Title

Identification of single guide editing strategy in TNFAIP3/A20 for improving adoptive cell therapy anti-tumor efficacy

ISBN

9798247946502

Author

Sandoval, Luis Roberto

Publication Date

2026-06-03

Peer reviewed|Thesis/dissertation

Identification of single guide editing strategy in TNFAIP3/A20 for improving adoptive cell therapy anti-tumor efficacy

by

Luis R. Sandoval

DISSERTATION

Submitted in partial satisfaction of the requirements for degree of

DOCTOR OF PHILOSOPHY

in

Bioengineering

in the

GRADUATE DIVISION

of the

UNIVERSITY OF CALIFORNIA, SAN FRANCISCO
AND
UNIVERSITY OF CALIFORNIA, BERKELEY

Approved:

Signed by:
Chun Jimmie Ye
6810A02CECA0469...
Chair

DocuSigned by:
Justin Eyquem
Committee Members

Alex Marson

Liana Lareau

Averil Ma
AD4FC9824DB043D...

Acknowledgements

A project of this scale and the effort of decades of academic preparation would not be possible without the support of many important people during this journey. I want to thank the teachers who were critical for supporting my early scientific curiosity especially Mrs. Genth and Mrs. Patterson. I also want to highlight the guidance of mentors in my career that elucidated the path towards this PhD: my older sister Bianca who I will forever be indebted for her sacrifices in leading the way for me and ensuring I would benefit from her experiences, my undergraduate research advisors Lisa Anderson and Kristala Prather, Carlos Barrajas and Domitilla Del Vecchio for establishing the fundamentals and scientific thinking in the lab, and my research advisors Justin Eyquem and Jimmie Ye for creating a space for impactful and novel science that allowed me to always focus on progressing my scientific ability and skills.

I need to also thank the people that support the balance in my life during this endeavor. My family with both mi padres, Victor and Margarita, and mis hermanos Bianca, Victor, Alondra, and Sergio. Without your ability to be a place to always recenter myself and be unconditionally supported this PhD would be impossible to complete. My friends in the bay area, Ohio, and Boston who have given me advice at critical points of my life and career. A special thanks goes to the people residing in the 20 Upton house in Boston who created a beautiful life even in the time of isolation and the Fugacity squad that has created space to think about the science and life outside the lab. I want to thank Lordean Gustinvil and Gary Li for their unwavering friendship throughout the entirety of the PhD. I also want to give a big thank you to Maria Elgueta for being a grounding force for life outside the lab and reminding me that working hard in lab and living life id possible. Finally, I want to thank all the people who usually go

unnamed: cousins, uncles and aunts, fraternity brothers of Zeta Beta Tau at MIT, as well as the entire Hispanic community that rallies to support each other in their time of need. This PhD is just as much of an accomplishment for every individual I listed as it is for myself.

Dedication

To every Latino who was able to follow their dream to “seguir adelante” with education in the US even as they felt guilt that they should be staying at home para ayudar tus padres or estar pendiente de apollar la familia. This is a testament that it is possible to achieve more, to not only go beyond what your parents could have dreamed for you to achieve but to do in a field that stands to benefit others.

Contributions

For work discussed in chapter 1, Luis R. Sandoval, Justin Eyquem, Chun Jimmie Ye, and Averil Ma conceived and designed experiments. Luis R. Sandoval conducted all experiments and analysis. Charlotte Hui Wang and Yang Sun assisted with design of library, sequencing, and analysis of resulting data.

For work discussed in chapter 2, Adam Blaisdell, Stefanie Bachl, Luis R. Sandoval (myself), Barabara A. Malynn, Justin Eyquem, Julia Carnevale, and Averil Ma conceived and designed the studies. Adam Blaisdell, Stefanie Bachl, Luis R. Sandoval (myself), Carter Ching, and Manu Prabandham performed and analyzed in vivo experiments, while Zhongmei Liu, Qi Li, Jin Seo, Shimin Zhang, and Charlotte Hui Wang provided assistance. Stefanie Bachl, Nupura Kale and Julia Carnevale performed genome-wide CRISPR screen, and Morgan Diolaiti analyzed the next-generation sequencing screen data. Adam Blaisdell, Manu Prabandham, Rommel Advincula, Dorothea Stibor, and Inger Øynerbråten performed and analyzed mouse tumor and T cell experiments, while Nika Lenci, Emily Yamashita, Philip Achacoso and Chirstopher J. Bowman provided assistance and guidance. Stefanie Bachl, Luis R. Sandoval, Carter Ching and Claire Havig performed and analyzed human T cell experiments. Chun Jimmue Ye and Alex Marson provided guidance for genomic ESM1b and base-editing analyses. The manuscript was written by Adam Blaisdell, Stefanie Bachl, Luis R. Ssandoval, Barbara A. Malynn, Justin Eyquem, Julia Carnevale. and Averil Ma and edited by Christopher J. Bowman, Alan Ashworth, Chun Jimmie Ye and Alex Marson with input from all authors.

Identification of single guide editing strategy in TNFAIP3/A20 for improving adoptive cell therapy anti-tumor efficacy

Luis Sandoval

Abstract

Tumors drive T cell exhaustion in both tumor-infiltrating lymphocytes and CAR T cells, marked by increased inhibitory receptor expression, impaired cytotoxicity, and reduced cytokine production, ultimately limiting durable clinical responses. In this work, I have performed a high-density base editor screen of A20/TNFAIP3, a multifunctional ubiquitin-modifying protein, to map variants to T cell functions. In addition, we performed genome-wide loss-of-function screening in repetitively stimulated human T cells and identified the multifunctional ubiquitin-modifying protein A20/TNFAIP3 as a major negative regulator of exhausted T cell persistence. Protein large language modeling, deep base-editing mutagenesis, and studies in immunocompetent mice with domain-specific inactivating mutations revealed A20's non-enzymatic M1 ubiquitin-binding zinc finger 7 ($A20^{ZF7}$) motif as critical to suppression of anti-tumor immunity. $A20^{ZF7}$-deficient $CD8^{+}$ tumor-infiltrating lymphocytes (TILs) resisted terminal exhaustion and circumvented an unappreciated mechanism restraining perforin degranulation in terminally exhausted cells. Human chimeric antigen receptor (CAR)-T cells engineered via base-editing to inactivate $A20^{ZF7}$ via a single missense mutation also resisted exhaustion, secreted more perforin and robustly suppressed cancer *in vivo*. These studies pinpoint $A20^{ZF7}$ as a novel T cell checkpoint and reveal precision base-editing of missense mutations as an effective approach to enhance CAR-T cell therapy.

Table of Contents

Introduction 1

Chapter 1: Base Editor Saturation Mutagenesis Screen of A20 in CAR-Ts 5

Introduction 5

Design of Functional Screens and Cell Engineering 7

Base Editor Library Design 9

Completion of Screens and Sequencing of resulting libraries 11

Data analysis for collected screen 11

Discussion 19

Chapter 2: Base-editing a single missense mutation in A20 enhances CAR-T cell efficacy 22

Introduction 22

A genome-wide CRISPR perturbation screen identifies A20/TNFAIP3 as a key regulator of T cell dysfunction upon chronic antigen stimulation 24

A20 ablation enhances ACT anti-tumor activity in vivo 30

Inactivation of the zinc finger 7 domain of A20 invigorates anti-tumor immunity 32

$CD8^+$ T cell-intrinsic $A20^{ZF7}$ inactivation invigorates anti-tumor immunity 37

$A20^{ZF7}$ inactivation alleviates terminal exhaustion of $CD8^+$ T cells 42

Perforin, but not IFNγ or TNF, drives enhanced anti-tumor immunity in $A20^{ZF7/ZF7}$ mice 48

A20^{ZF7} inactivation unleashes perforin degranulation by exhausted CD8^{+} T cells 51

Cas9-editing of A20^{ZF7} in human CAR-T cells enhances anti-tumor immunity in vivo 58

Base-editing of A20^{ZF7} enhances cytolytic function of human CAR-T cells in vitro 60

Base-editing of A20^{ZF7} enhances human CAR-T cell efficacy in vivo 65

Discussion 68

References 72

List of Figures

Figure 1.1 Coverage Plots of NG PAM Base Editor library for TNFAIP3/A20 10

Figure 1.2 Assessment of Library Quality through Null Distribution and Donor Correlations 12

Figure 1.3 Guide Level Cross Assay Correlations in each Cell Type 13

Figure 1.4 TNFAIP3 Mutational Landscape per Variant 15

Figure 1.5 TNFAIP3 Mutational Landscape per Position 18

Figure 1.6 ESM-1b Correlation for Persistence Assay in CD4s using CBE 19

Figure 2.1 A20 is a key regulator of human T cell dysfunction upon chronic antigen stimulation. 27

Figure 2.2 A genome-wide CRISPR perturbation screen identifies A20/TNFAIP3 as a key regulator of T cell dysfunction upon chronic antigen stimulation. 29

Figure 2.3 Inactivation of A20's zinc finger 7 domain invigorates anti-tumor immunity. 34

Figure 2.4 $A20^{ZF7}$ inactivation augments anti-tumor immunity across tumor models and promotes anti-tumor memory. 36

Figure 2.5 $A20^{ZF7}$ inactivation specifically within $CD8^+$ T cells augments anti-tumor immunity. 38

Figure 2.6 $CD8^+$ T cell-intrinsic $A20^{ZF7}$ inactivation invigorates anti-tumor immunity. 40

Figure 2.7 A20^{ZF7} inactivation alleviates terminal exhaustion of CD8^{+} T cells. 44

Figure 2.8 A20^{ZF7} inactivation alleviates terminal exhaustion following repetitive TCR stimulation. 46

Figure 2.9 Perforin drives superior anti-tumor immunity in A20$^{ZF7/ZF7}$ mice. 50

Figure 2.10 A20$^{ZF7/ZF7}$ Ttex paradoxically exhibit reduced perforin. 52

Figure 2.11 A20^{ZF7} inactivation unleashes Ttex perforin degranulation. 54

Figure 2.12 A20^{ZF7} suppression of Ttex degranulation depends upon repetitive TCR stimulation. 56

Figure 2.13 Base-editing to inactivate A20^{ZF7} enhances CAR-T cell function *in vitro*. 59

Figure 2.14 Cas9- or BE-directed A20^{ZF7} inactivation augments CAR-T cell anti-tumor activity without safety concerns. 63

Figure 2.15 Base-editing to inactivate A20^{ZF7} enhances CAR-T cell function *in vitro* and *in vivo*. 66

Figure 2.16 BE-directed A20^{ZF7} inactivation augments CAR-T cell anti-tumor activity. 67

Introduction

Adoptive cell therapies have emerged as a groundbreaking approach in cancer therapeutics. Designed as autologous treatments, two major approaches have taken shape in this field. One enriches for tumor associated T cells, the other reprograms T cells with the addition of an exogenous receptor. These receptors are either curated T cell receptors targeting tumor antigen or a fully synthetic receptor commonly derived from immunoglobulin polypeptides and T cell intracellular signaling domains. This product is then reinfused into patients to achieve durable complete responses in patients with extensive history of interventions. These innovative methods have demonstrated remarkable success in clinical trials, validating the potential of T cell-based cancer immunotherapies.[1] The U.S. Food and Drug Administration (FDA) has recognized its promise by approving one TCR-T, one TIL, and six chimeric antigen receptor (CAR) T cell therapies for various cancers, including acute lymphoblastic lymphoma, diffuse large B cell lymphoma, multiple myeloma, melanoma, and synovial sarcoma.

Despite advancements in manufacturing, design, and administration, T cell therapies face challenges, particularly in treating refractory hematological malignancies and solid tumors. Issues such as tumor antigen escape, non-targeted killing, poor trafficking and infiltration, the immunosuppressive tumor microenvironment, and CAR-T cell-related toxicities need to be addressed.[2] A key focus is enhancing CAR-T cell persistence, which is strongly correlated to improved survival rates. Current strategies, like the use of anti-PD1 or anti-PDL1 antibodies, have shown relative success in advanced cancer patients as they target immune checkpoint mechanisms that tumors exploit to suppress T cell cytotoxicity.[3] However, combining these

strategies with a CAR-T therapy could potentially be counterproductive. Instead, a more promising approach might involve simultaneous genetic modifications during T cell engineering.

CRISPR genome editing technology has sparked considerable interest in refining adoptive T cell therapies by targeting additional genetic elements. It has enabled us to scan the entire human genome to pinpoint genes that enhance the effector and persistence functions of T cells.[4] While certain genes have been identified that, when knocked out, enhance T cell function in terms of activation, sensitivity to antigens, and effector responses, some are too vital for T cell operation to be completely removed.[5] This was evidenced in the case of PD-1; while a prime candidate for knockout due to its role in immunosuppressive environments, its silencing led to reduced efficacy by inhibiting proliferation.[6] Therefore, more nuanced methods of modulating T cell function are under investigation.

Databases like Genome Aggregation Database (gnomAD), dbVar, Human Genome Variation (HGV), and ClinVar have cataloged genetic variants that contribute to autoimmune diseases and an increased risk of cancer. Analysis of these databases have related how domain and residue-level variation in genes affect immune system function, which can inform the design of genetic perturbations to improve CAR-T cell therapy. Coding variants isolation clinical samples from autoimmune disease and T cell lymphomas in canonical T cell signaling pathways, which have been inaccessible with CRISPR genome wide screens, have proven beneficial to CAR-T function.[7]

Given the potential to have further tunability of T cell function with coding variants can expand potential perturbations from the number of human protein coding genes to all potential domains of proteins or single amino acid mutations. The increased scale exceeds two orders of magnitude difference and limits feasibility of studying all possible single amino acid variants at

whole genome scale. The advent of A.I. based tools for variant effect prediction such as ESM-1b have been useful in being able to increase the power of any genetic study.[8] Trained on 250 million protein sequences across all evolutionary diversity to be able to identify single amino acid variants likely to be impact protein function. This new technology has further opened the door to be able to design focused experiments to survey variants in genes associated with T cell immunity.

In this thesis, I focus on the TNFAIP3 gene, associated with a multitude of autoimmune conditions and a critical regulator of immunity.[9] Previous work profiled dominant immune tumor archetypes across several cancer types correlated TNFAIP3 with increase exhaustion and expression of PD-1 in most of the cancer types surveyed.[10] Its protein product, A20, is a negative feedback regulator of the NF-κB pathway in T cells. Although A20's role in this pathway is well understood, efforts in studying A20's effects are entangled in the pleotropic nature of the NF-κB pathway which is implicated in cell activation, inflammation control, cell survival, and memory formation and fitness.[11] This points to further understanding the structure, domain, and residue level effects of A20 for leveraging genetic perturbations for modulating immune cell function. A20 structure is composed of one large N terminal OTU region containing catalytic activity for K63 deubiquitinating and a series of seven Zinc Fingers (ZF). Of these seven ZF regions, ZF4 contains catalytic activity for K48 ubiquitination and ZF7 binds linear polyubiquitination.[12] These regions regulate NF-κB signaling through TNF sensing through deubiquitinating of RIP1 and NEMO to destabilize a K63 polyubiquitination chain, ubiquitination of RIP1 and Ubc13 for K48 mediated proteolysis, and binding to the dimerized NEMO, IIK1/IKK2 complex. Through the same NF-κB regulation, A20 is also implicated in TCR signaling and subsequently downstream signaling that confers memory formation and early effector function.

Even with previous studies understanding the molecular interactions of A20 with ubiquitination or regulatory partners, many regions of the A20 protein are still yet to be understood. Studies such as Tokunaga et al.[13] have studied function of zinc fingers and OUT domain in NF-kB regulation but have not paid as much attention to the unannotated regions. Even with the advancement of computational structure prediction tools such as AlphaFold[14], little is known about the importance of the sequence of these inter Zinc Finger domains and the regions around OTU. With this understanding, I aim to extend this body of research by examining A20's role in anti-tumor immunity at the variant level in primary human T cells. Attempting to perturb A20 through use of an unbiased high density base editor screen using functional readouts and a more guided approach through filtering of known literature to arrive at a candidate guide for modulation of T cell function. We can leverage these findings to inform an A20 editing strategy to improve adoptive cell therapies. In the end we were able to identify an editing strategy of A20 ZF7 through the mutation of Cysteine 779 that allows the unleashing of NF-kB activation that results in a more potent adoptive cell therapy but retains the safety characteristics of an effective anti-tumoral treatment.

Chapter 1: Base Editor Saturation Mutagenesis Screen of A20 in CAR-Ts

Introduction

Historically identifying genes related to optimized phenotypes was a herculean task. Forward genetic screens through random mutagenesis in animal models such as drosophila or mice were once the only way to identify genetic elements responsible for observed phenotypes. Although these screens uncovered a large number of genes and regulatory elements, they were inherently limited in scale and could not comprehensively interrogate the genome for a phenotype of interest. Recently the discovery of programmable editing tools initiated by the development of CRISPR-Cas9 has allowed the design of reverse genetic screens wherein the entire protein coding genome can be perturbed in a pooled fashion. With this the first genome-wide CRIPSR-Cas9 knockout screens were completed in cell lines and eventually transitioned to primary human cultures to further advance our understanding of phenotype regulation through protein coding genes.

Many of these screens completed in primary human T cells have been focused on the improvement of function within T cells to apply genetic engineering strategies to adoptive cell therapies or nominate a mechanism for modulation using a pharmacological agent. The first genome-wide screen in primary human CD8+ T cells from Shifrut et al.[4] overcame difficulties with editing to be able to identify genes responsible for proliferation. Following this landmark publication, the field has advanced, with the improvement of T cell editing techniques, to be able to complete screens surveying a wider space of T cell functions. Although these efforts have

generated an increasingly richer network of understand of genes implicated in T cell function the approach of full gene knockout still does not capture the casual domains or residues.

David Liu's group has been able to extend the gene editing toolbox beyond the nuclease version of CRISPR-Cas9, developing variants with fusion enzymatic domains for mutating DNA base pairs[15]. These variants of Cas9 that contain a reduced nicking ability can now reliably and precisely target regions in the genome and edit a window of cytosines or adenines, while preserving the protein expression creating protein mutants. This precise mutation through Cas9 Base Editors (BEs) allow us to be able to perturb the endogenous protein and conduct functional screens to understand the residue level effect of coding sequences to T cell function.

The field has started to implement these screens most notably with Schmidt, Ward et al[16] that completed functional screening of four markers CD25, PD-1, TNF, and IFNɣ in CD4+ T cells. These screens covered 385 curated genes through saturation of BEs to construct maps of residues that control these factors. Although TNFAIP3 (A20) was included in the set, these screens were conducted with a stricter Protospacer Adjacent Motif (PAM) NGG, that did not allow for dense coverage of all protein coding space. We understand that A20 contains many domains with annotated differential function in ubiquitin regulation that regulates TNF and TCR signaling. Additional annotated domains and unannotated regions may still be implicated in T cell function. BE screening would be the best way to understand A20's domains and residues role in T cell function. In this chapter, I cover my efforts to conduct a high-density NG PAM BE screen with functional readouts that are important for antitumoral efficacy of CAR-T cells with the goal of translating findings for applications in adoptive cell therapies.

Design of Functional Screens and Cell Engineering

To translate these findings of T cell function regulation through residues of A20, I decided to design functional screens to enrich for mutants that would directly lead to improvement of complex functions of adoptive cell therapies. Groups such as the Carnevale lab at UCSF have developed in vitro functional assays to drive human T cells to chronic antigen exhaustion. Using an immortalized cancer cell line (target cells) that express a target antigen, we can control exposure to target cells through co-culture with effector CAR-T or TCR-T cells that encode a receptor for that target antigen. Then repeated exposure is completed at an aggressive rate to promote cells to drive effector cells to exhaustion. Effector cells are collected in the repetition where target cells are able to survive co-culture, indicating reaching a state of dysfunction. This assay (RepStim) allows us to recover cells with a complex output of proliferative potential, killing efficacy, and ability to resist dysfunction. Since this assay is an additive readout of many T cell functions that contribute to antitumoral efficacy, I decided to include another co-culture-based assay to fully isolate the ability to assess proliferation. This proliferation assay follows the same set-up as the RepStim assay but at a weekly exposure to allow for rest between stimulations.

Two other proposed assays included production of two cytokines: TNF and IFN-ɣ. These two factors are critical for antitumoral activity and produced differentially through CD4s and CD8s that would be able to identify cytokine production in each subtype of T cells. To complete this assay, effector cells are co-cultured with target cells at a ratio of 1:1 in media containing a protein transport inhibitor and collected 6 hours later to be stained. Cells are fixed and permeabilized to be able to complete intracellular staining of TNF and IFN-ɣ. Cells would be sorted in quantiles, with the top 2 and bottom 2 quantiles collected for comparison against the

baseline library pre-sort. Each respective quantile will point to enrichment of guides that increase or decrease each respective cytokine.

Finally, to be able to screen human T cells with a targeted receptor for co-culture assays, I used an engineering strategy published in Eyquem et al[17] where a CAR is introduced to the TRAC locus to result in a mono-allelic targeted knock in, simultaneously removing the endogenous TCR and placing a CAR under regulation of the TRAC locus. This approach is completed through AAV transduction to deliver a donor template and CRISPR-cas9 electroporation to induce a double stranded break (DSB) at the knock in site. Although this approach has been used with success to conduct multiplexed editing of CAR-T cells using Cas9, base edit screening with this system poses unique issues.

An interesting characteristic of Cas9 editors is their ability to guide swap, where competing guides can replace the guide already complexed to a Cas9 protein. Many have used this to improve stability of Cas9 during delivery in other method such as in Ting et al.[18] In this case a guide swap with a base editor would result in a DSB in the A20 locus as the guide used to target the Cas9 BEs would complex with Cas9 from the TRAC KO. To overcome this restriction, an orthogonal Cas12a system was implemented to complete the TRAC DSB while allowing simultaneous use of Cas9 BEs. The Cas12a cutting site is located 28 base pairs downstream of the Cas9 site, allowing the use of similar homology arms for targeted knock-in.

Unlike the multiplexed Cas9 edits that pool mixtures of complexed guides and Cas9 protein, base editing in primary human T cells requires an alternative approach. Recent efforts to purify recombinant Cytosine and Adenine BEs have been commercially unsuccessful ruling out the ability to complex targeting guides and purified BEs to electroporate as ribonucleoproteins. Instead, we encoded the base editor into a mRNA produced through in vitro transcription. This

allows us still to deliver the base editors through electroporation, with the mRNA producing functional BEs in receiving cells through translation. Targeting synthetic guide RNAs (sgRNAs) can be co-electroplated to complex after BE creation to create a functional BE RNP. With this editing strategy we can create targeted knock in TRAC-CARs with A20 Base edits.

Base Editor Library Design

To cover more space of the protein coding sequence as compared to the previous screens, we elected to design a guide library with use of a NG PAM BE. This will allow us to cover more sites in A20. To construct this library, I developed a custom python script to take in a genbank file encoding for the gene loci of interest containing annotations for coding sequences. The script then identifies all possible NG PAM protospacers of guides that can target the input sequence. Guides are then filtered to overlap with the annotated coding sequence regions. Guides that contain available base pairs for editing within the expected editing window of each BE are retained for further filtering with a subset of non-editing guides retained for negative controls. Additionally guides that overlap with known splice acceptor or donor sites are added to this filtered list. In the end the script generates three lists, two BE specific lists per editor and a combined list that removes duplicates and attached adaptors to the guide sequences for synthesis and cloning into a plasmid backbone.

With this library construction method, we can access 95.95% of the coding sequence by position (759/791 total residues) across both editors. Totaling 1285 number of guides in the library including controls, we can generate three important plots for assessing the depth of importance of the mutations space covered. First is a confetti plot that shows mutations that are generated together from a single guide, as shown in figure 1a. Notably this points out the biased mutational space achieved by base editors, where some resulting residues are over-represented

compared to others. Additionally, this code generates a comparative analysis of the resulting mutational space with AI prediction tool ESM-1b. Using a collected tabulated file from ESM-1b predictions, the code can generate coverage plots with ESM-1b log likelihood ratio (LLR) scores and a histogram with the distribution of LLRs to demonstrate potential disruptive mutations in the protein coding sequence (figure 1b and 1c).

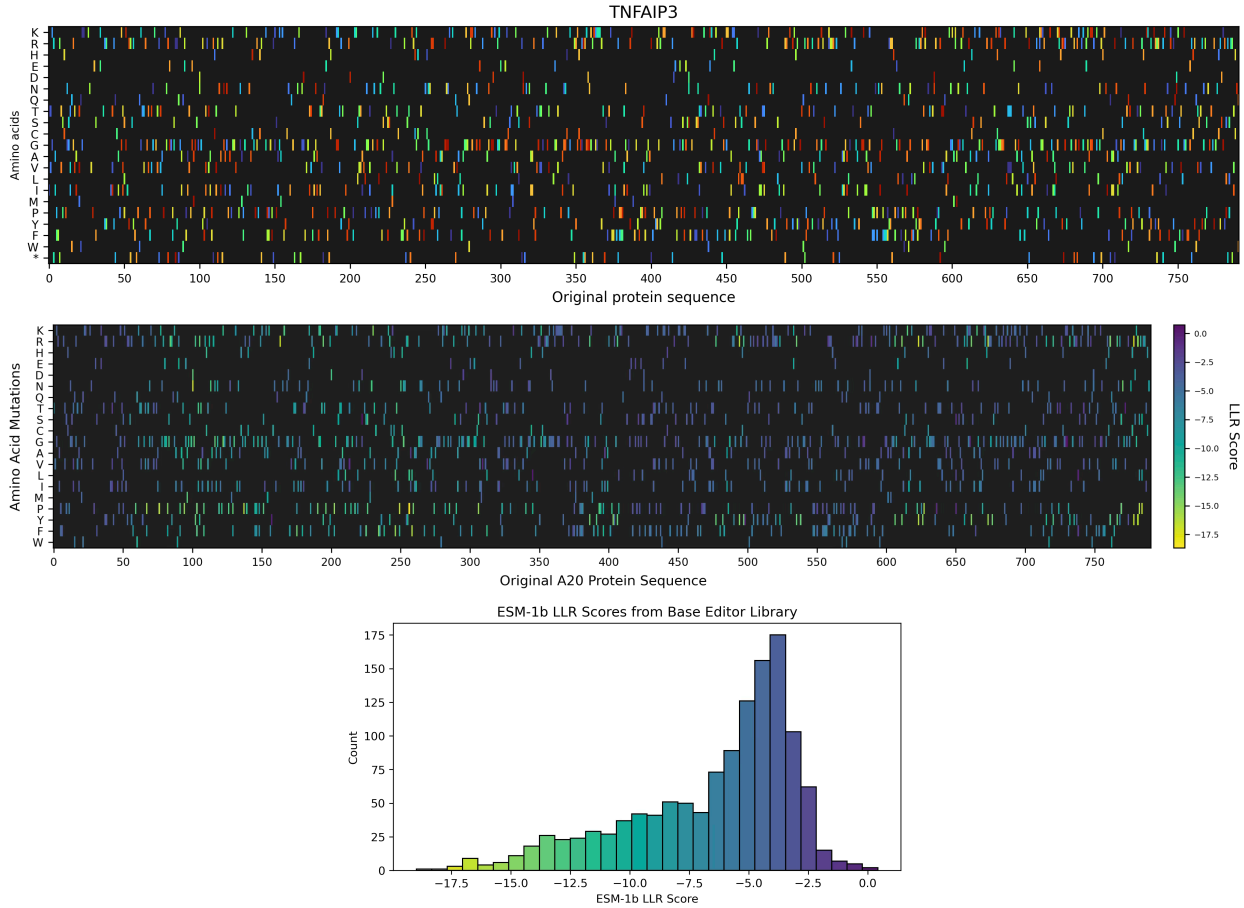

Figure 1.1 Coverage Plots of NG PAM Base Editor library for TNFAIP3/A20
Plot demonstrating coverage of BE screen in A20. (a) Color indicates mutations that are generated with a single guide. If mutations are positioned adjacent and are the same color, they are predicted to be generated by the same guide. (b) Heatmap representing total coverage of entire single amino acid mutational space with color mapping with ESM-1b LLR score. (c) Histogram of ESM-1b scores of mutations predicted to be made with Base Editor screen in A20.

Completion of Screens and Sequencing of resulting libraries

Screens for RepStim and proliferation were completed using separated CD8+ and CD4+ anti CD19.28z TRAC-CARs in coculture with target A375 human melanoma cell expressing CD19. RepStim was conducted until repetition 8 and proliferation assay was collected 20 days after initial stimulation. A coverage of x4000 was kept during all points of the screen to preserve any signal due to inherent noise of base editor screens. Cells were collected by centrifugation and decanting media, drying the cell pellet, and flash freezing in liquid nitrogen. To recover genomic DNA (gDNA) and read out guides from resulting libraries, phenol:chloroform:isoamyl alcohol extraction was completed and gDNA precipitated with sodium acetate and washed with 70% ethanol. PCR for NGS was completed with ExTaq polymerase, with protocol from the Broad Institute for PCR of guides for Illumina sequencing. PCR products were purified using solid phase reversible immobilization. Libraries were diluted to 10nM, equimolar pooled, and submitted for NGS on a NovaSeq X (Illumina). Targeted sequencing depth was x4000, but minimum sequencing reads per lane for custom library resulted in an average of x20000.

Data analysis for collected screen

After sequencing fastq files were analyzed using MAGeCK.[19] The command MAGeCK count was used to assess fastq files, representing each collection timepoint, for the presence of guide sequences and count them. Next, MAGeCK test was run to assess the distribution of guides and comparisons across different assay collections relative to distribution of synonymous guides as controls. For downstream analysis outputs from MAGeCK are collected in python to ensure all samples reached at least a median count of 4000 to achieve sufficient depth, all samples passed this metric. Then using synonymous guides, those that mutate the coding sequence in A20 but results in no change in the protein sequence, as a null distribution I

calculated the per sample deviation to ensure no shift was observed from 0. All samples passed this metric as shown in Figure 2a. Inter-donor correlations were drawn in each condition to assess if screens achieved consistent signal across biological replicates as in Figure 2b. Looking across editors, the ABE conditions showed little Pearson correlation with most guides centering around 0 $\log_2$ fold change (LFC). This would indicate that all the ABE conditions were not able to effectively enrich for guides, which reasons to why this might be discussed in a later section. For CBE conditions correlation values start to become better but unable to get correlation expected from previously published screens. Only CBE conditions were kept for the remainder of the analysis.

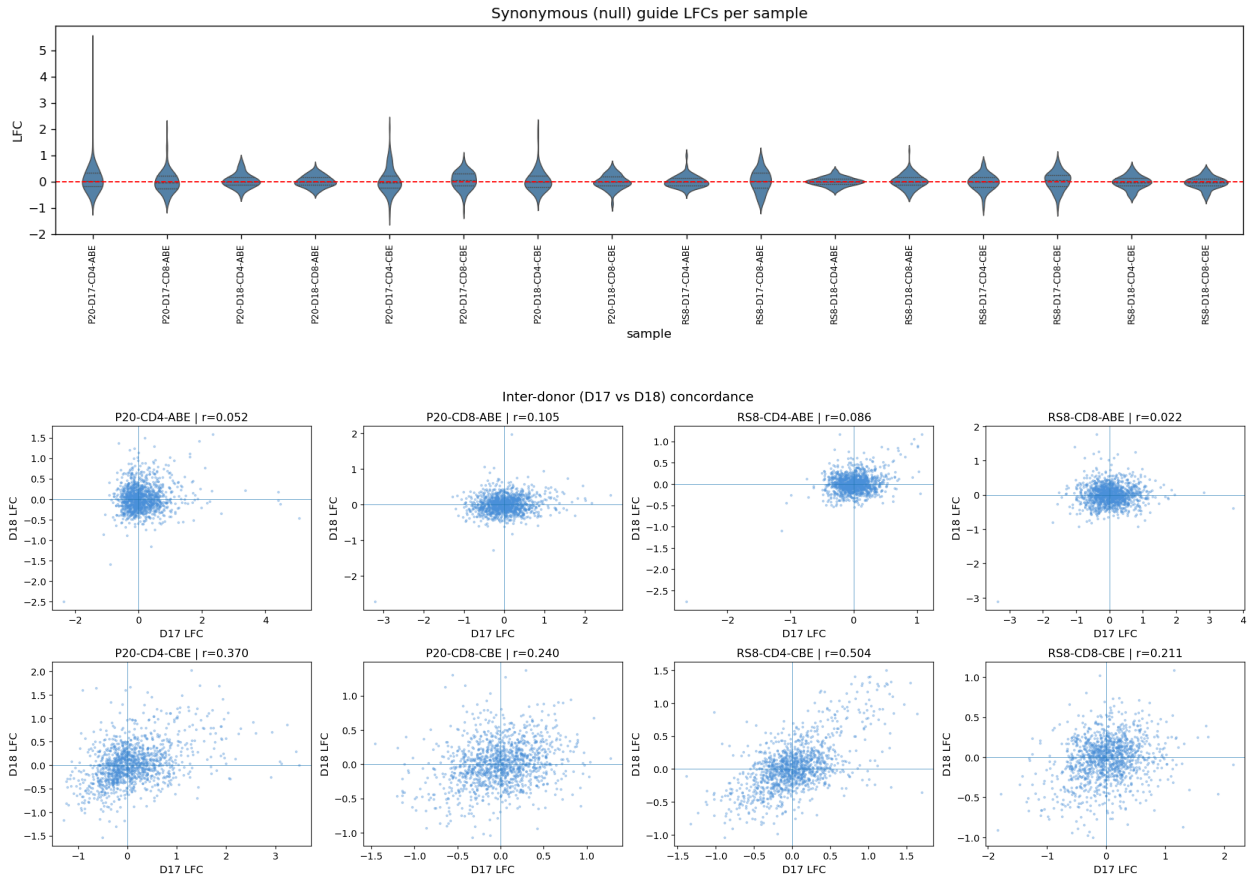

Figure 1.2 Assessment of Library Quality through Null Distribution and Donor Correlations

(a) Null distribution of synonymous guides in each library after MAGeCK processing. (Figure caption continued on the next page)

(Figure caption continued from the previous page) Highlighted dash line at 0 for expected medium of each distribution. (b) Donor to donor correlations for each condition of guide LFC enrichment separated by base editor. Proliferation samples are denoted with P20, and repetitive stimulation samples are denoted by RS8.

Within the CBE libraries the reduction of guide LFCs range for CD8s points to a reduction in signal that reduces the ability to confidently call hits from that arm of the study. In this case CD8s in the CBE arm are kept with the additional caution of calling hits. Starting with looking at the guide level effects, we can start to call concordance of donor pooled samples in each cell type. We observe greater LFC in CD4 than CD8s with a cutoff of absolute 0.5 LFC for either assay resulting in 97 and 65 guides passing this cutoff (Figure 1.2). Each comparison demonstrates the predicted concordance between the two functional assays of persistence and proliferation as the spearman correlation between the two assays reaches 0.70 for CD4s and 0.50 for CD8s.

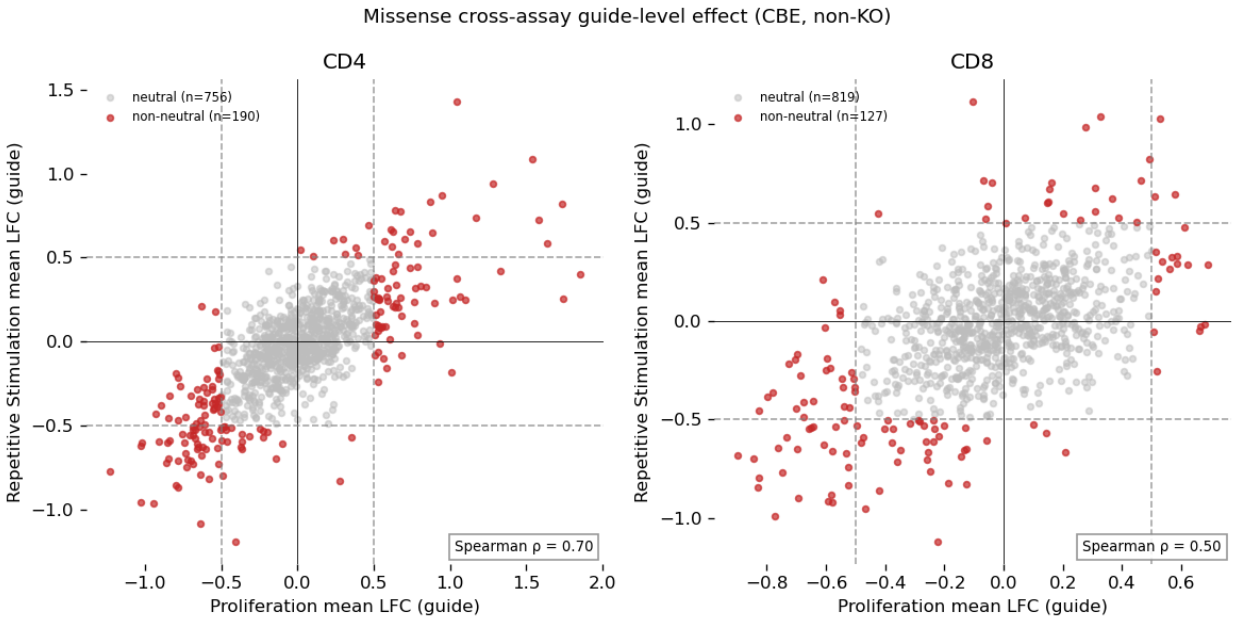

Figure 1.3 Guide Level Cross Assay Correlations in each Cell Type
Guides $\log_2$ fold change across two assays of repetitive stimulation and proliferation. Points colored in red are guides that pass a LFC of 0.5 in either assay.

To pinpoint specific variants, I completed a LFC assignment from each guide to the expected variant per guide. Using Stouffer's Z-score method to combine potential overlap between guides that overlap in the same mutational space, we can pileup the effects of a single mutant that may be represented in multiple guides. This does come with a caveat of potential reduction of signal for guides that are more efficient at creating specific mutations, but we overcome this by weighting the highest LFC twice. This guide preference effect can be the additive effect of editing efficiency of the guide overall but also the mutation position within the editing window of a base editor. Although data cannot be shown many prediction tools demonstrate a normal distribution curve of editing in the window that preferentially edits at the center. This is especially important to include for the CBE set as the window of editing is position 1-13 of the protospacer. For positional analysis, the same approach was taken by summing up all mutations in the same index of the protein sequence.

Using this weighted method, we can bin the guides into tiers of confidence for being able to call variants. To account for each individual assay's noise, I used dynamic cutoffs by calculating the minimum detectable effect (MDE) in which the synonymous guides are used to model a null distribution of the noise floor. This is calculated using the equation below where σ_{post} is the standard deviation of the LFC of a guide over the synonymous guides distribution in each assay. The number of independent guides n that contribute to each variant or position. Then standard normal quantiles are encoded using permissive rates to allow for discovery of hits.

$$MDE(n) = \frac{(z_{1-a/2} + z_{1-\beta})\,\sigma_{post}}{\sqrt{n}}$$

This allows for the generation of MDE per assay (donor pooled) for variants and positions that allows us to informatively bin guides if the effect size per variant or position is significant

compared to each libraries noise. Using this framework guides are binned into four tiers. Tier 1 that has a MDE α of 0.1 to makeup a 5% chance that a null guide reaches a one-sided effect with power of β of 80%, a standard convention for a screen with an FDR called from MAGeCK of less than or equal to 0.0. Tier 2 mimics the previous with an adjustment of α of 0.25 to allow for looser assessment if the LFC drives past the noise floor and the same cutoff of 0.05 for FDR from MAGeCK. Tier 3 only requirement calls for the FDR floor of 0.05. Then if a variant or position does not meet these guidelines it falls into not significant (NS).

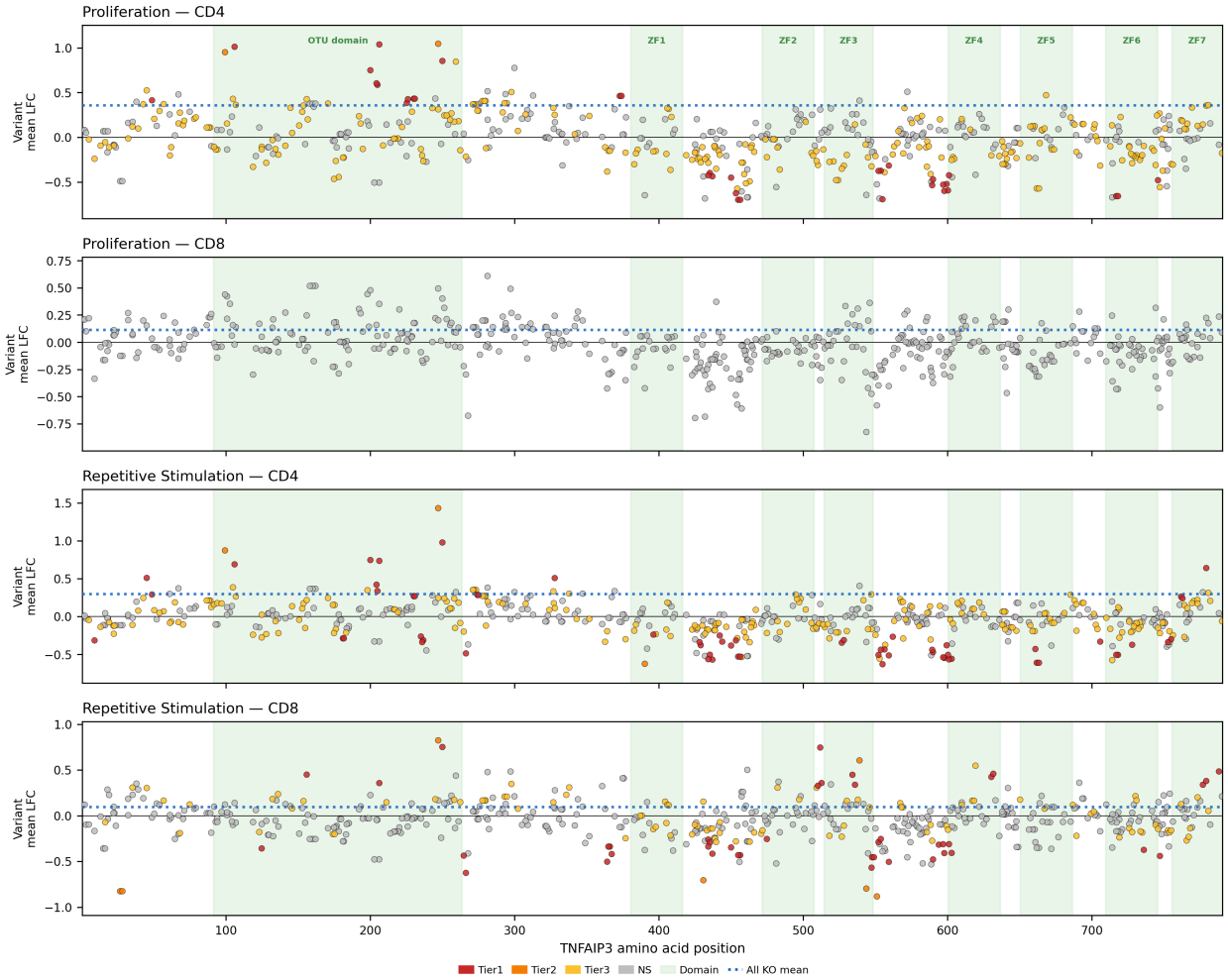

Figure 1.4 TNFAIP3 Mutational Landscape per Variant
Log_2 fold change of Stouffer's weighted mean of all variants plotted out by position. Respective enrichment and depletion of positions are colored by tiering of results. Regions that are annotated are labeled in green. Mean of all KO guides is labeled as dashed line across plots.

Looking at the variant landscape in Figure 4, we can see tiered hits come out of each assay with a clear lack of hits specifically in the CD8 proliferation. Looking into FDR values collected from MAGeCK test call for these libraries, all guides fail to reach significant, showing that there is not sufficient signal. The resulting weaker value from this assay points to reduced selection pressure from this library which can could be intrinsic to attempting to proliferate CD8s in isolation. Looking across all the other assays, we can observe some regions to be important across the two assays in CD4s, P247L, L250F, P206L, H106Y, and G99S in the OUT region come out as highly enriched variants surpassing the mean KO score. Additionally, C779Y in CD4s located in the Zinc Finger 7 domain also enriches heavily in repetitive stimulation but modestly enriches in proliferation. This mutant also more heavily enriches in CD8s for repetitive stimulation with multiple guides corroborating the effect. There are additional hits such as H512Y that distinctly enrich only in the CCD8s which target the unannotated region between ZF2 and ZF3 and C539Y that target Zinc finger motif structure. Interestingly, unannotated regions between ZF1/2 and ZF3/4 seem to have negative effects in proliferation and persistence which would not be expected as these regions are not known to be important for ubiquitination function.

Turning our focus to the variant landscape when the information is compressed per position in Figure 1.5, we can observe similar trends as the per variant analysis. As the positions compile effects of multiple variants, we observe that NS positions get squished making it easier to identify important residues for A20 protein function. In CD4s we observe further corroboration around the same sites of P247L, L250F, P206L, H106Y, and G99S. We additionally see the more striking enrichment of C779 in both CD4s and CD8s for persistence. These illustrates the screen's ability to identify specific variants that are expected to disrupt

A20's protein function such as C539Y and C779Y that ablate one of four cystine residues required to form the zinc finger motif that impart function to each domain. The same trend of interdomain regions between ZF1/2 and ZF3/4 being important for preserving proliferative and persistence capacity for both CD4s and CD8s.

Additional effort to relate these findings from this screen, albeit curtailed by smaller amount of signal, to AI prediction models like ESM-1b. Starting by taking guides that produce only one amino acid mutation, we take the persistence assay in CD4s using CBE and observe that the spearman correlation lands at 0.095. This does not show much confidence in being able to predict single mutant creating guides but as we have a variant and positional data, we correlated these results with ESM-1b in figure 1.6. This results in remarkable gain in correlation to -0.189 and -0.355 for variants and positions respectfully demonstrates that the individual guides and variants are too noisy of a signal to be able to accurately predict variant effects. This would be the one of the limitations of a base editor screen design that will be touched upon later. Even so the higher correlation in the per position prediction to screen data inspires the idea of being able to merge both methods, and fine tune models such as ESM-1b to better predict results in complex protein structures such as that of A20.

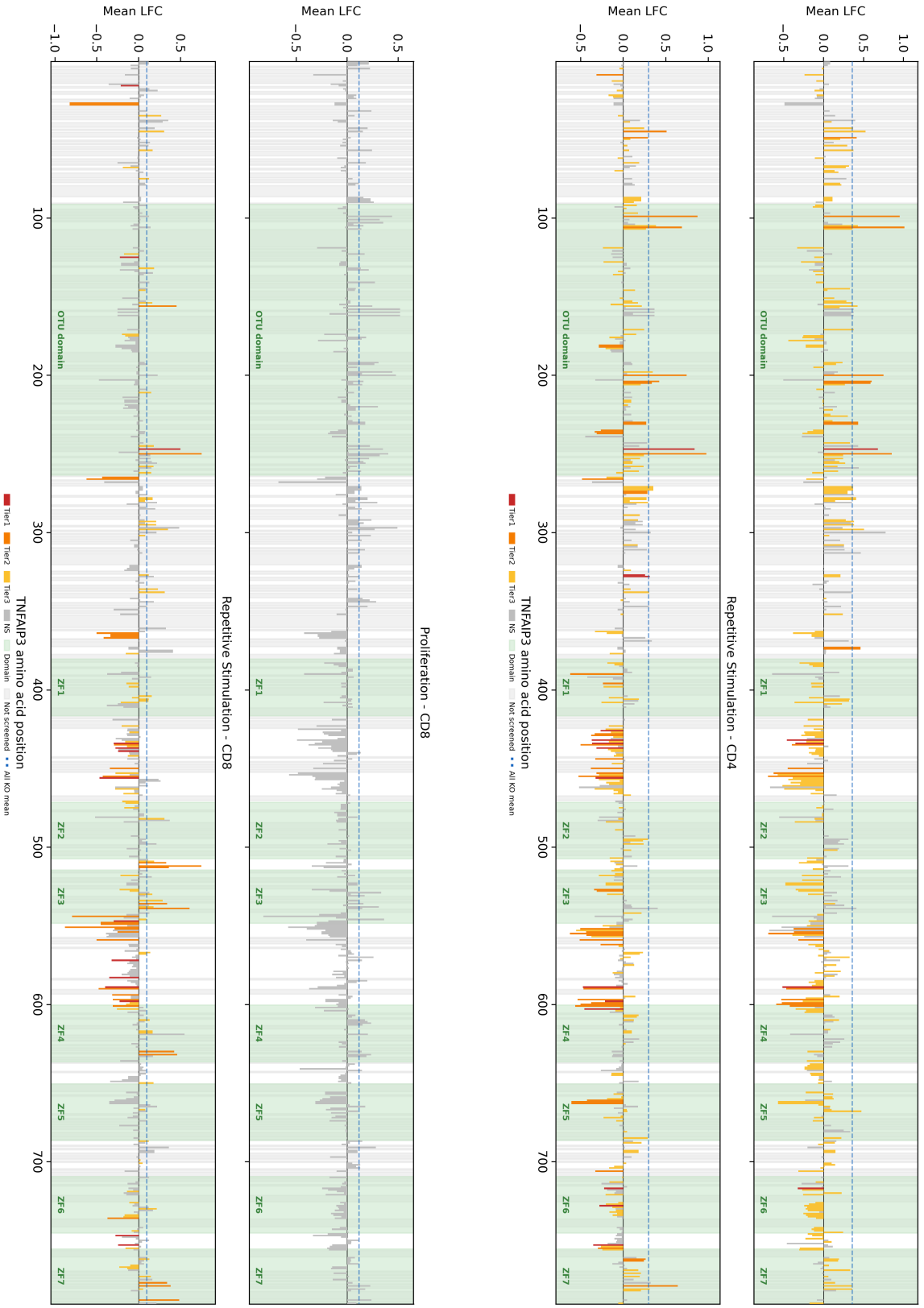

Figure 1.5 TNFAIP3 Mutational Landscape per Position
(Figure caption continued on the next page)

(Figure caption continued from the previous page) Log_2 fold change of Stouffer's weighted mean of all mutations per position. Respective enrichment and depletion of positions are colored by tiering of results, with tier 1 positions being represented by more than 1 guide, having absolute LFC greater than 0.5, a false discovery rate of less than 0.05, and more than 50% concordance between all covering guides. Tier 2 represents positions that contain a false discovery rate of 0.05 and Tier 3 are positions with an FDR less than 0.10. All grey bars are those positions not meeting the tiering criteria. Regions that are annotated are labeled in green and positions not covered are labeled in grey.

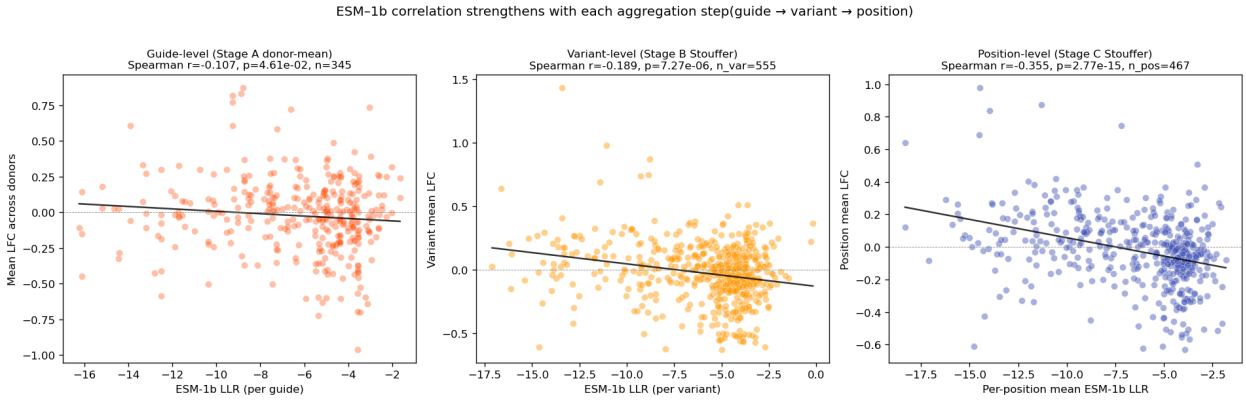

Figure 1.6 ESM-1b Correlation for Persistence Assay in CD4s using CBE
ESM-1b LLR scores correlated with spearman method against respective persistence CD4 CBE library single amino acid mutant producing guides, variants, and positional variants. Correlation increases as more variant information is aggregated in sequential steps.

Discussion

Although some variants and positions have been identified through this screen, no further work to validate these findings has been completed. There are many ways to interpret these results first before continuing into any validation work. Part of the limitations of conduction a base editor variant screen is the windowed effects that collects adjacent mutations together for each guide, resulting in the possible conflation of a single position or variant effect with simultaneous mutations. To overcome this limitation, the analysis binned variants and positions by effect but also tracked the number of guides covering the same space, which we can more confidently call variants for their perceived effects. To continue this work into arrayed validation we would consider the choice of single variants protein expression or guide-based mutation.

Each approach has limitations specifically for targeting TNFAIP3. For single variant mutant expression, we would need to find a way to either selectively mutate a single position through targeted knock-in or have pseudorandom knock-in and exogenous expression with a tandem endogenous TNFAIP3 KO to prevent any WT protein expression from masking variant effects. This would require considerable effort to generate a viable library in which the TNFAIP3 coding sequence would fit in a delivery vector or targeted integration would work efficiently for several domains of the TNFAIP3 locus. A guide approach would easily be able to be adapted from the pooled approach to replicate selected mutants, with the caveat of the windowed effect. Although an additional step can be added after to generate targeted integration methods to follow up on positive validation hits, which would drastically reduce engineering complexity by the reduction in numbers of hits.

In either case the screen nominates a considerable number of variants and positions to be important, in already annotated regions of OTU and ZF7 but also unannotated regions. The most interesting items to follow up are looking at the depleting variants and positions in the unannotated regions as these are the sequences in this protein that have not been linked to protein function and fail to be predicted well for structure using computational methods such as AlphaFold or for pathogenicity in ESM-1b. Shown here we have the beginnings of being able to tie these in silico prediction methods to functional data but there still exist a large gap with the best correlations only being achieved with data being compressed to a per position format rather than being able to confidently identify specific mutants. Many other studies have attempted to and continue to try to fine tune these prediction models with current functional data, but this requires a stronger and cleaner assay, in which case proteins like A20 and screens using base editors may be too noisy to provide clear results for training of these models.

There are also some additional difficulties associated with the design of this screen with the T cell engineering rely on the short-lived expression of base editors through mRNA expression at the time of electroporation. Unlike other previously published base editing screen conducted in primary human T cells where both the base editor and guide library were permanently expressed through lentiviral transduction, this design choice was taken to reduce the number of lentiviral transductions as the addition of AAV for targeted CAR knock in at the TRAC locus would already require electroporation. Given successful results with SLICE-seq approaches published, wherein the Cas9 effector was electroporated in a lentiviral guide library, we would have assumed this temporal restriction of base editor expression would not affect overall assay signal. Now comparing LFC changes between the two approaches the best way moving forward would be to maintain the two lentiviral transductions.

Even as this screen could not be completed with validation, it seems clear that understanding the unstructured and unannotated regions of A20 would be beneficial to link variants to functional tuning of not only T cells but potentially other cell types that use A20 as a key regulator of NF-kB activation for immune regulation. Application of this same screen or learnings from this project can be beneficial to inform future efforts in not only understanding A20 role in complex functions of immune cells but also refine functional genomics approaches for sparse mutational spaces such as that for base editing screens in other targets.

Chapter 2: Base-editing a single missense mutation in A20 enhances CAR-T cell efficacy

Introduction

Tumors induce an exhausted state in tumor-infiltrating lymphocytes (TILs) and CAR-T cells alike, characterized by increased expression of inhibitory receptors (IRs), diminished tumoricidal capacity, and reduced cytokine production.[20] Nevertheless, exhausted CD8 T cells (Tex) continue to express perforin and granzymes[21–23], suggesting that cytokines and cytotoxic granule proteins are regulated differently in Tex, and hinting at posttranscriptional restraint of cytotoxic potential. However, the ability of Tex to degranulate *in situ* within the tumor microenvironment (TME) has yet to be evaluated.

Identification of targets that can unlock the cytotoxic potential of Tex could markedly enhance cellular therapies. Repetitive *in vitro* T cell receptor (TCR) stimulation can mimic the chronic antigenic stimulation that drives T cell exhaustion, and when combined with CRISPR/Cas9 knockout screens can unveil key regulators of this process. To date, genome-wide screens in human T cells have utilized assays with a short course of one or two tumor cell co-cultures for repetitive antigenic stimulation.[24,25] However, a longer course of repeated tumor cell co-cultures could more closely model TIL experience in the TME, and uncover new therapeutic targets relevant to later stages of Tex differentiation.

In addition to Cas9-directed gene ablation, base-editors (BEs) have emerged as an efficient method to interrogate how individual amino acid changes affect T cell behaviors.[16,26] While BEs can ablate genes via nonsense mutations, their unique power lies in the precise tuning of protein function via hyper- or hypomorphic missense mutations. For multifunctional proteins,

this approach could specifically tune one function while preserving others. In the context of engineering next-generation adoptive cellular therapies (ACTs) such as TCR-T or CAR-T cells, BE-directed missense mutations could prove more efficacious and potentially safer. While large-scale BE screens have singled out missense mutations that improve CAR-T cell function *in vitro*[16,26], this approach has to our knowledge yet to boost efficacy *in vivo*.

A20/TNFAIP3 is a multifunctional ubiquitin (Ub)-modifying protein linked to autoimmune diseases.[27] A20 contains enzymatic and non-enzymatic domains with distinct functions that cooperate to regulate NF-κB and other Ub-dependent pathways.[27] Complete A20 deficiency in mice leads to systemic inflammation and perinatal lethality[28], while knock-in (KI) mice with A20 domain-specific hypomorphic mutations survive long into adulthood and exhibit variable degrees of spontaneous or inducible inflammation.[29–31] Complete or hypomorphic A20 deficiency within T cells can augment primary TCR responses but can also lead to cell death and impaired memory response to infection.[32–36] However, it remains unknown whether A20 or its hypomorphs impact T cell exhaustion, or whether A20 represents a suitable target for ACTs. Prior studies have implicated A20 as a suppressor of CD8 TIL persistence in the TME[37], as well as CD8 TIL cytotoxicity and effector cytokine (IFNγ and TNF) production[38–40], though the relevant anti-tumor effector mechanism was never directly tested. Notably, the requirement for specific effector cytokines versus cytotoxic granule proteins to suppress tumors can vary widely across models[41–48], and thus identifying targets that can enhance CD8 TIL cytotoxicity in multiple ways could lead to broader therapeutic applications.

Here, we use a genome-scale CRISPR knockout screen with a long duration of repetitive antigenic stimulation, a protein large language model for predicting missense variant effects, a BE tiling screen of the A20 gene, and a panel of A20 KI mice to unveil A20's non-enzymatic

zinc finger 7 ($A20^{ZF7}$) domain as a potent instructor of T cell exhaustion. Through the lens of A20 deficiency, we discover restrained perforin degranulation as an underrecognized post-transcriptional regulatory feature of Tex biology that is sharply reversed by abrogating the $A20^{ZF7}$ motif. Importantly, this enhanced degranulation, rather than increased effector cytokine production, provides the critical anti-tumor effector mechanism in $A20^{ZF7}$-deficient Tex. Finally, we show that a BE-guided missense mutation to inactivate $A20^{ZF7}$ substantially improves the efficacy of human CAR-T cells both *in vitro* and *in vivo*.

A genome-wide CRISPR perturbation screen identifies A20/TNFAIP3 as a key regulator of T cell dysfunction upon chronic antigen stimulation

The ability to repeatedly eradicate tumor cells during sustained tumor antigen exposure is an indispensable characteristic of therapeutic T cells. To reveal genes that have the potential to enhance T cell persistence and deter dysfunction, we employed an *in vitro* system that models chronic exposure to tumor antigen.[5,49] We engineered human T cells to express the NY-ESO-1 specific TCR (1G4) and repeatedly co-cultured them with fresh NY-ESO-1^{+} A375 melanoma cells (Figure 2.1). After multiple rounds of tumor exposure, we assessed the ability of TCR-T cells to eradicate tumor cells *in vitro*. TCR-T cells that were continuously exposed to tumor antigen displayed a substantial decline in their capacity to control tumor cell growth after each successive round of tumor stimulation, while TCR-T cells matched for time in culture, without prior exposure to antigen, maintained robust tumor-killing capability (**Figure 2.1**). Additionally, cell surface inhibitory receptors (IRs) whose expression are associated with T cell exhaustion (LAG-3, TIM-3, PD-1, and CD39) increased as TCR-T cells were repeatedly exposed to tumor cells, with the difference between tumor-exposed and unexposed TCR-T cells growing progressively over successive rounds of stimulation (**Figure 2.1C**). Finally, the capacity of TCR-

T cells to secrete effector cytokines (IFNγ, TNF) and cytotoxic granule proteins (perforin and granzyme B [GzmB]) decreased after several rounds of exposure to tumor cells (**Figure 2.1C**), providing further evidence of dysfunction from chronic antigen stimulation. Together these observations provide evidence that the chronic antigen stimulation we used models key aspects of TIL dysfunction.

To nominate gene modifications that improve TIL persistence and deter dysfunction in the TME, we performed a genome-wide CRISPR/Cas9 knockout screen using this repetitive tumor stimulation system.[4] Primary human T cells from two human donors were transduced with the 1G4 TCR along with a genome-wide single-guide RNA (sgRNA) library[50], and Cas9 protein was introduced by electroporation.[4,5] We then exposed pooled Cas9-edited TCR-T cells to nine successive rounds of tumor cell stimulation in the presence of IL-2 (**Figure 2.2A**), which greatly exceeds the number of repeated tumor exposures in prior genome-wide screens in human T cells.[24,25] We maintained an effector to target (E:T) ratio of 1:1 for each stimulation until the bulk TCR-T cells could no longer effectively eliminate the tumor cells, indicating a reduction in their functional capacity. Pooled edited TCR-T cells were sequenced either before initial antigenic exposure (Time-Zero; T0) or after 4 rounds (Time-Intermediate; TI) or 9 rounds (Time-Final; TF) of antigenic stimulation. A parallel set of edited TCR-T cells was cultured for the duration of the screen with IL-2 but not exposed to tumor cells (TF_{ctrl}). We identified numerous sgRNAs enriched in TF when compared with T0 (**Figure 2.2B;** Supp. Tables 1-2), including sgRNAs targeting genes with established roles in T cell fitness and exhaustion (*RASA2*, *CISH*, *DNMT3A*, *MAPK14*, and the Cullin-5 complex members *CUL5* and *RNF7*)[5,51–54], as well as sgRNAs targeting subunits of Mediator (*MED15*, *MED16*, and *MED24*) and SWI/SNF (*SMARCD1*) — protein complexes highlighted by prior chronic stimulation screens.[25,55] Intriguingly, we also

discovered in our chronic stimulation screen strong enrichment for A20/*TNFAIP3* sgRNAs (rank 4; **Figure 2.2B**), a target that was not enriched in these prior screens. A20 sgRNAs were also highly correlated between T cell donors (**Figure 2.1D**). When we compared TF_{ctrl} with T0, A20 was ranked 4718th (**Figure 2.1E**), suggesting that the high rank in TF compared with T0 was specific to repetitive stimulation. Comparison of TI with T0 showed A20 was ranked 70th (**Figure 2.1E**), indicating a relative increase in the A20 persistence advantage with increasing chronic stimulation pressure.

We further investigated whether A20 ablation could enhance human T cell function in the setting of chronic antigen exposure. We edited 1G4 TCR-T cells either with an A20-targeted sgRNA not included in the initial screen (sgRNA-1) or with a control sgRNA targeting the AAVS1 safe harbor locus (Supp. Table 6). After acute TCR stimulation, A20-targeted ($A20^{KO}$) cells demonstrated a trend toward increased proliferative capacity (**Figure 2.1F**). Furthermore, after repeated stimulation, $A20^{KO}$ cells displayed improved tumor killing (**Figure 2.2C; Figure 2.1G**) and increased secretion of effector cytokines and cytotoxic granule proteins (**Figure 2.2D**) when compared with AAVS1 control cells. These findings suggest that $A20^{KO}$ TCR-T cells resist functional decline induced by chronic antigenic exposure.

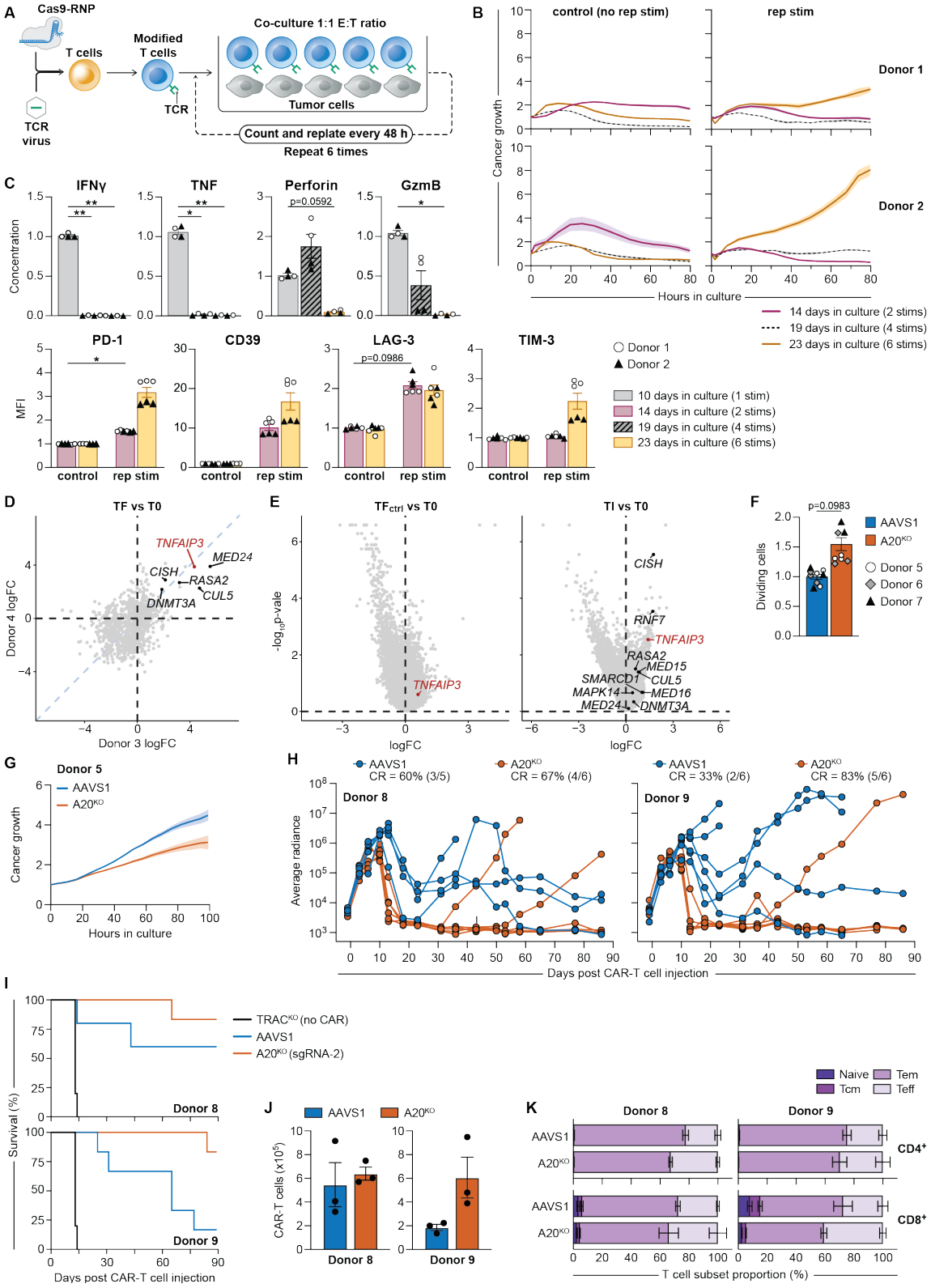

Figure 2.1 A20 is a key regulator of human T cell dysfunction upon chronic antigen stimulation.

(Figure caption continued on the next page)

(Figure caption continued from the previous page) **(A)** Schematic illustration of the human TCR-T cell repetitive stimulation assay. **(B)** Normalized cancer growth curves of NY-ESO-1$^+$ A375 melanoma target cells co-cultured with 1G4 TCR-T cells. Right panels depict co-cultures with TCR-T cells that had already undergone either 2, 4 or 6 rounds of repetitive tumor cell stimulation (rep stim; 14, 19 and 23 days in culture, respectively). Left panels depict co-cultures with control TCR-T cells that were matched for time in culture but had not undergone repetitive tumor cell stimulation (no rep stim). Effector:target (E:T) ratio = 1:1. Growth curves depict mean ± SEM of n = 3 technical replicates from n = 2 T cell donors. **(C)** (Top row) Normalized supernatant concentrations (pg/ml) of secreted effector molecules, as determined by LEGENDplex. Analysis shows TCR-T cells that had undergone either 1, 4, or 6 rounds of repetitive stimulation (10, 19 or 23 days in culture, respectively). (Bottom row) Normalized IR expression on TCR-T cells. Analysis shows TCR-T cells after 2 or 6 rounds of repetitive tumor antigenic stimulation (rep stim) compared with TCR-T cells matched for time in culture but not subjected to repetitive stimulation (control). MFI = median fluorescence intensity. Each technical replicate was normalized to the mean value of the control (no rep stim; bottom row) or 10 days in culture group (top row) for the corresponding donor. Bar graphs depict mean ± SEM of n = 2 donors, with n = 2-3 technical replicates per group per donor. Significance was assessed using paired t test. *$p < 0.05$; **$p < 0.01$. **(D)** Donor to donor correlation of TF versus T0. Highlighted genes include A20/*TNFAIP3* (red) and genes with known roles in T cell fitness (black). **(E)** Volcano plot comparing gene level scores from TF_{ctrl} versus T0 groups (left; n = 2 T cell donors) or from TI versus T0 groups (right; n = 1 T cell donor). Highlighted genes include A20/*TNFAIP3* (red) and genes with known roles in T cell fitness (black). **(F)** Normalized dividing TCR-T cells (CellTrace Violet^{lo}), as determined by proliferation assay after 72 h of stimulation. Each technical replicate was normalized to mean value of AAVS1 for corresponding donor. Bar graphs depict mean ± SEM of n = 3 donors with n = 3 technical replicates per group per donor. Significance was assessed by paired t test. **(G)** Normalized cancer growth curves of NY-ESO-1$^+$ A375 melanoma target cells. TCR-T cells after 5 rounds of repetitive stimulation were co-cultured with A375 cells at E:T ratio of 1:4. Growth curves depict mean ± SEM of n = 3 technical replicates from n = 1 T cell donor. **(H)** Individual NALM6 growth curves of mice treated with CAR-T cells. Left panel depicts different donor than that used in Figure 1F. Right panel depicts same donor as used in Figure 1F, but different sgRNA used to target A20^{KO}. n = 6 mice per group. CR = complete response. **(I)** Survival analysis for (H). Significance was assessed using a log-rank test. **(J)** Absolute numbers of total (CD4$^+$ and CD8$^+$ combined) CAR-T cells isolated from bone marrow of NALM6-bearing mice 14 days after CAR-T cell injection (mean ± SEM, n = 2 T cell donors, n = 3 mice per group per donor). Significance was assessed using unpaired t test with Welch's correction. **(K)** Differentiation status of CD4$^+$ or CD8$^+$ CAR-T cells from (e). Naive = CD45RA$^+$CD62L$^+$; central memory (Tcm) = CD45RA$^-$CD62L$^+$; effector memory (Tem) = CD45RA$^-$CD62L$^-$; effector (Teff) = CD45RA$^+$CD62L$^-$ (mean ± SEM, n = 2 T cell donors, n = 3 mice per group per donor). **(D,E)** Statistics were determined by MAGeCK analysis.

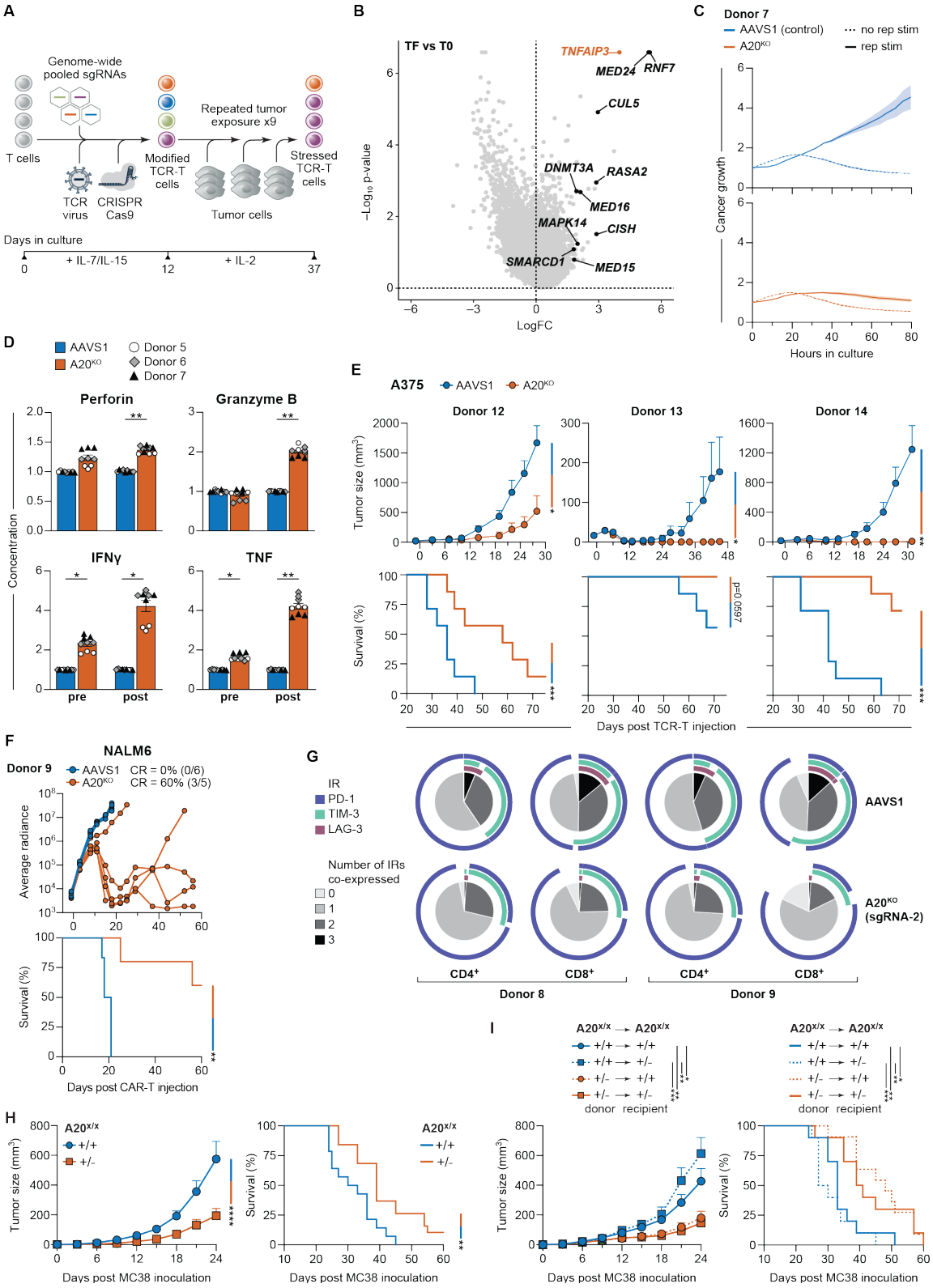

Figure 2.2 A genome-wide CRISPR perturbation screen identifies A20/TNFAIP3 as a key regulator of T cell dysfunction upon chronic antigen stimulation.

(Figure caption continued on the next page)

(Figure caption continued from the previous page) **(A)** Graphic depiction of genome-wide CRISPR screen. **(B)** Volcano plot portraying gene level scores for log fold change (FC; x axis) and p-value (y axis) generated by MAGeCK analysis for TF versus T0. Screen includes two human T cell donors. Highlighted genes include A20/TNFAIP3 (red) and genes with log FC ≥ 1.8 and known roles in T cell fitness (black). **(C)** Normalized growth curves of NY-ESO-1+ A375 melanoma target cells. 1G4 TCR-T cells without prior repetitive stimulation (no rep stim) or after 5 prior rounds of repetitive stimulation (rep stim) were co-cultured with A375 cells at an effector:target (E:T) ratio of 1:2. Curves depict mean ± SEM of n = 3 technical replicates from one of two T cell donors. **(D)** Normalized supernatant concentrations (pg/ml) of secreted effector granule proteins (top row) or cytokines (bottom row), as determined by LEGENDplex. TCR-T cells were analyzed before (pre) or after (post) 3 rounds of repetitive stimulation. Graphs depict mean ± SEM of n = 3 donors with n = 3 technical replicates per donor. Each technical replicate was normalized to mean of AAVS1 group for corresponding donor and condition. Significance was assessed using paired t test. **(E)** (Above) Averaged A375 growth curves in mice treated with 1G4 TCR-T cells. n = 7 mice per group using one T cell donor. (Below) Corresponding survival analysis. **(F)** (Above) Individual NALM6 growth curves in mice treated with CD19 CAR-T cells. n = 5 mice per group using one T cell donor. Radiance units = photons/s/cm2/steradian. (Below) Corresponding survival analysis. CR = complete response. **(G)** SPICE analyses of IR co-expression on CD4+ and CD8+ CAR-T cells isolated from bone marrow of NALM6-bearing mice. n = 3 mice per group per donor of n = 2 T cell donors. **(H)** Averaged MC38 growth (top) and survival (bottom) curves in A20 haploinsufficient (A20+/-) versus WT littermate (A20+/+) mice. n = 14-19 mice per group combined from three separate experiments. **(I)** Averaged MC38 growth (top) and survival (curves) in bone marrow chimeric mice of the indicated donor and recipient genotypes. n = 10-11 mice per group combined from two separate experiments. (E,F,H,I) Growth curves depict mean + SEM; significance was assessed using two-way ANOVA. Survival curve significance was assessed using a log-rank test. *p<0.05; **p<0.01; ***p<0.001; ****p<0.0001.

A20 ablation enhances ACT anti-tumor activity in vivo

To investigate whether A20 ablation could improve human ACTs *in vivo*, we challenged immunodeficient NOD-*scid* IL2Rγ^{null} (NSG) mice with A375 melanoma and treated with 1G4 TCR-T cells. Remarkably, mice that received A20^{KO} TCR-T cells suppressed A375 growth significantly better than recipients of AAVS1 TCR-T cells (**Figure 2.2E**). We then generated A20^{KO} or AAVS1 CD19 *TRAC*-CAR-T cells, where a CD19 CAR with a CD28 costimulatory endodomain is integrated into the *TRAC* locus, previously shown to outperform conventionally generated CAR-T cells.[17] We tested their ability to control CD19^{+} luciferase-expressing NALM6 B cell leukemia growth in NSG mice. Serial monitoring via bioluminescence imaging (BLI)

revealed that mice treated with $A20^{KO}$ CAR-T cells controlled NALM6 growth significantly better than recipients of AAVS1 CAR-T cells, and achieved a higher complete response (CR) rate (**Figure 2.2F**). We validated these findings using a different A20-targeted sgRNA (sgRNA-2; Supp. Table 6) and using two T cell donors (**Figure 2.1H-2.1I**). Upon flow cytometric profiling of bone marrow in treated mice, we discovered that only 18-29% of $A20^{KO}$ CAR-T cells co-expressed two or more IRs, compared with 40-51% of control AAVS1 CAR-T cells (**Figure 2.2G**). These findings suggest that $A20^{KO}$ CAR-T cells persist in more functional states than AAVS1 CAR-T cells *in vivo*. We further observed a trend toward increased numbers of $A20^{KO}$ CAR-T cells within the bone marrow TME (**Figure 2.1J**), but no clear alteration in memory phenotypes (**Figure 2.1K**). Overall, A20 ablation in human TCR-T or CAR-T cells potently enhances their ability to suppress tumor growth *in vivo*.

To test whether modulating A20 expression levels can limit anti-tumor immunity in immunocompetent settings, we compared the growth of MC38 – a widely used colon adenocarcinoma derived from C57BL/6 inbred mice and considered to be a "hot" tumor that responds well to immunotherapy – in heterozygous $A20^{+/-}$ mice and littermate control wild-type (WT; $A20^{+/+}$) mice. Of note, $A20^{+/-}$ mice appear grossly normal without spontaneous inflammation, but have reduced A20 expression and increased susceptibility to experimentally-induced inflammation[56,57]; homozygous $A20^{-/-}$ mice die perinatally and are hence not suitable for testing anti-tumor responses.[28] $A20^{+/-}$ mice consistently suppressed MC38 growth better than $A20^{+/+}$ littermates, with improved overall survival (**Figure 2.2H**). We next tested the anti-tumor efficacy of $A20^{+/-}$ haploinsufficiency in immune cells by generating bone marrow chimeric mice reconstituted with $A20^{+/-}$ versus $A20^{+/+}$ hematopoietic cells, and challenging these mice with MC38. Chimeras bearing $A20^{+/-}$ hematopoietic cells suppressed MC38 tumor growth better than

chimeras containing A20$^{+/+}$ hematopoietic cells (**Figure 2.2I**). Together, these findings show that reduction of A20 expression in hematopoietic cells enhances anti-tumor immunity. When combined with our human ACT results, they suggest that modulating A20 in T cells drives this superior anti-tumor immunity.

Inactivation of the zinc finger 7 domain of A20 invigorates anti-tumor immunity

Complete loss of A20 from cells can perturb both cellular activation and cell death responses in distinct cell types and differentiation states.[28,34,56,58,59] These disparate outcomes reflect the ability of A20 to regulate various ubiquitinated signaling complexes.[29,34,60] The A20 protein contains several structurally defined biochemical motifs that perform distinct biochemical functions (**Figure 2.3A**).[61–67] Selective mutation of individual A20 motifs may thus differentially impact T cell functions such as activation, differentiation, cytokine secretion, and/or survival. Accordingly, we sought to investigate the domains and associated biochemical functions of A20 that regulate acute T cell responses. We started with ESM1b, a protein large language model[8,68], and utilized a modified workflow capable of predicting the phenotypic consequences of missense variants throughout the genome.[8,68] Specific interrogation of the A20 open reading frame highlighted several hotspot regions within A20 where missense variants were predicted to have a high likelihood of functional impact (**Figure 2.3A**). To complement this approach with a defined functional outcome, we reanalyzed data from our large-scale BE screen in human T cells.[16] This screen utilized a massive sgRNA library tiled across the coding sequences of known regulators of T cell activity, including A20, to probe for missense mutations capable of enhancing T cell effector functions. Briefly, T cells were activated, transduced with BEs and sgRNAs, expanded in cytokines, and then restimulated. T cells with the highest level of activation (e.g., TNF production) upon restimulation were then flow-sorted and sequenced to

uncover enriched sgRNAs and their associated missense mutations. Analysis of this BE mutagenesis screen revealed sgRNAs that linked A20 missense mutations with enhanced TNF production by activated T cells (**Figure 2.3A**). Alignment of our ESM1b and BE screen analyses nominated three A20 domains as potentially critical for T cell functionality: the ovarian tumor ($A20^{OTU}$) domain, the seventh zinc finger motif ($A20^{ZF7}$), and to a lesser extent the fourth zinc finger motif ($A20^{ZF4}$) (**Figure 2.3A**). The $A20^{OTU}$ and $A20^{ZF4}$ domains harbor a deubiquitinase (DUB) and an E3 ubiquitin (Ub) ligase, respectively, and $A20^{ZF4}$ can also bind to K63 Ub chains.[27] The $A20^{ZF7}$ motif binds to M1 linked Ub chains, but has no known enzymatic activity.[13,66,67,69]

To understand how these A20 motifs regulate anti-tumor immunity *in vivo*, we leveraged our unique series of A20 knock-in (KI) mice carrying germline hypomorphic missense mutations that precisely abrogate the functions of either the $A20^{OTU}$, $A20^{ZF4}$, or $A20^{ZF7}$ motifs[29,30], leaving the remainder of the A20 protein intact. Of note, while $A20^{-/-}$ mice die shortly after birth, $A20^{OTU/OTU}$, $A20^{ZF4/ZF4}$, and $A20^{ZF7/ZF7}$ mice live over 8 months, thereby allowing us to analyze their responses to implanted tumors. Using the MC38 model, we found that tumor growth in $A20^{OTU}$ or $A20^{ZF4}$ KI mice matched that of wild-type (WT; $A20^{+/+}$) littermates (**Figure 2.3B**), arguing against a dominant role for these domains in regulating anti-tumor immunity. In striking contrast, both heterozygous $A20^{ZF7/+}$ and homozygous $A20^{ZF7/ZF7}$ mice exhibited significantly slower tumor growth and prolonged survival when compared with $A20^{+/+}$ littermates (**Figure 2.3B**). Notably, tumor growth did not diverge between $A20^{+/+}$ and $A20^{ZF7}$ KI mice until days 9-12 following tumor inoculation (**Figure 2.3B**). This timing hinted at an important role for the $A20^{ZF7}$ domain in regulating tumor-specific T cell responses, which typically require 7-10 days for naïve antigen-specific lymphocytes to become activated, proliferate, and differentiate into

effector cells. Moreover, after initial growth, MC38 tumor clearance was observed in 7% and 43% of $A20^{ZF7/+}$ and $A20^{ZF7/ZF7}$ mice, respectively. By contrast, no tumor clearance was observed in $A20^{+/+}$, $A20^{OTU}$ KI, or $A20^{ZF4}$ KI mice (**Figure 2.3C**). Thus, $A20^{ZF7}$ inactivation produces a robust anti-tumor immune response capable of sustained tumor rejection.

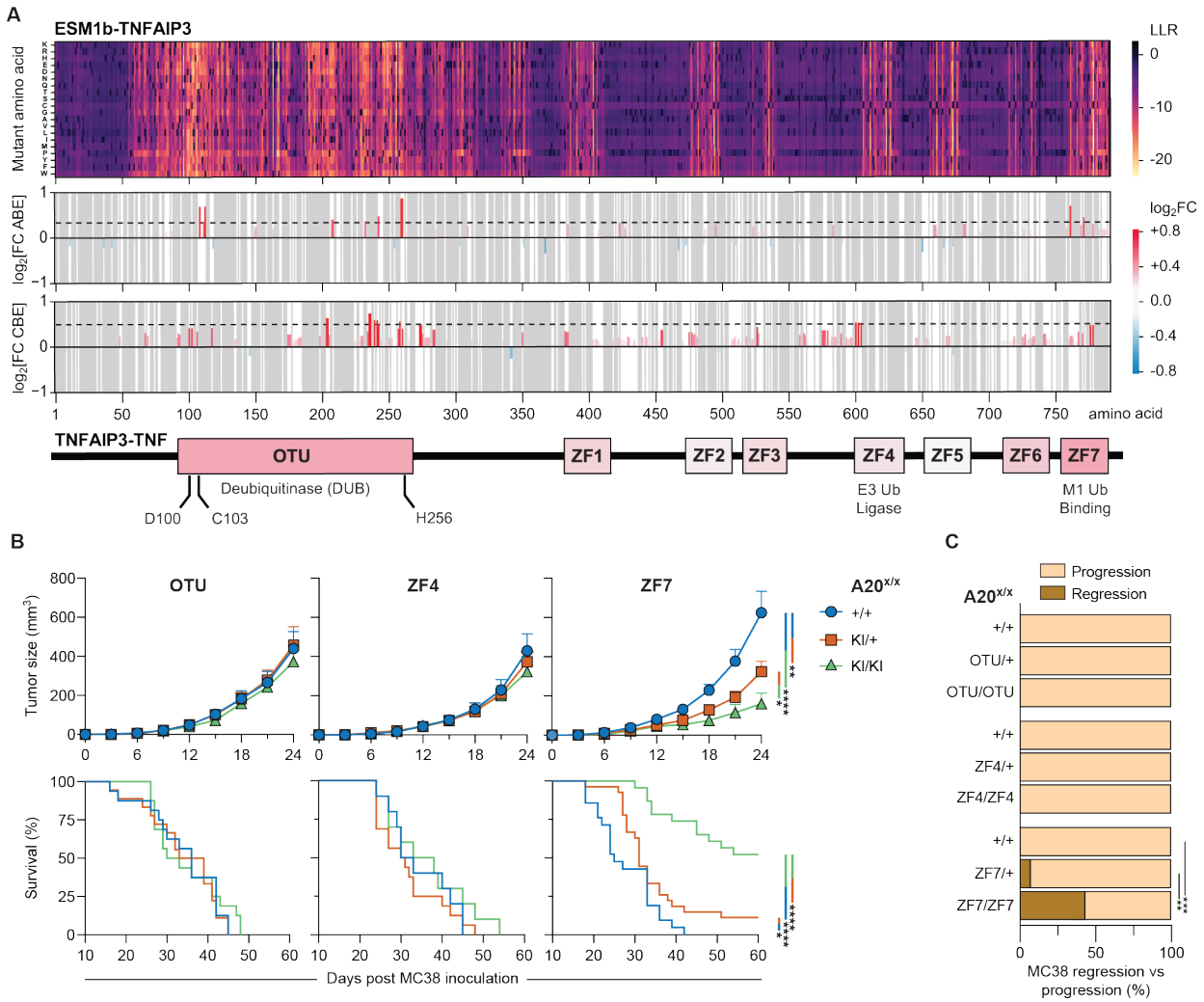

Figure 2.3 Inactivation of A20's zinc finger 7 domain invigorates anti-tumor immunity.
(A) (Top) Heatmap depicting ESM1b log likelihood ratio (LLR) score for all possible amino acid missense mutations (left) along the length of the A20 protein, with more negative score indicating greater likelihood of pathogenicity. (Middle) Average effects log_2FC on human T cell TNF production by missense mutation base-edits across the open reading frame of A20/*TNFAIP3*, using either adenine (ABE; above) or cytosine (CBE; below) base-editors. Red and blue indicate increased versus decreased TNF production over unedited cells, respectively. Dashed line indicates average log_2FC of all knockout guides within the ABE or CBE screen targeting the first 250 amino acids. Gray indicates amino acid residues not targeted by screen.
(Figure caption continued on the next page)

(Figure caption continued from the previous page) (Bottom) Annotated domains of A20 protein (UniProt), with box colors indicating average effect of base-edit screen guides targeting those domains. Annotation includes DUB catalytic triad of OTU domain (D100, C103, H256). Ub = ubiquitin. **(B)** (Above) Averaged MC38 growth curves in $A20^{OTU}$ (left), $A20^{ZF4}$ (middle), and $A20^{ZF7}$ (right) KI mice. Growth curves depict mean + SEM of n = 16-18 ($A20^{OTU}$), 10-16 ($A20^{ZF4}$) or 21-27 ($A20^{ZF7}$) mice per genotype combined from two to four independent experiments. Significance was assessed using two-way ANOVA or mixed-effects analysis. (Below) Corresponding survival analyses. Significance was assessed using a log-rank test. **(C)** Proportion of mice from (B) that exhibited MC38 clearance versus those that did not (progression). Significance was assessed using Fisher's exact test. *p<0.05; **p<0.01; ***p<0.001; ****p<0.0001.

The vigor of anti-tumor immune responses varies between tumor types and between host immune backgrounds. We therefore tested responses of $A20^{+/+}$, $A20^{ZF7/+}$ and $A20^{ZF7/ZF7}$ littermates to challenges with two additional heterotopic tumor models. We first used B16F10 melanoma, a C57BL/6 “cold” tumor that responds poorly to immunotherapy. As with MC38, both $A20^{ZF7/+}$ and $A20^{ZF7/ZF7}$ mice suppressed B16F10 tumor growth better than $A20^{+/+}$ littermates, accompanied by prolonged survival (**Figure 2.4A-2.4B**). Next, we used CT26 colon carcinoma, a “hot” tumor derived from BALB/c mice. BALB/c mice exhibit more robust type 2 immune responses characterized by IL-4, IL-5, and IL-13 expression, and less robust type 1 responses typified by IFNγ and TNF expression.[70] We backcrossed $A20^{ZF7}$ mice to BALB/c mice for seven generations and, upon challenge with CT26, again observed that both $A20^{ZF7/+}$ and $A20^{ZF7/ZF7}$ mice suppressed tumor growth better than $A20^{+/+}$ littermates (**Figure 2.4A-2.4B**). Hence, the $A20^{ZF7}$ domain restrains anti-tumor immunity against multiple tumor types and across divergent immune backgrounds.

Augmented primary anti-tumor immune responses can lead to enhanced memory responses. On the other hand, some genetic enhancements of acute CAR-T cell responses can compromise the durability of these responses, resulting in tumor relapse.[71] Also of note, A20 deficiency reduces memory T cell responses to bacterial infection.[36] We therefore investigated

whether A20$^{ZF7/ZF7}$ mice that cleared their primary tumor challenge also developed a robust anti-tumor memory response. We rechallenged these mice with four times the number of MC38 cells used in the primary challenge and compared tumor growth with age-matched A20$^{ZF7/ZF7}$ mice receiving their primary tumor challenge (i.e. naive to tumor; **Figure 2.4C**). As no A20$^{+/+}$ mice cleared their primary challenge, this genotype was not available for comparison in these experiments. Strikingly, A20$^{ZF7/ZF7}$ mice that cleared their primary tumor challenge nearly completely resisted their secondary challenge, with significantly less tumor growth and prolonged survival when compared to age-matched A20$^{ZF7/ZF7}$ mice receiving their primary tumor challenge (**Figure 2.4D**). Therefore, abrogation of the A20^{ZF7} motif also confers a strong memory anti-tumor immune response.

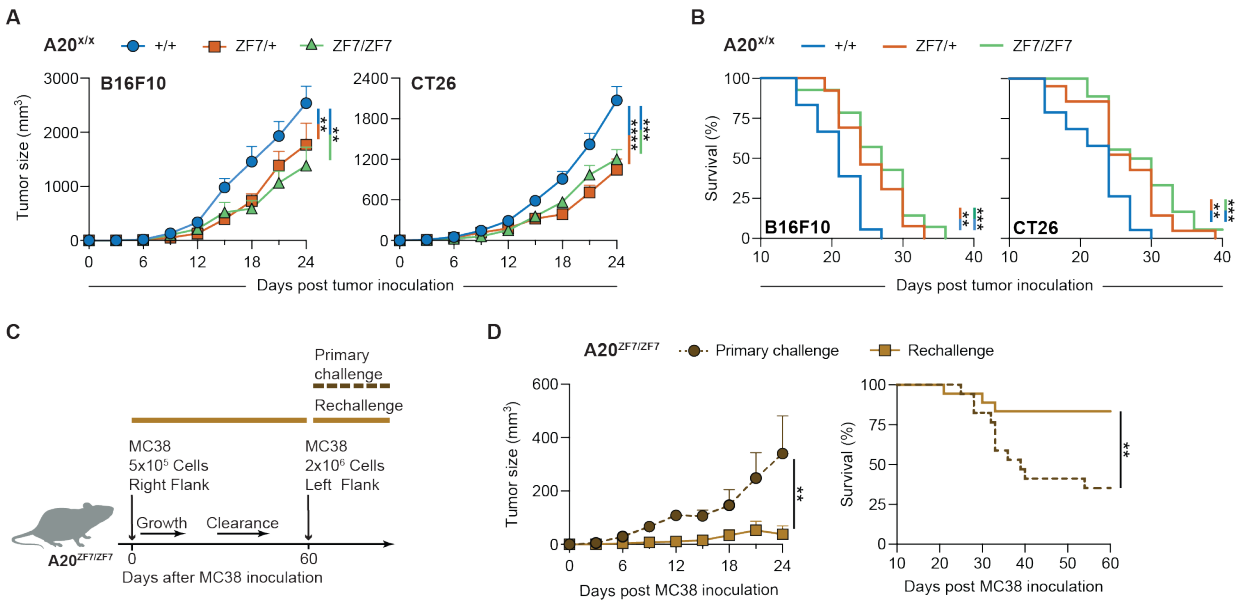

Figure 2.4 A20^{ZF7} inactivation augments anti-tumor immunity across tumor models and promotes anti-tumor memory.
(A) Averaged B16F10 (left) and CT26 (right) growth curves in A20^{ZF7} KI mice. n = 13-18 (B16F10) or 18-21 (CT26) mice per genotype combined from three independent experiments. **(B)** Survival analyses corresponding to (A). **(C)** Overview of workflow for MC38 rechallenge experiments of A20$^{ZF7/ZF7}$ mice that cleared their first challenge. **(D)** (Left) Averaged MC38 growth curves from A20$^{ZF7/ZF7}$ mice that cleared their initial challenge and were rechallenged with MC38, compared with age-matched A20$^{ZF7/ZF7}$ mice that were naive to tumor (primary challenge). (Figure caption continued on the next page)

(Figure caption continued from the previous page) n = 9-17 mice per group combined from three independent experiments. (Right) Corresponding survival analysis. **(A,B,D)** Growth curves depict mean + SEM; significance was assessed using two-way ANOVA. Survival significance was assessed using a log-rank test. **p<0.01; ***p<0.001; ****p<0.0001.

CD8$^+$ T cell-intrinsic A20^{ZF7} inactivation invigorates anti-tumor immunity

Mutation of A20^{ZF7} perturbs homeostasis of both innate and adaptive immune cells.[30] We thus investigated which immune cells are critical for the superior anti-tumor immunity of A20$^{ZF7/+}$ and A20$^{ZF7/ZF7}$ mice. We began by interbreeding A20^{ZF7} mice with *Rag1*$^{-/-}$ mice to remove B and T lymphocytes. RAG1 deficiency abolished the advantages in MC38 tumor suppression and survival of both A20$^{ZF7/+}$ and A20$^{ZF7/ZF7}$ mice (**Figure 2.5A**), while also eliminating tumor clearance (**Figure 2.5B**). The critical RAG1-dependent lymphocytes did not appear to be B cells or γδ T cells, as A20$^{ZF7/+}$ and A20$^{ZF7/ZF7}$ mice with genetic ablation of either B cells (*Ighm*$^{-/-}$ a.k.a. μMT) or γδ T cells (*Tcrd*$^{-/-}$) retained tumor suppression advantages over A20$^{+/+}$μMT and A20$^{+/+}$*Tcrd*$^{-/-}$ controls, respectively (**Figure 2.5A-2.5B**).

We therefore turned our attention to CD4$^+$ and CD8$^+$ T cells. When compared to isotype control-treated mice, antibody-mediated depletion of CD4$^+$ T cells greatly enhanced MC38 suppression and clearance in A20$^{+/+}$ and A20$^{ZF7/+}$ mice (**Figure 2.6A, 2.6C**), consistent with prior reports[72,73] and likely attributable to depletion of regulatory CD4$^+$ T cells (Tregs). Meanwhile, CD4$^+$ T cell depletion from A20$^{ZF7/ZF7}$ mice had minimal impact on MC38 suppression or clearance (**Figure 2.6A, 2.6C**), arguing against a major role for CD4$^+$ T cells in orchestrating superior anti-tumor immunity in these mice. Conversely, antibody-mediated depletion of CD8$^+$ T cells from A20$^{ZF7/+}$ and A20$^{ZF7/ZF7}$ mice completely abolished their advantages in tumor suppression and clearance (**Figure 2.6A, 2.6C**), as did genetic ablation of CD8$^+$ T cells (*Cd8a*$^{-/-}$; **Figure 2.6B-2.6C**). Of note, antibody-mediated CD8$^+$ T cell depletion had minimal impact on

MC38 growth in A20$^{+/+}$ mice (**Figure 2.6A**), suggesting their CD8^{+} TILs are not significantly contributing to tumor suppression, and are thus likely highly dysfunctional and potentially immunosuppressive.[74] Together these results highlight the centrality of CD8^{+} T cells to superior anti-tumor immunity in A20^{ZF7} KI mice.

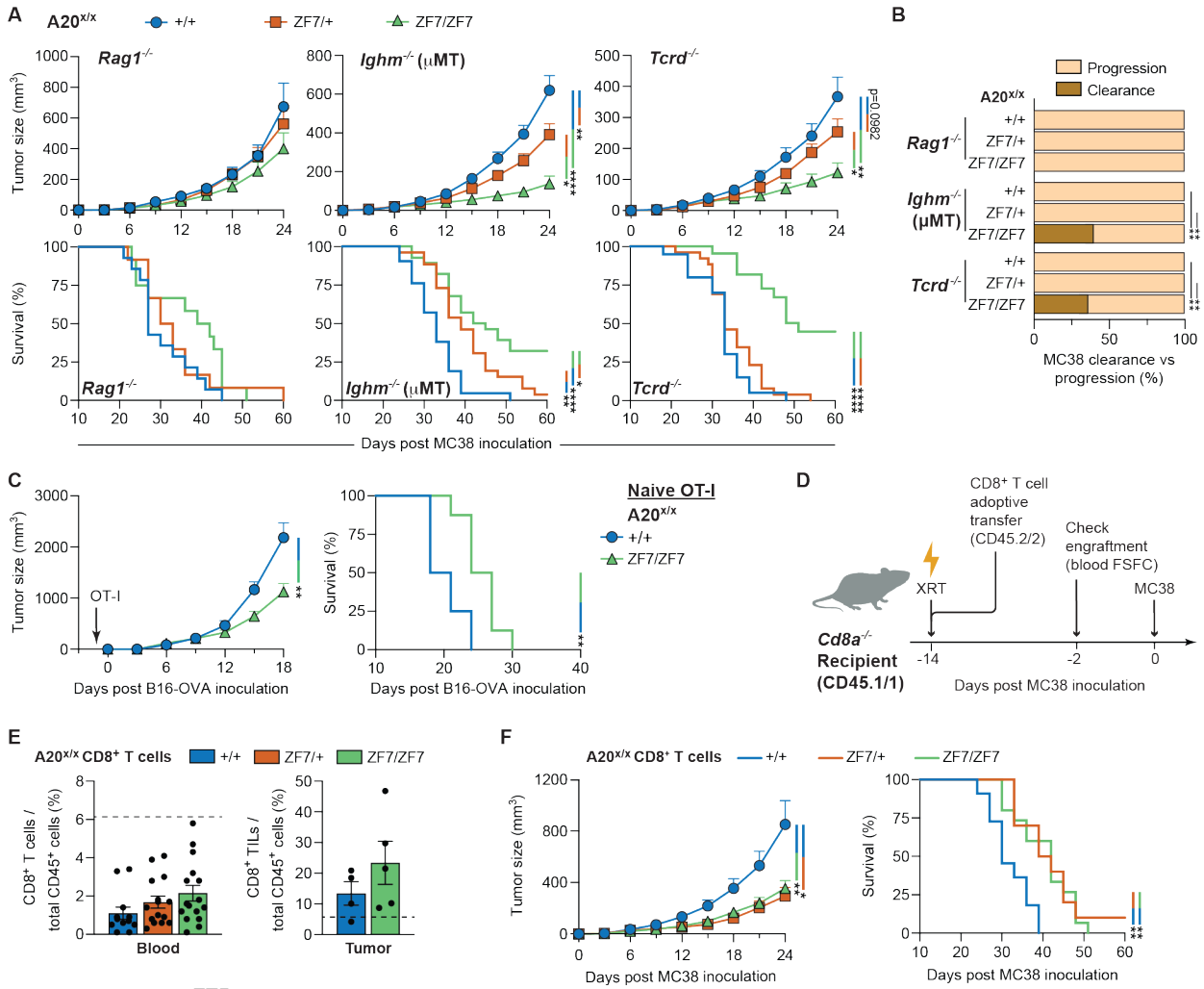

Figure 2.5 A20^{ZF7} inactivation specifically within CD8^{+} T cells augments anti-tumor immunity.

(A) (Above) Averaged MC38 growth curves from mice with indicated genetic ablation of lymphocyte subsets. (Below) Corresponding survival analyses. n = 12-14 (*Rag1*$^{-/-}$), 20-34 (μMT) or 20-26 (*Tcrd*$^{-/-}$) mice per genotype combined from three to five separate experiments. **(B)** Proportion of mice from (A) that exhibited MC38 clearance versus those that did not (progression). Significance was assessed using Fisher's exact test. **(C)** Averaged B16-OVA growth (left) and survival (right) curves from mice that received adoptive transfer of naïve OT-I cells. n = 8 mice per group combined from two separate experiments. (Figure caption continued on the next page)

(Figure caption continued from the previous page) **(D)** Overview of workflow for reconstitution of *Cd8a*$^{-/-}$ mice with CD8^{+} T cells. XRT = sublethal irradiation. FSFC = full spectrum flow cytometry. **(E)** Bar graphs depicting CD8^{+} T cell reconstitution of blood (left) and MC38 tumors (right) in *Cd8a*$^{-/-}$ mice. Blood dashed line represents mean blood CD8^{+} T cell proportion from 5 age-matched non-irradiated non-tumor-bearing WT (*Cd8a*$^{+/+}$) mice. Tumor dashed line represents mean CD8^{+} TIL density from day 12-15 tumors in WT (A20$^{+/+}$) mice (see Figure 4A). Bar graphs depict mean ± SEM of 4-16 mice per group from 1-2 independent experiments. Significance was assessed using one-way ANOVA (blood) or unpaired t test with Welch's correction (tumor). **(F)** (Left) Averaged MC38 growth curves of *Cd8a*$^{-/-}$ mice reconstituted with CD8^{+} T cells. n = 10-15 mice per group combined from two separate experiments. (Right) Corresponding survival analysis. **(A,C,D,G)** Growth curves depict mean + SEM; significance assessed using two-way ANOVA. Survival significance was assessed using log-rank test. *p<0.05; **p<0.01; ****p<0.0001.

We next investigated whether A20^{ZF7} inactivation specifically within CD8^{+} TILs could improve anti-tumor immunity. We interbred A20^{ZF7} KI mice with OT-I transgenic mice expressing a TCR specific for the ovalbumin peptide OVA.$^{257-264}$ We then adoptively transferred either naive A20$^{ZF7/ZF7}$ OT-I or control A20$^{+/+}$ OT-I cells (CD45.2) into congenic (CD45.1) WT hosts (**Figure 2.6D**). After challenging these host mice with OVA-expressing MC38 cells (MC38-OVA), we observed that recipients of naïve A20$^{ZF7/ZF7}$ OT-I cells suppressed tumor growth and prolonged survival better than recipients of A20$^{+/+}$ OT-I cells (**Figure 2.6D**). Similarly enhanced anti-tumor immunity was observed when naïve A20$^{ZF7/ZF7}$ OT-I cells were tested against B16-OVA melanoma (**Figure 2.5C**). We next employed an adoptive transfer model using pre-activated OT-I cells (**Figure 2.6E**). This model focuses specifically on OT-I effector phase functions, bypassing any potential differences that arise between A20$^{+/+}$ and A20$^{ZF7/ZF7}$ OT-I cells at the lymph node priming stage. Furthermore, this model more closely reflects ACT production. As with naive cells, adoptive transfer of pre-activated A20$^{ZF7/ZF7}$ OT-I cells outperformed A20$^{+/+}$ OT-I cells (**Figure 2.6E**).

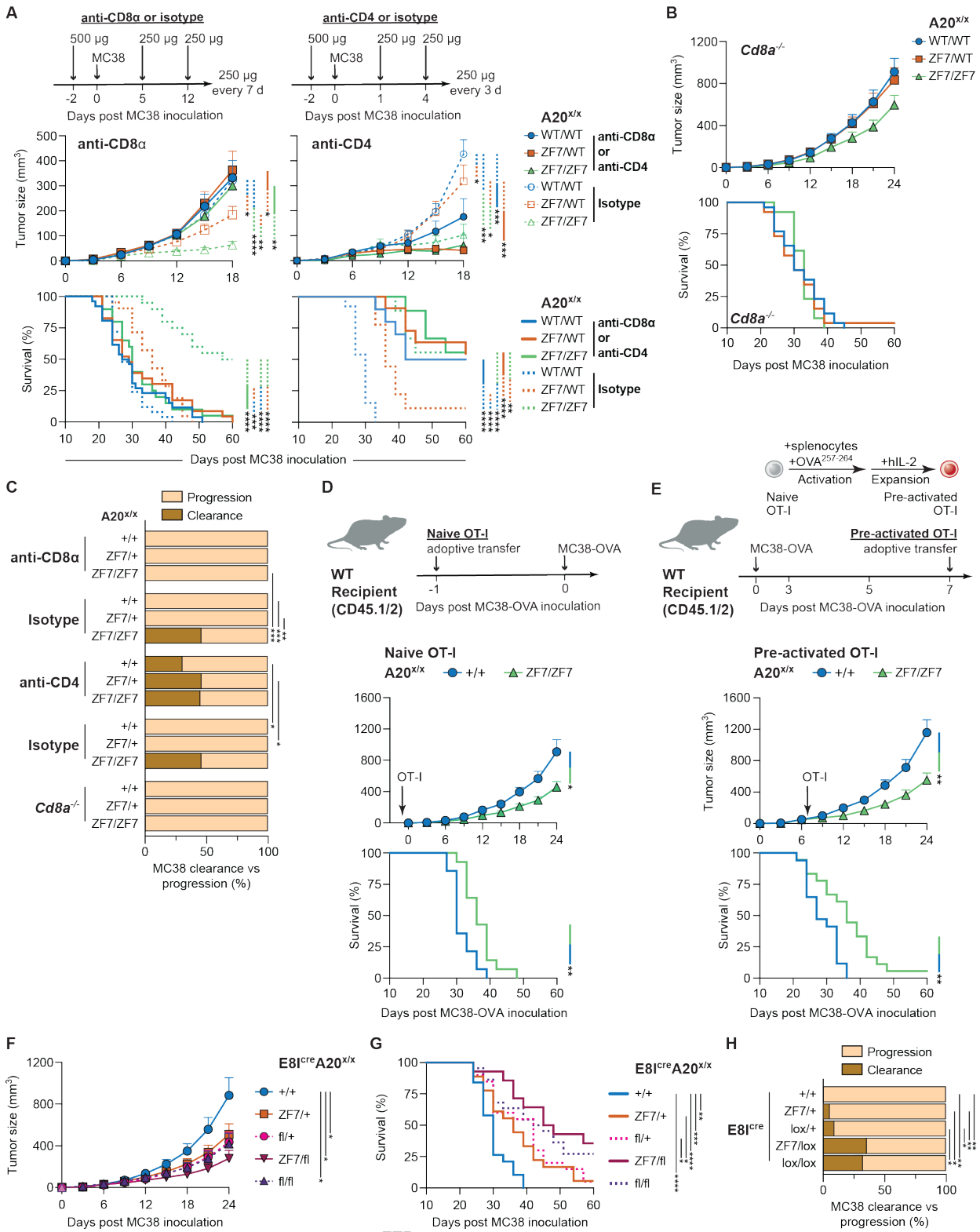

Figure 2.6 CD8$^+$ T cell-intrinsic A20^{ZF7} inactivation invigorates anti-tumor immunity.
(A) Averaged MC38 growth (top) and survival (bottom) curves from A20^{ZF7} KI mice with indicated antibody-mediated CD4$^+$ T cell (anti-CD4) or CD8$^+$ T cell (anti-CD8α) depletion. (Figure caption continued on the next page)

(Figure caption continued from the previous page) Isotype = isotype control antibody for anti-CD4 or anti-CD8α. n = 9-13 (anti-CD4) or 20-26 (anti-CD8α) mice per group combined from two (anti-CD4) or four (anti-CD8α) independent experiments. **(B)** Averaged MC38 growth (top) and survival (bottom) curves from $A20^{ZF7}$ KI mice with genetic $CD8^+$ T cell ablation (*Cd8a*$^{-/-}$). n = 13-26 mice per genotype combined from three separate experiments. **(C)** Proportion of mice from (A) and (B) that exhibited MC38 clearance versus those that did not (progression). **(D)** Averaged MC38-OVA growth (above) and survival (below) curves from mice that received adoptive transfer of naive OT-I cells. n = 14 mice per group combined from three separate experiments. **(E)** Averaged MC38-OVA growth (above) and survival (below) curves from mice that received adoptive transfer of pre-activated OT-I cells. n = 17-18 mice per group combined from three separate experiments. **(F)** Averaged MC38 growth curves from $E8I^{cre}$ mice interbred with mice carrying floxed A20 ($A20^{fl}$) and/or $A20^{ZF7}$ KI alleles. n = 19-25 mice per genotype combined from four separate experiments. **(G)** Survival curves from (F). **(H)** Proportion of mice from (F) that exhibited MC38 clearance versus progression. **(A,B,D,E,F,G)** Growth curves depict mean + SEM; significance was assessed using two-way ANOVA. Survival curve significance was assessed using log-rank test. **(C,H)** Significance was assessed using Fisher's exact test. *p<0.05; **p<0.01; ***p<0.001; ****p<0.0001.

To test the ability of $A20^{ZF7}$ KI $CD8^+$ T cells to kill MC38 tumors via the recognition of endogenous tumor antigens, we took two separate approaches. First, we utilized *Cd8a*^{cre} (a.k.a. $E8I^{cre}$) mice crossed with $A20^{ZF7}$ KI mice and/or floxed A20 mice ($A20^{fl}$) to generate mice with either $CD8^+$ T cell-restricted A20 deficiency ($E8I^{cre}A20^{fl/fl}$ mice) or $A20^{ZF7}$ hemizygosity ($E8I^{cre}A20^{ZF7/fl}$ mice). $E8I^{cre}A20^{fl/fl}$ mice outperformed $E8I^{cre}A20^{+/+}$ littermates in tumor growth suppression (**Figure 2.6F-2.6G**) and achieved a clearance rate comparable to $A20^{ZF7/ZF7}$ mice (27%; **Figure 2.6H**), confirming that $A20^{KO}$ $CD8^+$ T cells boost anti-tumor immunity.[38–40] Remarkably, $E8I^{cre}A20^{ZF7/fl}$ mice also demonstrated a clearance rate equivalent to $E8I^{cre}A20^{fl/fl}$ mice (36%; **Figure 2.6H**), and prolonged mouse survival to a greater extent than $E8I^{cre}A20^{ZF7/+}$ or $E8I^{cre}A20^{fl/+}$ mice (**Figure 2.6G**), indicating that $A20^{ZF7}$ hemizygosity within $CD8^+$ T cells promotes anti-tumor immunity. Second, we reconstituted *Cd8a*$^{-/-}$ mice (CD45.1) with congenic (CD45.2) polyclonal $CD8^+$ T cells (**Figure 2.5D**). Using sublethal irradiation prior to adoptive transfer, we achieved durable engraftment of the transferred $CD8^+$ T cells (**Figure 2.5E**). Importantly, *Cd8a*$^{-/-}$ mice reconstituted with either $A20^{ZF7/+}$ or $A20^{ZF7/ZF7}$ $CD8^+$ T cells

suppressed MC38 growth significantly better than *Cd8a*$^{-/-}$ mice reconstituted with control A20$^{+/+}$ CD8^{+} T cells (**Figure 2.5F**). Taken together, these data show that abrogating the A20^{ZF7} motif specifically within CD8^{+} T cells enhances anti-tumor immunity.

A20^{ZF7} inactivation alleviates terminal exhaustion of CD8^{+} T cells

To understand how A20^{ZF7} regulates CD8^{+} TILs, we analyzed CD8^{+} TILs from tumors in A20$^{+/+}$, A20$^{ZF7/+}$ and A20$^{ZF7/ZF7}$ mice by full spectrum flow cytometry (FSFC) 12-15 days after tumor inoculation. This time point was chosen to allow enough time for mice to mount an adaptive immune response, while still maintaining similar tumor sizes across genotypes. We initially observed no significant difference in total CD8^{+} TIL density within A20$^{+/+}$ versus A20^{ZF7} KI mice, a finding that was consistent across tumor models (**Figure 2.7A**). We next investigated CD8^{+} TIL subsets, as differences in CD8^{+} T cell differentiation can impact anti-tumor immunity. CD8^{+} TILs can be broadly defined as Tex (PD-1^{+}) or PD-1^{-} cells, and Tex can be further divided into progenitor exhausted (Tpex) and terminally exhausted (Ttex) subsets (**Figure 2.7B**).[23,75,76] Tpex have stem-like features but possess minimal cytotoxic potential, and are defined by expression of TCF-1 (**Figure 2.7B**). Tpex ultimately differentiate into Ttex[21,23], characterized by loss of TCF-1 expression, upregulation of the IR TIM-3 (**Figure 2.7B**), and increased expression of TOX. Ttex increase their expression of cytotoxic molecules but remain hypofunctional, as TOX orchestrates upregulation of various additional IRs and epigenetic silencing of T cell effector genes.[77–79] In MC38 and CT26 tumors, we did not find any significant differences in the distribution of these CD8^{+} TIL subsets across genotypes, while in B16F10 tumors we observed a greater proportion of Ttex in A20$^{ZF7/ZF7}$ mice (**Figure 2.7C**). Overall, quantitative differences in CD8^{+} TIL subsets cannot fully explain superior anti-tumor immunity in A20^{ZF7} KI mice.

We next interrogated memory phenotypes of $CD8^+$ TIL subsets. Intriguingly, in later-stage (day 24) MC38 tumors, we discovered a significant increase in $A20^{ZF7/ZF7}$ $CD8^+$ TILs bearing a tissue resident memory ($CD69^+CD103$; Trm) phenotype (**Figure 2.8A**), which could explain in part their robust anti-tumor memory response (**Figure 2.4D**). Conversely, in day 12-15 MC38 tumors, we did not observe any differences among $CD8^+$ TILs bearing a Trm or central memory ($CD62L^+$; Tcm) phenotype (**Figure 2.8B**). Thus, at this early time point, memory $CD8^+$ T cell differentiation is unlikely to account for the superior anti-tumor immunity of $A20^{ZF7/ZF7}$ mice.

We therefore turned our attention to exhaustion by profiling the expression of IRs (2B4, CD39, ICOS and LAG-3) and TOX. With few exceptions, the fraction of $PD\text{-}1^-$ TILs and Tpex that expressed these markers within MC38 tumors was similar across genotypes (**Figure 2.7D-2.7E**). In striking contrast, a significantly lower percentage of $A20^{ZF7/ZF7}$ Ttex expressed IRs or TOX when compared with $A20^{+/+}$ and $A20^{ZF7/+}$ Ttex (**Figure 2.7D-2.7E**). Similar findings were observed in $A20^{ZF7/ZF7}$ Ttex from B16F10 and CT26 tumors (**Figure 2.8C**). Intriguingly, we also observed a marked increase in $KLRG1^+$ $A20^{ZF7/ZF7}$ Ttex across tumor models (**Figure 2.7F-2.7G**), which notably had lower IR expression than $KLRG1^-$ $A20^{ZF7/ZF7}$ Ttex (**Figure 2.7H**). KLRG1 identifies short-term effector $CD8^+$ T cells, and is not commonly seen expressed on Ttex[80,81]. These phenotypic differences were not present in $A20^{OTU/OTU}$ or $A20^{ZF4/ZF4}$ Ttex (**Figure 2.8D**). Thus, $A20^{ZF7}$ inactivation alters $CD8^+$ Ttex such that they appear less exhausted.

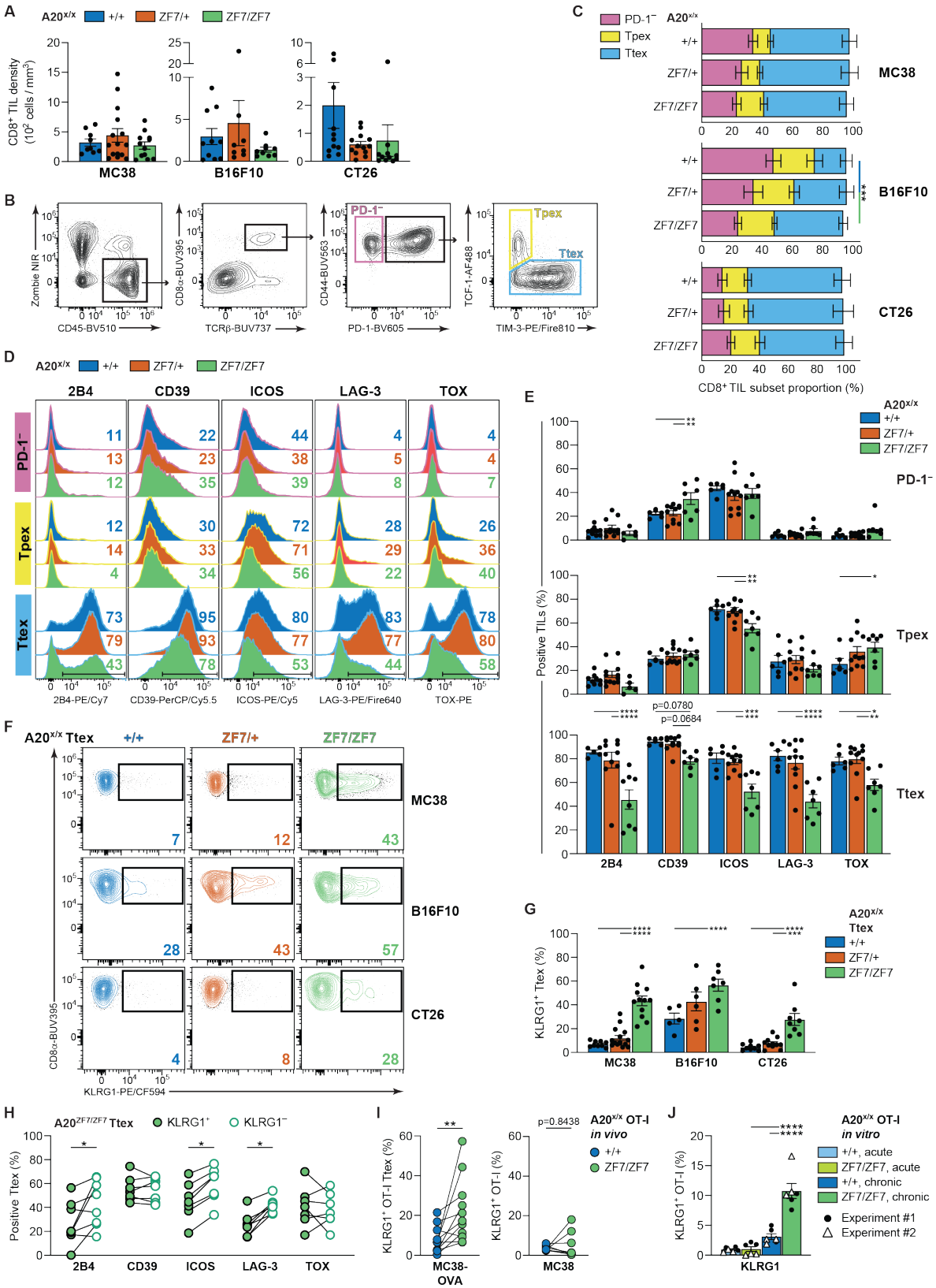

Figure 2.7 A20^{ZF7} inactivation alleviates terminal exhaustion of CD8^{+} T cells.
(Figure caption continued on the next page)

(Figure caption continued from the previous page) **(A)** Total intratumoral $CD8^+$ TIL density. n = 9-15 (MC38), 8-10 (B16F10), or 11-13 (CT26) samples per genotype combined from two to three separate experiments. **(B)** Gating strategy to identify $CD8^+$ TIL subsets. Contour plots represent 10 concatenated samples combined from $A20^{+/+}$, $A20^{ZF7/+}$ and $A20^{ZF7/ZF7}$ MC38 tumors from one experiment. **(C)** $CD8^+$ TIL subset proportions from (A). **(D)** IR or TOX expression by MC38 $CD8^+$ TIL subsets. Representative FSFC histograms depict 3-5 concatenated samples per genotype from one experiment. Inset = proportion (%) of cells within ranged gate. **(E)** Bar graphs showing proportion of $CD8^+$ TIL subsets — PD-1^- (top), Tpex (middle), or Ttex (bottom) — from (C) that express IRs or TOX. **(F)** Ttex KLRG1 expression. Representative contour plots from 3-5 concatenated samples per genotype from one experiment. Inset = proportion (%) of KLRG1-expressing cells. **(G)** Proportion of Ttex from (C) that express KLRG1. **(H)** Paired analysis of IR or TOX expression by $KLRG1^+$ versus $KLRG1^-$ $A20^{ZF7/ZF7}$ Ttex within MC38 tumors from (G). **(I)** Paired analysis of $A20^{+/+}$ versus $A20^{ZF7/ZF7}$ OT-I Ttex expression of KLRG1 following adoptive co-transfer of pre-activated OT-I cells. **(J)** KLRG1 expression by OT-I cells following *in vitro* repetitive (chronic) stimulation or acute stimulation alone, combining technical triplicates from two separate experiments. Significance was assessed using paired t test. **(A-G)** FSFC analyses of day 12-15 tumors. Significance was assessed using one-way ANOVA (A,G) or two-way ANOVA with Tukey's multiple comparisons test (C,E). **(H,I)** Each symbol/line pair represents cells from the same tumor. n = 6-10 samples combined from two to three independent experiments. Significance was assessed using Wilcoxon matched-pairs signed rank test. *$p<0.05$; **$p<0.01$; ***$p<0.001$; ****$p<0.0001$.

To test whether $A20^{ZF7}$ inactivation impacts $CD8^+$ TIL exhaustion in a truly cell autonomous manner, we adoptively co-transferred congenic pre-activated $A20^{+/+}$ OT-I (CD45.1/1) and $A20^{ZF7/ZF7}$ OT-I (CD45.2/2) cells into WT (CD45.1/2) recipient mice bearing MC38-OVA tumors (**Figure 2.8E**), then analyzed tumors 7 days later by FSFC. Both $A20^{+/+}$ and $A20^{ZF7/ZF7}$ OT-I TILs were present at similar densities and differentiated into Ttex (PD-1^{hi}TIM-3^+) in similar proportions (**Figure 2.8F-2.8G**). However, $A20^{ZF7/ZF7}$ OT-I Ttex displayed increased levels of KLRG1 (**Figure 2.7I**) and decreased levels of IRs and TOX (**Figure 2.8H**) when compared with $A20^{+/+}$ OT-I Ttex within the same TME, confirming the $CD8^+$ T cell-intrinsic role of $A20^{ZF7}$ inactivation in relieving the exhaustion phenotype.

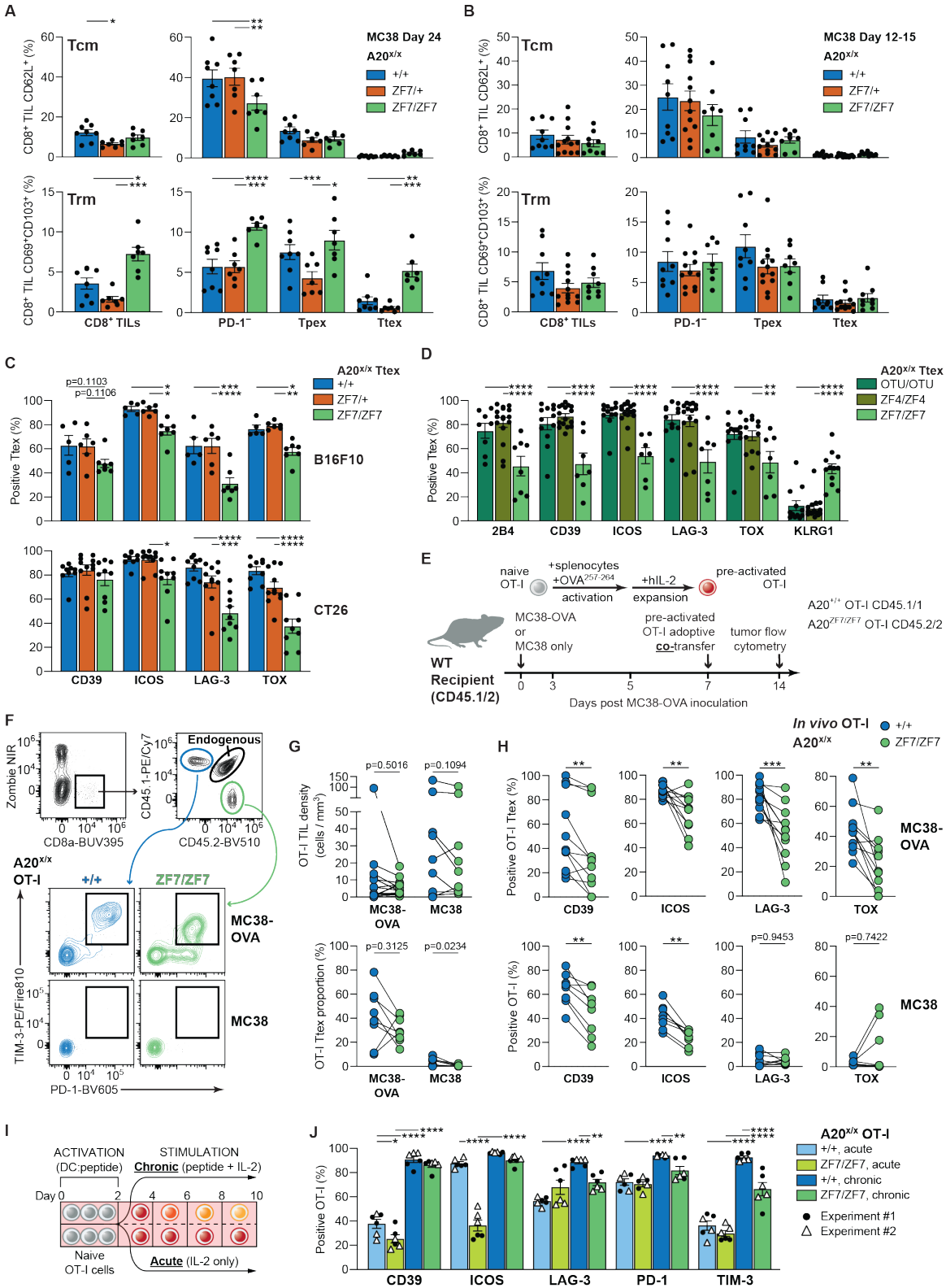

Figure 2.8 A20^{ZF7} inactivation alleviates terminal exhaustion following repetitive TCR stimulation.

(Figure caption continued on the next page)

(Figure caption continued from the previous page) **(A)** Proportion of day 24 MC38 total $CD8^+$ TILs (left) or TIL subsets (right) with phenotype suggestive of central memory (Tcm; $CD62L^+$; top) or tissue resident memory (Trm; $CD69^+CD103^+$; bottom) differentiation. n = 7-8 mice per genotype combined from two separate experiments. **(B)** As in (A), but from day 12-15 MC38 tumors. n = 8-12 tumors per genotype combined from two separate experiments. **(C)** IR or TOX expression by Ttex from B16F10 (top) or CT26 (bottom) tumors. n = 5-7 (B16F10) or 9-11 (CT26) mice per genotype combined from two or three separate experiments. **(D)** IR, TOX or KLRG1 expression by Ttex from MC38 tumors. n = 7-15 mice per genotype combined from two or three separate experiments. $A20^{ZF7/ZF7}$ data is repeated from Figure 2.7E and 4G for comparison. **(E)** Overview of workflow for adoptive OT-I co-transfer experiments. **(F)** Gating strategy to identify $A20^{+/+}$ (CD45.1/1) and $A20^{ZF7/ZF7}$ OT-I (CD45.2/2) Ttex in adoptive co-transfer experiments. Contour plots represent FSFC on 9 concatenated MC38-OVA and MC38 tumors from one experiment. Endogenous = endogenous MC38-OVA or MC38 $CD8^+$ TILs (CD45.1/2). **(G)** Paired analyses of OT-I TIL density (top) and proportion that differentiated into Ttex (bottom) within MC38 or MC38-OVA tumors. n = 7 samples combined from two experiments. **(H)** Paired analysis of IR and TOX expression by OT-I Ttex (MC38-OVA; top) or total OT-I TILs (MC38; bottom) following adoptive co-transfer. **(I)** Overview of workflow for *in vitro* acute versus chronic/repetitive stimulation assay. **(J)** IR expression by OT-I cells following *in vitro* acute or chronic stimulation. Bar graphs depict mean ± SEM of technical triplicates combined from two separate experiments. Significance was assessed using two-way ANOVA with Bonferroni's multiple comparisons test. **(A-H)** FSFC analyses from day 12-15 tumors, unless otherwise stated. All bar graphs show mean ± SEM. Significance was assessed using two-way ANOVA with Tukey's multiple comparisons test. **(G,H)** Each symbol/line pair represents cells retrieved from the same tumor. n = 9-11 samples combined from two separate experiments. Significance was assessed using Wilcoxon matched-pairs signed rank test. *p<0.05; **p<0.01; ***p<0.001; ****p<0.0001.

We next wanted to gain insight into whether these phenotypic differences in $A20^{ZF7/ZF7}$ Ttex truly required exhaustive (i.e. repetitive or chronic) TCR engagement, or were simply a byproduct of the initial (i.e. acute) TCR stimulus. We first repeated our adoptive co-transfer of pre-activated OT-I cells but replaced MC38-OVA tumor cells with MC38 tumors, thereby removing the *in vivo* antigenic stimulus and ensuring these OT-I cells were only acutely stimulated *in vitro*. Examination of OT-I TILs within MC38 tumors 7 days after adoptive co-transfer revealed densities comparable to that observed in MC38-OVA tumors (**Figure 2.8G**); however, almost all $A20^{+/+}$ and $A20^{ZF7/ZF7}$ OT-I TILs within MC38 tumors remained PD-1^-, with few differentiating into Ttex (**Figure 2.8F-2.8G**). As there were not enough OT-I Ttex of either genotype to analyze within MC38 tumors, we instead profiled IRs and TOX on total $A20^{+/+}$ and

$A20^{ZF7/ZF7}$ OT-I TILs. This analysis revealed minimal expression of KLRG1 on either $A20^{+/+}$ or $A20^{ZF7/ZF7}$ OT-I TILs (**Figure 2.7I**). Furthermore, LAG-3 and TOX expression remained equivalently low in $A20^{+/+}$ and $A20^{ZF7/ZF7}$ OT-I TILs (**Figure 2.8H**). Meanwhile, fewer $A20^{ZF7/ZF7}$ OT-I TILs in MC38 tumors expressed CD39 and ICOS than $A20^{+/+}$ OT-I TILs (**Figure 2.8H**), similar to our findings in MC38-OVA OT-I Ttex. Thus, several core $A20^{ZF7/ZF7}$ Ttex phenotypic differences (KLRG1, LAG-3, TOX) required chronic TCR engagement *in vivo*, while others were likely encoded following acute TCR stimulation (CD39, ICOS). To further support these findings, we submitted $A20^{+/+}$ and $A20^{ZF7/ZF7}$ OT-I cells to an *in vitro* repetitive/chronic stimulation assay benchmarked as a surrogate for exhaustion (**Figure 2.8I**).[82] For comparison, a parallel set of OT-I cells matched for time in culture received only acute stimulation (**Figure 2.8I**). As with our *in vivo* analysis, this assay revealed increased KLRG1 expression (**Figure 2.7J**), and decreased expression of several IRs (LAG-3, PD-1, TIM-3; **Figure 2.8J**), in chronically but not acutely stimulated $A20^{ZF7/ZF7}$ OT-I cells when compared to $A20^{+/+}$ OT-I cells. We also again observed lower expression of CD39 and ICOS on both acutely and chronically stimulated $A20^{ZF7/ZF7}$ OT-I cells when compared to $A20^{+/+}$ OT-I cells (**Figure 2.8J**). Together these results indicate that many of the key phenotypic differences observed in $A20^{ZF7/ZF7}$ Ttex versus WT Ttex require repetitive TCR engagement, while others require only acute stimulation.

Perforin, but not IFNγ or TNF, drives enhanced anti-tumor immunity in $A20^{ZF7/ZF7}$ mice

Reduced exhaustion in $A20^{ZF7/ZF7}$ Ttex may align with enhanced tumoricidal effector function, explaining the superior anti-tumor response of $A20^{ZF7/ZF7}$ mice. To define the relevant anti-tumor effector mechanisms unleashed in $A20^{ZF7}$ KI Ttex, we focused first on co-production of IFNγ and TNF, a commonly cited indicator of TIL dysfunction.[23,83,84] We observed a significant increase of $IFN\gamma^+$ TNF^+ Ttex in both $A20^{ZF7/+}$ and $A20^{ZF7/ZF7}$ mice upon *ex vivo* stimulation (**Figure 2.9A-**

2.9B), consistent with prior reports in A20^{KO} CD8^{+} TILs.[38–40] To test whether increased IFNγ or TNF production by A20^{ZF7} KI Ttex enhances anti-tumor immunity, we interbred A20^{ZF7} KI mice with *Ifng*$^{-/-}$ or *Tnf*$^{-/-}$ mice. Surprisingly, neither IFNγ or TNF deficiency alone were able to reverse the superior MC38 growth control and prolonged survival of A20$^{ZF7/+}$ and A20$^{ZF7/ZF7}$ mice when compared to A20$^{+/+}$ littermates (**Figure 2.9C**). In addition, A20$^{ZF7/ZF7}$*Ifng*$^{-/-}$ and A20$^{ZF7/ZF7}$*Tnf*$^{-/-}$ mice both showed tumor clearance rates similar to A20$^{ZF7/ZF7}$ mice (**Figure 2.9D**). To account for potential redundancies or compensatory actions between the anti-tumor activities of IFNγ and TNF, we interbred A20^{ZF7} mice with *Ifng*$^{-/-}$*Tnf*$^{-/-}$ mice that lack both cytokines. Interestingly, A20$^{ZF7/+}$*Ifng*$^{-/-}$*Tnf*$^{-/-}$ mice were no longer able to control tumor growth or prolong survival better than their A20$^{+/+}$*Ifng*$^{-/-}$*Tnf*$^{-/-}$ mice counterparts (**Figure 2.9C**), indicating that these cytokines together drive the superior tumor suppression observed in heterozygous A20$^{ZF7/+}$ mice. In striking contrast, homozygous A20$^{ZF7/ZF7}$*Ifng*$^{-/-}$*Tnf*$^{-/-}$ mice retained significant advantages in controlling tumor growth and prolonging survival when compared to A20$^{+/+}$*Ifng*$^{-/-}$ *Tnf*$^{-/-}$ mice, while maintaining a 45% clearance rate (**Figure 2.9C-2.9D**). These findings suggested the presence of an additional IFNγ/TNF-independent tumor growth suppression mechanism unlocked only in homozygous but not heterozygous A20^{ZF7} KI mice, i.e., only below a certain threshold of A20 activity.

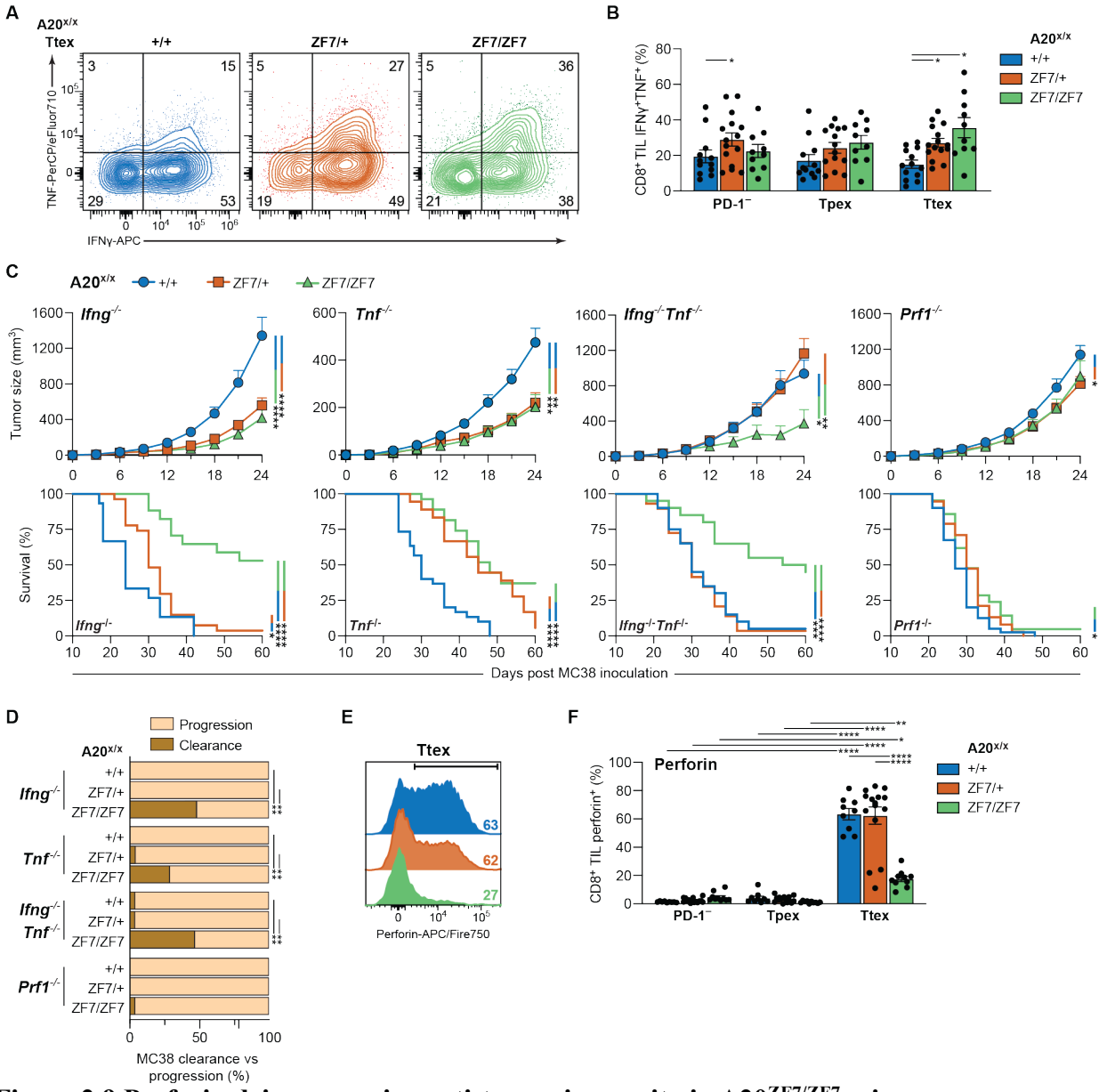

Figure 2.9 Perforin drives superior anti-tumor immunity in A20$^{ZF7/ZF7}$ mice.
(A) IFNγ and TNF expression by Ttex following *ex vivo* stimulation with PMA and ionomycin. Representative contour plots depict 2-4 concatenated samples per genotype from one experiment. Inset = proportion (%) of Ttex in that quadrant. **(B)** Proportion of IFNγ^{+}TNF^{+} cells by CD8^{+} TIL subset. n = 10-15 mice per genotype combined from three separate experiments. **(C)** Averaged MC38 growth (top) and survival (bottom) curves from A20^{ZF7} KI mice with indicated genetic ablation of IFNγ (*Ifng*$^{-/-}$) and/or TNF (*Tnf*$^{-/-}$) versus perforin (*Prf1*$^{-/-}$). Growth curves depict mean + SEM of 15-27 (*Ifng*$^{-/-}$), 18-30 (*Tnf*$^{-/-}$), 20-29 (*Ifng*$^{-/-}$*Tnf*$^{-/-}$), or 21-40 (*Prf1*$^{-/-}$) mice combined from three or more separate experiments. **(D)** Proportion of mice from (C) that exhibited MC38 clearance versus those that did not (progression). Significance was assessed using Fisher's exact test. **(E)** Ttex perforin expression in MC38 tumors. Representative FSFC histograms depicting 3-5 concatenated samples per genotype from one experiment. **(F)** Proportion of perforin-expressing cells within each CD8^{+} TIL subset. (Figure caption continued on the next page)

Figure caption continued from the precious page. n = 9-15 mice per genotype combined from three separate experiments. **(A,B,E,F)** FSFC analyses of day 12-15 MC38 tumors. Bar graphs depict mean ± SEM. Significance was assessed using two-way ANOVA with Tukey's multiple comparisons test. *p<0.05; **p<0.01; ***p<0.001; ****p<0.0001.

$CD8^+$ TILs can also kill target cells via exocytosis of cytotoxic granules (i.e. degranulation) that contain perforin and granzymes. Perforin disrupts target cell membranes to facilitate granzyme entry, and granzymes in turn trigger cell death pathways.[85] Notably, perforin and granzymes appear to be required for tumor suppression in some tumor models, but not others.[41–48] We thus evaluated the perforin-granzyme signaling axis for its role in $A20^{ZF7}$ anti-tumor immunity by crossing $A20^{ZF7}$ KI mice with perforin knockout (*Prf1*$^{-/-}$) mice. Perforin deficiency, unlike IFNγ and/or TNF deficiency, abolished the superior tumor growth control and clearance rate of $A20^{ZF7/ZF7}$ mice (**Figure 2.9C-2.9D**). Importantly, perforin deficiency did not alter $CD8^+$ TIL density, $CD8^+$ TIL subset distribution, or markers of T cell exhaustion in $A20^{+/+}$, $A20^{ZF7/+}$ or $A20^{ZF7/ZF7}$ mice (**Figure 2.10A-2.10C**). Therefore, perforin mediates enhanced anti-tumor immunity in $A20^{ZF7/ZF7}$ mice without perturbing $CD8^+$ TIL numbers or differentiation.

$A20^{ZF7}$ inactivation unleashes perforin degranulation by exhausted $CD8^+$ T cells

The superior perforin-dependent anti-tumor cytotoxicity of $A20^{ZF7/ZF7}$ mice could result from increased perforin expression by $CD8^+$ TILs. We therefore assessed $CD8^+$ TIL perforin expression by FSFC which, unlike most cytokines, can be detected without *ex vivo* stimulation. Among $CD8^+$ TILs, regardless of genotype, perforin expression was largely confined to Ttex (**Figure 2.9E-2.9F**). These findings align with prior reports of elevated perforin and granzyme levels in Ttex.[21–23,86,87] Surprisingly, while $A20^{+/+}$ and $A20^{ZF7/+}$ Ttex exhibited similarly high proportions of perforin-expressing cells, we observed an unexpected *reduction* in the numbers of perforin-expressing $A20^{ZF7/ZF7}$ Ttex when compared to $A20^{+/+}$ Ttex (**Figure 2.9E-2.9F**). Perforin

expression was also reduced in A20$^{ZF7/ZF7}$ Ttex from B16F10 and CT26 tumors (**Figure 2.10D**), but was not reduced in A20$^{OTU/OTU}$ or A20$^{ZF4/ZF4}$ Ttex from MC38 tumors (**Figure 2.10E**). These findings highlight a paradox wherein biallelic A20^{ZF7} inactivation unleashes perforin-dependent anti-tumor cytotoxicity, yet engenders fewer perforin-expressing Ttex.

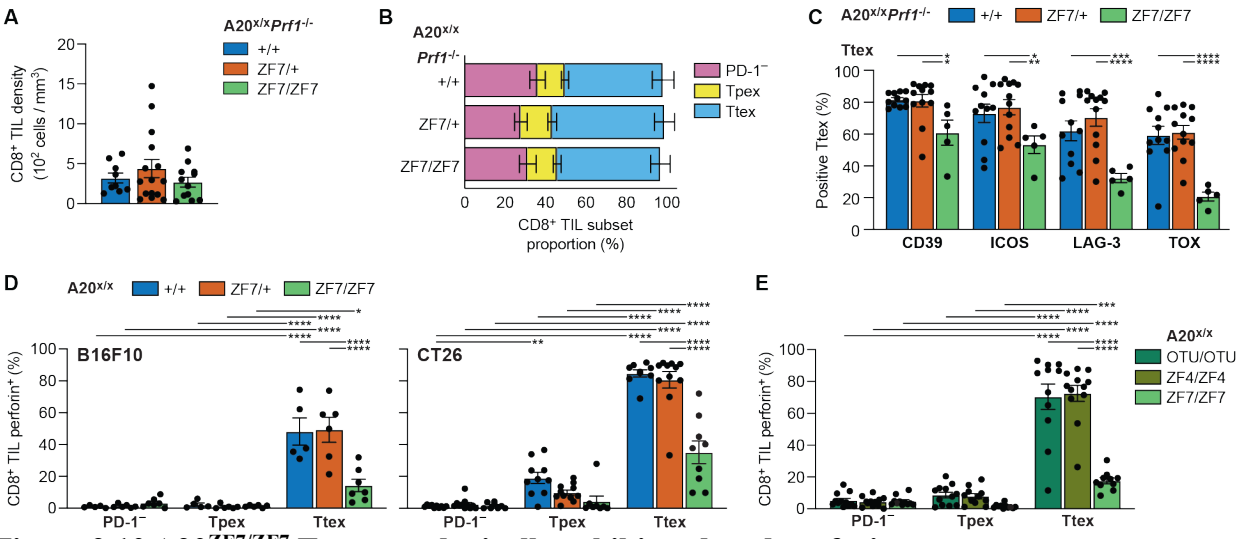

Figure 2.10 A20$^{ZF7/ZF7}$ Ttex paradoxically exhibit reduced perforin.
(A) Total MC38 CD8$^+$ TIL density in *Prf1*$^{-/-}$ mice. n = 9-15 mice per genotype combined from three separate experiments. **(B)** CD8$^+$ TIL subset proportions from (A). **(C)** Ttex IR and TOX expression from (B). **(D)** Perforin expression by CD8$^+$ TIL subsets within B16F10 (left) or CT26 (right) tumors. **(E)** Perforin expression by CD8$^+$ TIL subsets in MC38 tumors. A20$^{ZF7/ZF7}$ data is repeated from Figure 2.9F for comparison. **(A-E)** FSFC analyses of day 12-15 tumors. Bar graphs depict mean + SEM. Significance was assessed using one-way ANOVA (A) or two-way ANOVA with Tukey's multiple comparison's test (B-E). *p<0.05; **p<0.01; ***p<0.001; ****p<0.0001.

Diminished perforin expression by A20$^{ZF7/ZF7}$ Ttex could result from reduced production or from enhanced degranulation. To distinguish between these possibilities, we first measured side scatter area (SSC-A) as an indicator of cellular complexity which, in the case of CD8$^+$ T cells, likely reflects granule content. We observed that SSC-A was greatly increased in Ttex when compared to PD-1$^-$ and Tpex subsets across genotypes (**Figure 2.12A**), suggesting that the perforin-expressing Ttex subset also harbored the most granules. Accordingly, we uncovered a strong positive correlation between Ttex perforin expression and SSC-A (**Figure 2.12B**). As with

perforin, SSC-A was significantly reduced in $A20^{ZF7/ZF7}$ Ttex when compared to $A20^{+/+}$ and $A20^{ZF7/+}$ Ttex (**Figure 2.12A**), suggesting reduced cytotoxic granule content. Next, we measured the capacity of Ttex to manufacture perforin protein. We stimulated dissociated MC38 tumors *ex vivo* with phorbol 12-myristate 13-acetate (PMA) and ionomycin in the presence of brefeldin to block intracellular vesicle transport and, by extension, inhibit degranulation. Using this approach, we discovered that a similarly high fraction of $A20^{ZF7/ZF7}$ Ttex expressed perforin as compared to $A20^{+/+}$ and $A20^{ZF7/+}$ Ttex (**Figure 2.11A**). Thus, $A20^{ZF7/ZF7}$ Ttex are capable of equivalent perforin production, at least in these pharmacologically stimulated cells.

To quantify Ttex perforin content in their native TME without additional stimulation, we treated MC38-bearing mice for 6 hours *in vivo* with brefeldin or vehicle control[88], then analyzed tumors by FSFC. This experiment revealed several important facets of perforin degranulation by $A20^{+/+}$ and $A20^{ZF7}$ KI $CD8^+$ TILs. Most strikingly, brefeldin treatment led to a marked increase in the fraction of $perforin^+$ $A20^{ZF7/ZF7}$ Ttex when compared to vehicle treatment, rising to levels that matched those of $A20^{+/+}$ and $A20^{ZF7/+}$ Ttex (**Figure 2.11B**), indicating that many $A20^{ZF7/ZF7}$ Ttex are likely degranulating perforin in the absence of brefeldin.

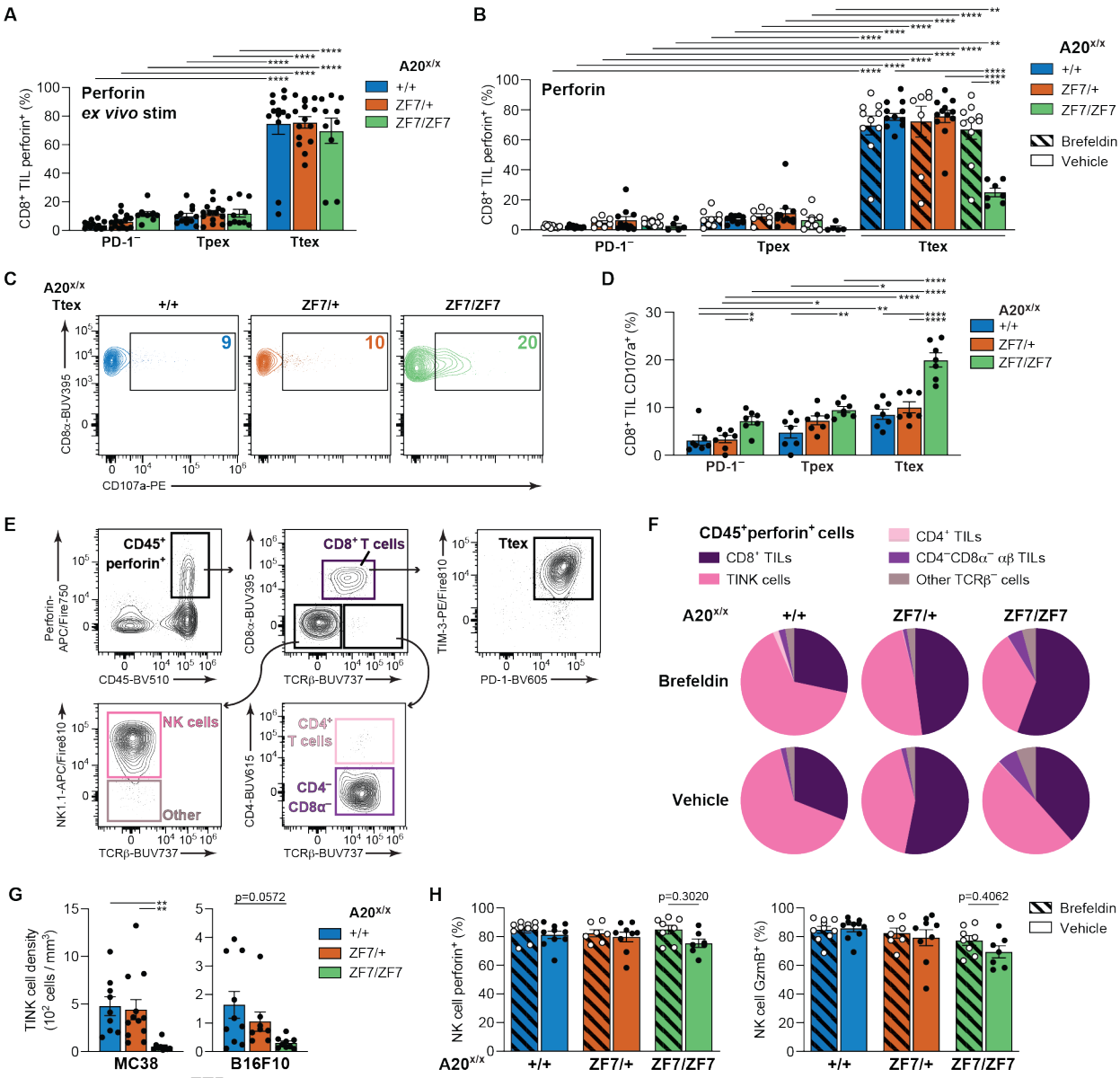

Figure 2.11 A20^{ZF7} inactivation unleashes Ttex perforin degranulation.

(A) Perforin expression by CD8$^+$ TIL subsets after 6 h *ex vivo* stimulation with PMA, ionomycin and brefeldin. n = 10-15 mice per genotype combined from three separate experiments. **(B)** Proportion of perforin-expressing CD8$^+$ TILs in mice treated *in vivo* for 6 h with either brefeldin or vehicle control (5% DMSO). n = 5-12 mice per group combined from two separate experiments. **(C)** CD107a surface expression by Ttex following *ex vivo* stimulation for 1 h with PMA, ionomycin, brefeldin and monensin. Contour plots depict one representative sample per genotype from one experiment. Inset = proportion (%) of CD107a$^+$ Ttex. **(D)** CD8$^+$ TIL subset surface expression of CD107a, related to (C). n = 7 mice per genotype combined from two separate experiments. **(E)** Gating strategy to identify perforin-expressing cells within tumors, related to (B). Contour plots depict eight concatenated A20$^{+/+}$, A20$^{ZF7/+}$, and A20$^{ZF7/ZF7}$ brefeldin-treated mice from one experiment. **(F)** Proportion of perforin-expressing cells by subset, related to (E). Pie charts depict mean for each cell subset in brefeldin- versus vehicle-treated mice from (B). (Figure caption continued on the next page)

Figure caption continued from the preious page. **(G)** Total intratumoral TINK cell density in MC38 (left) or B16F10 (right) tumors. n = 9-13 (MC38) or 8-10 (B16F10) mice per genotype combined from two (B16F10) or three (MC38) separate experiments. **(H)** Proportion of perforin-expressing (left) or GzmB-expressing (right) TINK cells in mice treated *in vivo* for 6 h with either brefeldin or vehicle control (5% DMSO). n = 7-10 mice per group combined from two separate experiments. **(A-H)** FSFC analyses of day 12-15 MC38 tumors. Bar graphs depict mean ± SEM. Significance was assessed using one-way ANOVA (G) or two-way ANOVA with Tukey's multiple comparisons test (A,B,D,H). *p<0.05; **p<0.01; ***p<0.001; ****p<0.0001.

Accordingly, surface levels of the degranulation marker CD107a were significantly higher on $A20^{ZF7/ZF7}$ Ttex than on $A20^{+/+}$ or $A20^{ZF7/+}$ Ttex following brief *ex vivo* stimulation (**Figure 2.11C-2.11D**). Meanwhile, the fraction of perforin$^+$ Ttex remained similar in brefeldin- versus vehicle-treated $A20^{+/+}$ and $A20^{ZF7/+}$ mice (**Figure 2.11B**), suggesting minimal degranulation by these Ttex. Parallel findings of increased SSC-A, GzmB and GzmC were observed in brefeldin-treated $A20^{ZF7/ZF7}$ Ttex, but not in $A20^{+/+}$ or $A20^{ZF7/+}$ Ttex (**Figure 2.12C**). Of note, minimal GzmA expression was observed in Ttex of any genotype (**Figure 2.12C**). Importantly, while PD-1$^-$ TILs and Tpex both expressed GzmB (**Figure 2.12C**), few perforin$^+$ PD-1$^-$ TILs or Tpex were detected in any genotype even after *in vivo* brefeldin treatment (**Figure 2.11B**), confirming that perforin production is highly restricted to Ttex. Finally, KLRG1$^+$ Ttex at baseline expressed less perforin and more CD107a than KLRG1$^-$ Ttex (**Figure 2.12D**). After *in vivo* brefeldin treatment, perforin levels between KLRG1$^+$ and KLRG1$^-$ $A20^{ZF7/ZF7}$ Ttex became relatively similar (**Figure 2.12E**), suggesting that the less exhausted appearing KLRG1$^+$ Ttex subset was more actively degranulating perforin *in vivo*. Overall, these data highlight an unappreciated defect in Ttex degranulation that can be reversed upon $A20^{ZF7}$ inactivation.

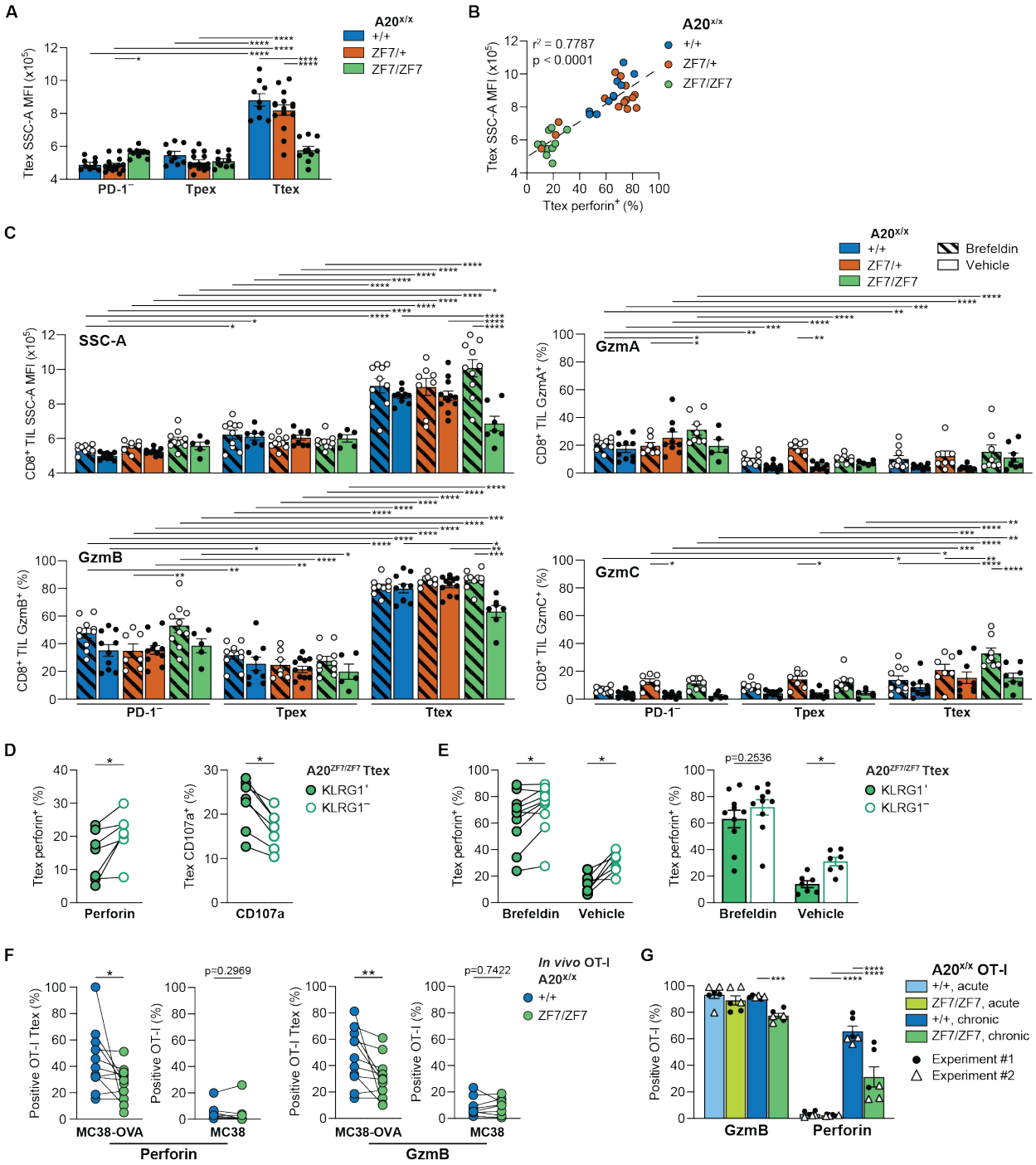

Figure 2.12 A20^{ZF7} suppression of Ttex degranulation depends upon repetitive TCR stimulation.

(A) CD8$^+$ TIL subset SSC-A mean values. n = 9-15 samples per genotype combined from three separate experiments. **(B)** Scatter plot correlating SSC-A mean from (A) with Ttex perforin expression (see Figure 2.9F). Statistics were calculated using simple linear regression (dashed line). **(C)** SSC-A mean (top left) or proportion of GzmA- (top right) versus GzmB- (bottom left) versus GzmC- (bottom right) expressing CD8$^+$ TIL subsets in mice treated *in vivo* for 6 h with either brefeldin or vehicle control (5% DMSO). (Figure caption continued on the next page)

(Figure caption continued from the previous page) n = 5-12 mice per group combined from two separate experiments. **(D)** Paired analysis of perforin (left; related to Figure 2.9F) or CD107a (right; related to Figure 2.11D) expression by KLRG1$^+$ versus KLRG1$^-$ A20$^{ZF7/ZF7}$ Ttex. **(E)** (Left) Paired analysis of perforin expression by KLRG1$^+$ versus KLRG1$^-$ A20$^{ZF7/ZF7}$ Ttex in mice treated for 6 h *in vivo* with either brefeldin or vehicle control, related to Figure 2.11B. (Right) Same data presented in unpaired format. **(F)** Paired analysis of perforin (left) or GzmB (right) expression by OT-I Ttex 7 days following adoptive co-transfer into MC38- versus MC38-OVA-bearing WT mice. **(G)** GzmB and perforin expression by OT-I cells following *in vitro* acute versus chronic/repetitive stimulation. Bar graphs depict mean ± SEM of technical triplicates combined from two separate experiments. Significance was assessed using two-way ANOVA with Bonferroni's multiple comparisons test. **(A-F)** FSFC analyses of day 12-15 MC38 tumors. Bar graphs depict mean ± SEM, with significance assessed using Bonferroni's (E) or Tukey's multiple comparisons test (A,C). Symbol/line pairs represent cells matched from same tumor, with significance assessed using Wilcoxon matched-pairs signed rank test. *p<0.05; **p<0.01; ***p<0.001; ****p<0.0001.

We next aimed to verify that Ttex-derived perforin – rather than perforin produced by another cell subset – drove the A20$^{ZF7/ZF7}$ anti-tumor phenotype. We gated the FSFC data from our *in vivo* brefeldin- versus vehicle-treated mouse experiments on perforin$^+$ cells and discovered that, as expected, almost all were CD45$^+$ leukocytes (**Figure 2.11E**). Among these CD45$^+$perforin$^+$ cells, nearly all were either CD8$^+$ TILs (primarily Ttex) or tumor-infiltrating NK (TINK) cells, regardless of genotype (**Figure 2.11F**). Three key pieces of evidence indicated that TINK cell-derived perforin was not the key driver of anti-tumor immunity in A20$^{ZF7/ZF7}$ mice. First, as discussed, RAG1 deficiency, which ablates CD8$^+$ TILs but not TINK cells, eliminated the anti-tumor phenotype (**Figure 2.5A-2.5B**). Second, we observed significantly diminished TINK cell density in A20$^{ZF7/ZF7}$ mice when compared to A20$^{+/+}$ mice (**Figure 2.11G**), implicating a key role for A20 in supporting TINK cell proliferation, survival or recruitment. Third, A20$^{ZF7/ZF7}$ TINK cells in vehicle-treated mice expressed similarly high levels of perforin and GzmB as A20$^{+/+}$ and A20$^{ZF7/+}$ TINK cells, with no further increase following *in vivo* brefeldin treatment (**Figure 2.11H**), suggesting that A20$^{ZF7/ZF7}$ TINK cells are not robustly degranulating.

Together these findings validate a critical anti-tumor role for $A20^{ZF7/ZF7}$ Ttex-derived perforin, and highlight different roles for A20 in regulating $CD8^+$ TIL versus TINK cell biology.

Cas9-editing of $A20^{ZF7}$ in human CAR-T cells enhances anti-tumor immunity in vivo

Given the potent ability of $A20^{ZF7}$ to regulate anti-tumor immunity, we next tested whether specific ablation of the $A20^{ZF7}$ motif in human CD19 *TRAC*-CAR-T cells would enhance leukemia control in preclinical models. We designed a Cas9 sgRNA targeting a double-stranded break (DSB) at Asp768 in the $A20^{ZF7}$ motif to disrupt the domain via indel frameshift (Supp. Table 6), thereby inactivating the two (of four) most C-terminal zinc coordinating cysteines in the $A20^{ZF7}$ domain that instruct M1 Ub binding.[30] This Cas9-directed edit at Asp768 is near the C-terminus of A20, and is therefore not expected to impact the functionality of the remainder of the A20 protein. We confirmed efficient $A20^{ZF7}$ indel generation (91%), and immunoblotting revealed efficient deletion of A20 in $A20^{KO}$ T cells, while $A20^{ZF7}$ T cells retained A20 protein expression (**Figure 2.14A**). We next injected $A20^{KO}$, $A20^{ZF7}$, or control AAVS1 CD19 CAR-T cells into NALM6-bearing NSG mice and monitored leukemia growth. Mice treated with either $A20^{KO}$ or $A20^{ZF7}$ CAR-T cells potently suppressed NALM6 leukemia growth and demonstrated increased complete response (CR) rates (**Figure 2.13A; Figure 2.14B**) and survival (**Figure 2.13B**) when compared to mice treated with control AAVS1 CAR-T cells. Most recipients of $A20^{KO}$ or $A20^{ZF7}$ CAR-T cells that achieved CR remained leukemia-free for several months without relapse, and furthermore resisted iterative NALM6 rechallenge (**Figure 2.14C**). Thus, as with $A20^{KO}$ CAR-T cells, Cas9-directed abrogation of the $A20^{ZF7}$ domain in CAR-T cells dramatically enhances the anti-tumor efficacy and functional persistence of these cells.

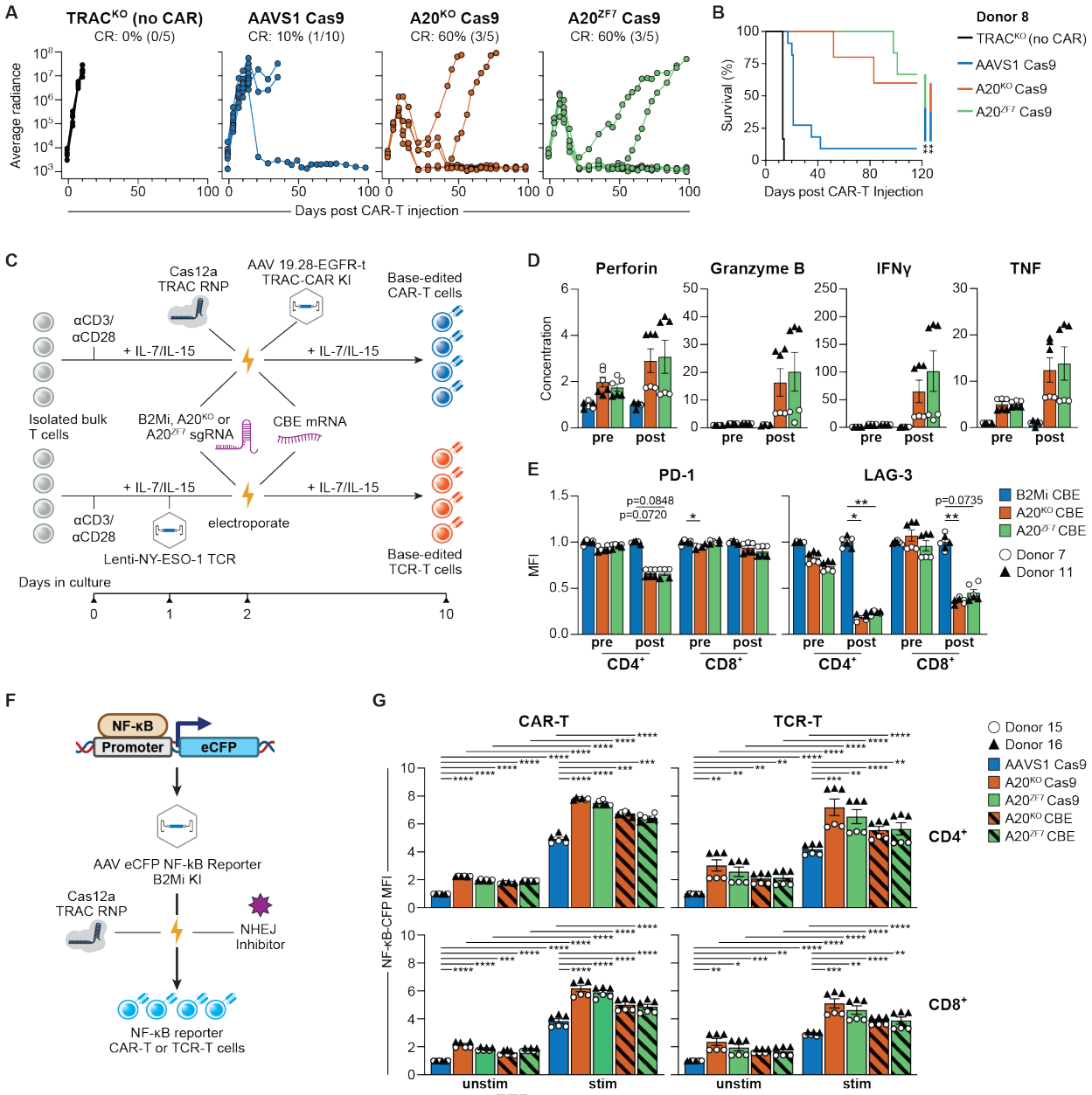

Figure 2.13 Base-editing to inactivate A20^{ZF7} enhances CAR-T cell function *in vitro*. **(A)** Individual NALM6 growth curves of mice treated with Cas9-edited CAR-T cells or with TRAC^{KO} (no CAR) T cells (n = 1 T cell donor, n = 5-10 mice per group). CR = complete response. Leukemia burden was quantified via BLI. Radiance units = photons/s/cm^2/steradian. **(B)** Survival analysis corresponding to (A). Significance was assessed using log-rank test. **(C)** Schematic illustration for the generation of base-edited CD19 *TRAC*-CAR-T (top) or 1G4 TCR-T (bottom) cells. Cas12a RNP carrying *TRAC*-targeting sgRNAs (CAR-T only), cytosine base-editor (CBE)-encoding mRNA, and a CBE sgRNA were introduced into T cells via electroporation. **(D)** Normalized supernatant concentrations (pg/ml) of secreted effector molecules from base-edited CD19 CAR-T cells, as determined by LEGENDplex. CAR-T cells were analyzed before (pre) or after (post) 3 rounds of repetitive stimulation. **(E)** Normalized IR expression by CD4$^+$ and CD8$^+$ CD19 CAR-T cells either before (pre) or after (post) 5 rounds of repetitive stimulation. (Figure caption continued on the next page)

(Figure caption continued from the previous page) **(F)** Schematic illustration for the generation of NF-κB activity reporter CAR-T or TCR-T cells. Cells were electroporated with Cas12a RNP carrying B2Mi-targeting sgRNAs, then transduced with AAV carrying NF-κB reporter construct. For base-edited cells, steps in (C) were concurrently performed. For Cas9-edited cells, Cas9 RNPs with sgRNAs targeting AAVS1, $A20^{KO}$ or $A20^{ZF7}$ were electroporated in lieu of CBE mRNA and associated sgRNAs. **(G)** Normalized NF-kB-CFP MFI of Cas9 or base-edited CD19 CAR-T (left) or 1G4 TCR-T (right) cells before (unstim) or after 12 h stimulation (stim) with antigen-expressing tumor cells (E:T 1:2). **(D,E,G)** Bar graphs depict mean ± SEM of n = 2 donors with n = 3 technical replicates per donor. Each technical replicate was normalized to mean of control (AAVS1 or B2Mi) group for corresponding donor and condition. Significance was assessed using paired t test. *p<0.05; **p<0.01; ***p<0.001; ****p<0.0001.

Base-editing of $A20^{ZF7}$ enhances cytolytic function of human CAR-T cells in vitro

Cas9-based CRISPR editing relies upon DNA DSBs that lead to deletions or frameshifts. By contrast, CRISPR base editors (BEs) generate targeted base pair edits without causing DSB.[89] Hence, BE-directed mutagenesis usually mutates a single amino acid and avoids triggering DNA DSB repair pathways, which altogether confers a more defined and clinically safer approach to genomic engineering. To test the therapeutic potential of this strategy, we used BEs to introduce a targeted $A20^{ZF7}$ domain missense mutation into CAR-T cells. From our ESM1b analysis and large-scale BE screen (**Figure 2.3A**)[16], we nominated a specific amino acid residue within the $A20^{ZF7}$ motif (Cys779), and a corresponding sgRNA targeting a missense mutation (C779Y; Supp. Table 6) predicted to disrupt A20 function and enhance T cell activation (**Figure 2.14D**). Notably, Cys779 represents the third (of four) Zn^{++}-coordinating cysteines in the $A20^{ZF7}$ motif, and is likely important for M1 Ub binding.[9,13,69] For comparison, we also generated base-edited $A20^{KO}$ CAR-T cells using an sgRNA that introduces a premature stop codon in exon 2 of the A20 gene (R90*; Supp. Table 6), and confirmed elimination of the A20 protein by immunoblot (**Figure 2.14A**). Control T cells from the same donors were edited with an sgRNA targeting an intronic sequence of the *B2M* gene encoding beta-2 microglobulin (β2m; Supp. Table 6). This intronic mutation (hereafter referred to as B2Mi) does not disrupt β2m surface protein expression

(**Figure 2.14E**). Next-generation sequencing analysis of T cells collected 7 days after editing confirmed that both the $A20^{KO}$ and $A20^{ZF7}$ sgRNAs edited A20 with 90% efficiency, generating the expected R90* or C779Y mutations, while the B2Mi sgRNA edited with 97% efficiency.

We next engineered CD19 CAR-T cells that were base-edited with either $A20^{KO}$, $A20^{ZF7}$ or control B2Mi sgRNAs. We introduced Cas12a RNP carrying *TRAC*-targeting sgRNAs, cytosine base-editor (CBE)-encoding mRNA, and a CBE sgRNA targeting either $A20^{KO}$, $A20^{ZF7}$ or B2Mi into T cells via electroporation (**Figure 2.13C**). As CBE is coupled to a nicking Cas9 (nCas9) for targeting, we utilized Cas12a-mediated *TRAC*-CAR knock-in here to prevent guide swapping between the two Cas proteins.[90] We then tested our base-edited CD19 CAR-T cells using our *in vitro* repetitive stimulation assay. Base-edited CAR-T cells were repeatedly stimulated with fresh $CD19^{+}$ tumor cells, then evaluated for expression of activation and exhaustion markers, production of cytokines and cytotoxic proteins, and tumor cell killing capacity. Repetitively stimulated $A20^{KO}$ and $A20^{ZF7}$ CAR-T cells exhibited enhanced proliferation when compared to control B2Mi CAR-T cells (**Figure 2.14F**). Remarkably, $A20^{KO}$ and $A20^{ZF7}$ base-edited CAR-T cells also maintained robust tumoricidal capacity compared to control B2Mi CAR-T cells after three rounds of tumor stimulation (**Figure 2.14G**). Furthermore, compared to control B2Mi CAR-T cells, base-edited $A20^{KO}$ and $A20^{ZF7}$ CAR-T cells produced more effector cytokines (IFNγ, TNF) and secreted substantially more cytotoxic granule proteins (perforin, GzmB) after repetitive stimulation (**Figure 2.13D**), consistent with our findings of increased secretion by Cas9-edited $A20^{KO}$ TCR-T cells (**Figure 2.15D**) and increased degranulation by $A20^{ZF7/ZF7}$ Ttex (**Figure 2.11**). Lastly, repetitively stimulated $A20^{KO}$ and $A20^{ZF7}$ CAR-T cells expressed lower levels of exhaustion markers (PD-1 and LAG-3; **Figure 2.13E**)

and higher levels of activation markers (CD25, CD137, CD69 and CD154) (**Figure 2.14H**). Importantly, by all metrics, $A20^{KO}$ and $A20^{ZF7}$ CAR-T cells performed similarly.

We next determined whether these CRISPR editing approaches enhanced NF-κB activity, a common readout for A20 dysfunction.[66,69] To this end, we generated AAVS1 and Cas9- or CBE-directed $A20^{KO}$ and $A20^{ZF7}$ TCR-T or CAR-T cells, and concurrently transduced them with a construct encoding NF-κB-dependent cyan fluorescent protein (CFP) expression, knocked into the B2Mi locus to ensure consistent regulation of CFP expression across cells (**Figure 2.13F**). Notably, both Cas9 and CBE $A20^{KO}$ and $A20^{ZF7}$ CAR-T and TCR-T cells exhibited higher basal NF-κB activity than control AAVS1 cells even prior to stimulation (**Figure 2.13G**). Following stimulation with antigen-expressing tumor cells, all groups expectedly increased their NF-κB activity, but both Cas9- and base-edited $A20^{KO}$ and $A20^{ZF7}$ CAR-T and TCR-T cells demonstrated substantially higher activity than AAVS1 (**Figure 2.13G**). Thus, functional ablation of A20 and augmentation of NF-κB activity within ACTs can be easily achieved using Cas9- or CBE-directed disruption of the $A20^{ZF7}$ motif.

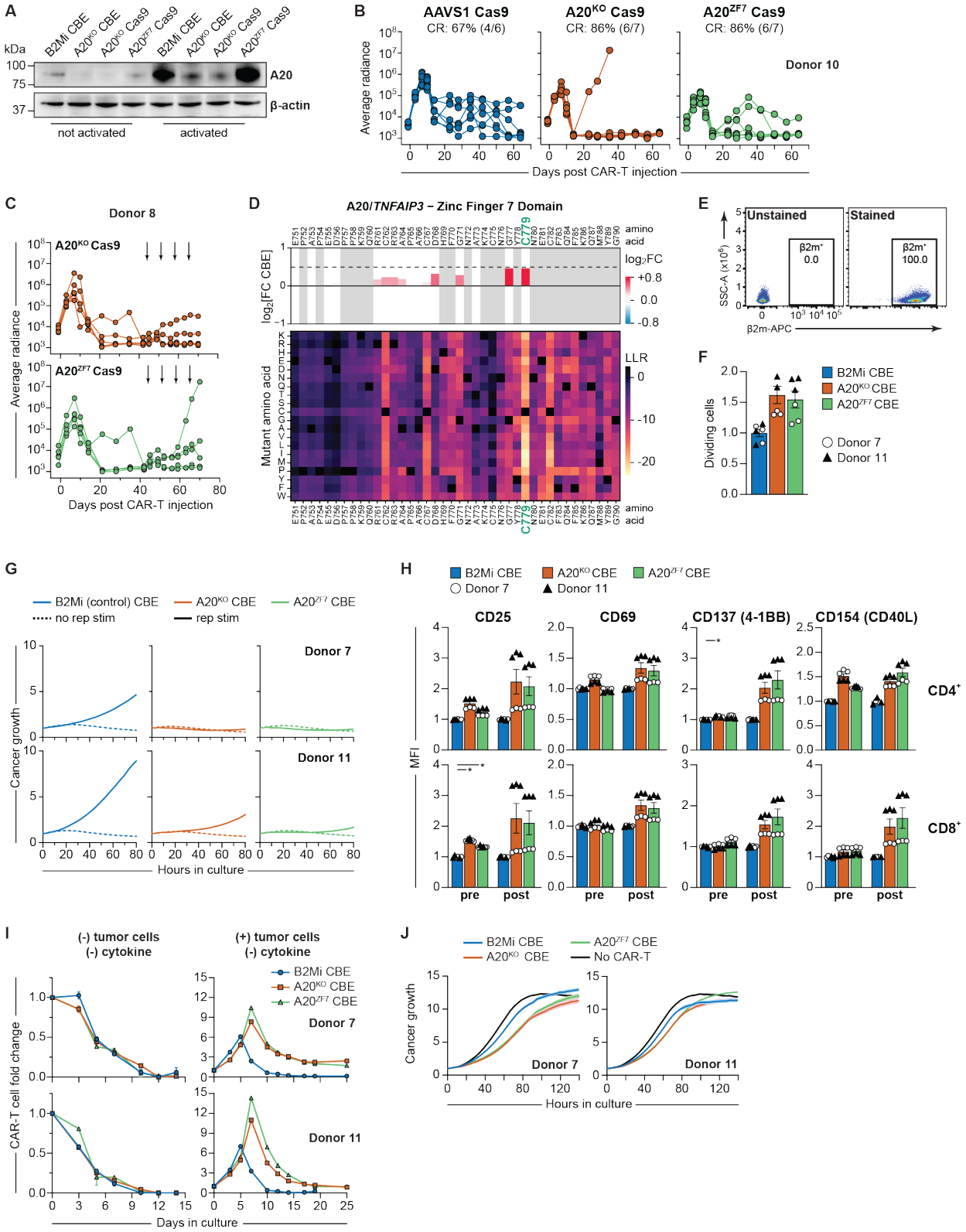

Figure 2.14 Cas9- or BE-directed A20^{ZF7} inactivation augments CAR-T cell anti-tumor activity without safety concerns.

(Figure caption continued on the next page)

(Figure caption continued from the previous page) **(A)** Immunoblot of A20 expression by Cas9- or base-edited (CBE) human T cells that were either not activated, or activated with anti-CD3/CD28 for 24 hours. n = 1 donor. **(B)** Individual NALM6 growth curves of mice treated with Cas9-edited CAR-T cells or with $TRAC^{KO}$ (no CAR) T cells (n = 1 T cell donor different from Figure 2.13A, n = 6-7 mice per group). CR = complete response. Leukemia burden was quantified via BLI. Radiance units = photons/s/cm^2/steradian. **(C)** Individual NALM6 growth curves of mice that controlled initial challenge (Figure 2.13A) and underwent iterative rechallenge (black arrows). **(D)** CBE screen (top) and ESM1b heatmap (bottom) from Figure 2.3A, zoomed in on $A20^{ZF7}$ motif. sgRNA target (Cys779) highlighted in green. **(E)** Representative dot plots depicting β2m expression on B2Mi CAR-T cells 36 hours after base-editing. Inset = percentage of $\beta2m^+$ cells. **(F)** Normalized dividing cells (CellTrace $Violet^{lo}$), as determined via proliferation assay of CAR-T cells after 72 h of stimulation. **(G)** Normalized growth curves of A375-CD19 cells. CAR-T cells either without prior repetitive stimulation (no rep stim) or after 3 rounds of repetitive stimulation (rep stim) were co-cultured with A375-CD19 cells at an E:T ratio of 1:1 (mean ± SEM of n = 3 technical replicates; n = 2 donors). **(H)** Normalized expression of activation markers by $CD4^+$ (top) and $CD8^+$ (bottom) CAR-T cells before (pre) and after (post) 3 rounds of tumor stimulation. **(I)** Fold change of base-edited CD19 CAR-T cells cultured without cytokine either in the absence (left) or presence (right) of A375-CD19 target cells (E:T ratio 1:1). **(J)** Normalized growth curves of CD19-negative A375 melanoma cells co-cultured with CD19 CAR-T cells (E:T 1:1), or cultured without CAR-T cells. **(F,H)** Bar graphs depict mean ± SEM of n = 2 donors with n = 3 technical replicates per donor. Each technical replicate was normalized to mean of B2Mi group for corresponding donor and condition. Significance was assessed using paired t test. **(I,J)** All curves show mean ± SEM of n = 3 technical replicates from n = 2 T cell donors. *$p<0.05$.

We next tested whether A20 ablation via base-editing enables human CAR-T cells to grow in a cytokine- or antigen-independent fashion, which could represent a safety challenge for ACT applications. First, we evaluated the growth of $A20^{KO}$ and $A20^{ZF7}$ CAR-T cells after the withdrawal of cytokines, where we observed consistent decreases in cell numbers and viability of both $A20^{KO}$ and $A20^{ZF7}$ CAR-T cells, similar to control B2Mi CAR-T cells (**Figure 2.14I**). Further, the numbers of $A20^{KO}$ and $A20^{ZF7}$ CAR-T cells contracted as expected after initial exposure to tumor cells without cytokines (**Figure 2.14I**). We also assessed the level of dependence on antigen of $A20^{KO}$ and $A20^{ZF7}$ CAR-T cells for tumor cell killing. Here, we exposed all CAR-T cell conditions to CD19-negative tumor cells and assessed their ability to eradicate tumor cells over several days. We observed a small degree of allogenic killing, which was similar across all conditions (**Figure 2.14J**). Therefore, targeting A20 does not confer

cytokine-independent growth or antigen-independent killing, suggesting A20-targeted CAR-T cells may be safe for clinical use.

Base-editing of A20^{ZF7} enhances human CAR-T cell efficacy in vivo

To test the ability of base-edited A20-targeted CAR-T cells to suppress tumor growth *in vivo*, we treated NALM6-engrafted mice with either base-edited A20^{KO}, A20^{ZF7}, or control B2Mi CD19 CAR-T cells and serially measured growth of the luminescent NALM6 tumors via BLI. Mice treated with A20^{KO} or A20^{ZF7} base-edited CAR-T cells exhibited superior tumor control, CR rates and survival when compared to mice treated with B2Mi CAR-T cells (**Figure 2.15A-2.15B; Figure 2.16A-2.16B**). Importantly, mice that controlled their initial leukemia challenge appeared grossly normal based upon visual inspection and body weight (**Figure 2.16C**). To understand why A20^{KO} and A20^{ZF7} engineered CAR-T cells suppress leukemia growth better than control B2Mi CAR-T cells, we evaluated bone marrow samples from tumor bearing mice 14 days after CAR-T cell adoptive transfer by flow cytometry. At this early time point, leukemia burden remained relatively even across treatment groups. Our findings showed a trend toward higher numbers of CAR-T cells in the bone marrow of mice treated with A20^{KO} or A20^{ZF7} CAR-T cells when compared to those treated with control B2Mi CAR-T cells (**Figure 2.16D**). Notably, editing of A20 did not substantially change the distribution of memory phenotypes of the isolated CAR-T cells (**Figure 2.16E**). Finally, the frequency of CAR-T cells co-expressing 2 or more IRs was markedly lower in A20^{KO} (24-30%) and A20^{ZF7} (34-46%) CAR-T cells when compared with B2Mi control (51-65%) (**Figure 2.15C**), consistent with our findings in A20$^{ZF7/ZF7}$ Ttex (**Figure 2.7**). These data highlight that base-editing of A20^{ZF7} can lead to remarkable improvements *in vivo* using an already optimized best-in-class CAR-T cell therapy, accompanied by reduced exhaustion, without any clear safety risk.

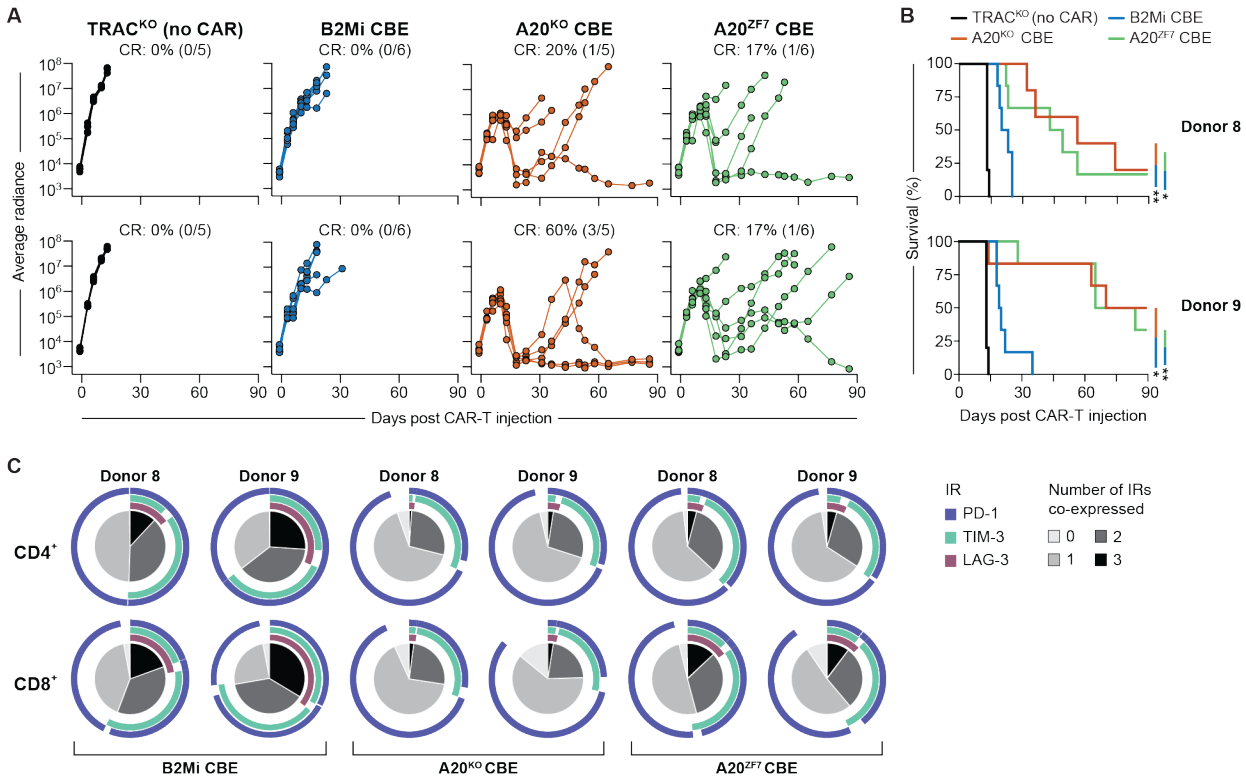

Figure 2.15 Base-editing to inactivate A20^{ZF7} enhances CAR-T cell function *in vitro* and *in vivo*.

(A) Individual NALM6 growth curves of mice treated with base-edited (CBE) CAR-T cells, or with TRAC^{KO} (no CAR) T cells (n = 2 T cell donors, n = 5-6 mice per group per donor). CR = complete response. Leukemia burden was quantified via BLI. Radiance units = photons/s/cm^2/steradian. **(B)** Survival analysis corresponding to (A). Survival significance was assessed using log-rank test. **(C)** SPICE analyses of IR co-expression on base-edited CD4$^+$ and CD8$^+$ CAR-T cells isolated from bone marrow of NALM6-bearing mice 14 days after CAR-T cell injection, as determined by flow cytometry. Plots depict mean of n = 3 mice per group per n = 2 donors. *p<0.05; **p<0.01.

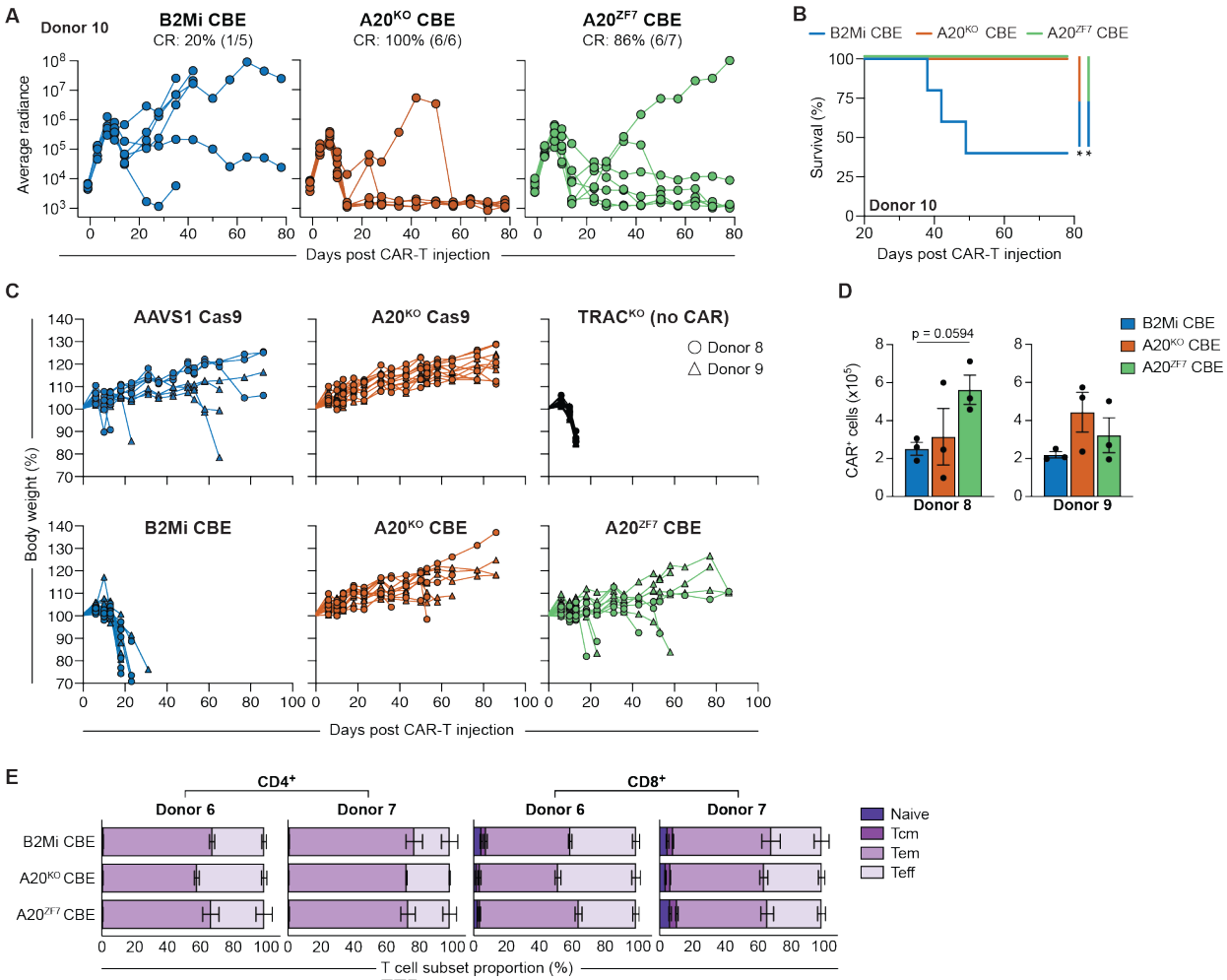

Figure 2.16 BE-directed A20^{ZF7} inactivation augments CAR-T cell anti-tumor activity. **(A)** Individual NALM6 growth curves of mice treated with Cas9-edited CAR-T cells or with TRAC^{KO} (no CAR) T cells (n = 1 T cell donor, n = 5-7 mice per group). Different donor than used in Figure 2.15A. Leukemia burden was quantified via BLI. Radiance units = photons/s/cm^2/steradian. **(B)** Survival analysis corresponding to (A). Survival significance was assessed using log-rank test. **(C)** Total body weight of NALM6-bearing mice after receiving Cas9- or base-edited CAR-T cell injection, expressed as percent change over baseline weight (measured on day -1 prior to CAR-T injection). Each graph depicts individual weight curves of n = 5-9 mice per donor per group (n = 2 T cell donors). **(D)** Absolute numbers of CAR-T cells harvested from the bone marrow of NALM6-bearing mice 14 days after CAR-T cell injection, as determined by flow cytometry (mean ± SEM, n = 2 T cell donors, n = 3 mice per group per donor). Significance was assessed using one-way ANOVA with Dunnett's T3 multiple comparisons test. **(E)** Differentiation status of CD4$^+$ or CD8$^+$ base-edited CAR-T from (e). Naive = CD45RA$^+$CD62L$^+$; central memory (Tcm) = CD45RA$^-$CD62L$^+$; effector memory (Tem) = CD45RA$^-$CD62L$^-$; effector (Teff) = CD45RA$^+$CD62L$^-$ (mean ± SEM, n=2 T cell donors, n = 3 mice per group per donor). **(D,E)** Bar graphs depict mean ± SEM. *p<0.05.

Discussion

In this study, we filtered the entire protein-coding genome through a CRISPR knockout screen, followed by a base-editing mutagenesis screen, a protein large language model, and transgenic knock-in mice to pinpoint a single protein domain — $A20^{ZF7}$ — as a critical negative regulator of $CD8^+$ TIL function. This precise molecular lever operated both in murine and human T cells, in liquid and solid tumors, and in immunodeficient and immunocompetent mice. We then base-edited a single $A20^{ZF7}$ missense mutation at high editing efficiency that robustly enhanced CAR-T cell anti-tumor activity. Our study sets a new standard for engineering functionally enhanced CAR-T cell clinical products using base-editing. BE-directed gene ablation avoids Cas9-directed DNA double-stranded breaks and their potential associated chromosomal rearrangements.[89,91] We take this approach one step further by using base-editing to introduce a strategic missense mutation rather than total gene ablation. For multifunctional proteins like A20, this approach could prove superior to complete ablation, with fewer undesirable side effects. Recent large-scale base-editing mutagenesis screens have begun to pinpoint key amino acid residues that impact T cell functions *in vitro*.[16,26] We have now translated this approach to CAR-T cell enhancement *in vivo* by targeting $A20^{ZF7}$. BE-guided gene ablation can also be multiplexed[92], thus setting the stage for combining missense mutations to develop safer and more efficacious next-generation ACTs. Indeed, multiplexed editing within A20 itself might lead to further enhancements, as we and others have described synergy between the $A20^{ZF4}$ and $A20^{ZF7}$ motifs that prevents spontaneous inflammation.[30,31]

Interestingly, the aforementioned large-scale BE screens to identify amino acids relevant to T cell function converged on mutations found in hereditary autoimmune syndromes.[16,26] Likewise, inherited A20 mutations cause haploinsufficiency of A20 (HA20), a syndrome with

autoimmune manifestations.[93] Also of note, T cell lymphoma oncogenic mutations intentionally expressed in CAR-T cells can boost their efficacy, particularly those that augment NF-κB signaling[7], and somatic A20 mutations have been described in B and T cell lymphomas.[94,95] Altogether, these findings highlight that the optimal enhancement of ACTs may already be written in the genetics of existing pathophysiologic processes, including those tied to A20 dysfunction. Importantly, our studies using $A20^{KO}$ or $A20^{ZF7}$ CAR-T cells showed no evidence of dysregulated proliferation *in vitro* or *in vivo*. While continued safety monitoring will be paramount as A20-deficient ACTs move forward toward clinical use, preliminarily we find no safety concerns.

Our prior genome-scale CRISPR screens identified a role for A20 in restraining proliferation of acutely stimulated human T cells.[4,5] We herein leveraged this platform to reveal that A20 potently orchestrates T cell dysfunction in the setting of chronic antigen exposure. Our data extend the findings of previous genome-scale human T cell exhaustion screens[24,25] by incorporating substantially longer repetitive tumor stimulation. In our screen, A20 became progressively enriched with increasing rounds of stimulation, suggesting that A20's role is potentiated during later stages of exhaustion. These results align with multiomics analyses wherein Ttex differentiation correlated with increased A20/*Tnfaip3* chromatin accessibility and decreased NF-κB transcriptional signatures.[96,97] The mechanism by which A20 promotes terminal exhaustion has yet to be elucidated, though our findings suggest that A20 supports TOX expression. Indeed, the predominance of $KLRG1^{+}$ $A20^{ZF7/ZF7}$ Ttex mirrors the skewing of chronically stimulated TOX-deficient $CD8^{+}$ T cells toward $KLRG1^{+}$ cells.[77,79] A20 might also promote exhaustion via restraint of NF-κB signaling. In acutely activated T cells, A20 disrupts NF-κB activity following recruitment to the CARD11-BCL10-MALT1 (CBM) signalosome[32,33],

possibly via the $A20^{ZF7}$ motif.[35] Acutely activated CAR-T cells also recruit A20 to the CAR endodomain.[98] Repeated TCR or CAR stimulation might similarly engage A20 to repress NF-κB and induce TOX. However, unlike $A20^{ZF7}$ CAR-T cells and $A20^{ZF7/ZF7}$ Ttex, TOX-deficient $CD8^+$ TILs remain dysfunctional in the TME.[78] Thus, A20 likely also regulates TOX-independent pathways to implement exhaustion.

We reveal two layers of anti-tumor effector mechanisms unlocked by targeting $A20^{ZF7}$ in T cells and CAR-T cells. The first layer involves enhanced production of IFNγ and TNF, consistent with prior studies of $A20^{KO}$ $CD8^+$ TILs.[38–40] We extend these studies by directly interrogating the role of IFNγ and TNF in anti-tumor immunity, and by showing that inactivation of a single $A20^{ZF7}$ allele promotes cytokine-dependent tumor suppression. However, $A20^{ZF7/ZF7}$ mice suppressed tumor growth even in the absence of these cytokines, highlighting a more potent second layer — the perforin-granzyme axis — accessible only below a certain threshold of $A20^{ZF7}$ activity. While our understanding of Tex biology to date has concentrated upon epigenetic and transcriptional regulation of effector programs, we discover an unappreciated posttranscriptional regulatory step in Ttex at the level of perforin degranulation. Indeed, Ttex consistently express perforin and granzymes[21–23], yet their native ability to degranulate has not been studied. We used *in vivo* brefeldin treatment to demonstrate that $A20^{ZF7/ZF7}$ Ttex rapidly degranulated perforin, while $A20^{+/+}$ and $A20^{ZF7/+}$ Ttex did not. Thus, assays that solely measure Ttex perforin or granzyme content may not accurately reflect their true cytotoxic potential. Moving forward, the use of *in vivo* brefeldin treatment could help discriminate the functional state of Ttex. While the pathways that connect TCR engagement to degranulation remain incompletely understood[99], genome-scale CRISPR screens have begun to discover mediators in acutely activated T cells.[100] Similar screens in chronically stimulated T cells might find

additional mediators of Ttex degranulation beyond A20. Importantly, the dependence on cytokines versus perforin for anti-tumor immunity may vary based on the tumor model or immunotherapy used.[41–48] Our study emphasizes the importance of finding targets such as A20^{ZF7} that can enhance TIL and CAR-T cell activity in multiple ways.

References

1. Brentjens, R. J. *et al.* Safety and persistence of adoptively transferred autologous CD19-targeted T cells in patients with relapsed or chemotherapy refractory B-cell leukemias. *Blood* **118**, 4817–4828 (2011).

2. Sterner, R. C. & Sterner, R. M. CAR-T cell therapy: current limitations and potential strategies. *Blood Cancer Journal* vol. 11 Preprint at https://doi.org/10.1038/s41408-021-00459-7 (2021).

3. Jiang, Y., Chen, M., Nie, H. & Yuan, Y. PD-1 and PD-L1 in cancer immunotherapy: clinical implications and future considerations. *Human Vaccines and Immunotherapeutics* vol. 15 1111–1122 Preprint at https://doi.org/10.1080/21645515.2019.1571892 (2019).

4. Shifrut, E. *et al.* Genome-wide CRISPR Screens in Primary Human T Cells Reveal Key Regulators of Immune Function. *Cell* **175**, 1958-1971.e15 (2018).

5. Carnevale, J. *et al.* RASA2 ablation in T cells boosts antigen sensitivity and long-term function. *Nature* **609**, 174–182 (2022).

6. Wei, J. *et al.* PD-1 silencing impairs the anti-tumor function of chimeric antigen receptor modified T cells by inhibiting proliferation activity. *J. Immunother. Cancer* **7**, 209 (2019).

7. Garcia, J. *et al.* Naturally occurring T cell mutations enhance engineered T cell therapies. *Nature* **626**, 626–634 (2024).

8. Brandes, N., Goldman, G., Wang, C. H., Ye, C. J. & Ntranos, V. Genome-wide prediction of disease variant effects with a deep protein language model. *Nat. Genet.* **55**, 1512–1522 (2023).

9. Ma, A. & Malynn, B. A. A20: linking a complex regulator of ubiquitylation to immunity and human disease. *Nat Rev Immunol* **12**, 774–785 (2012).

10. Combes, A. J. *et al.* Discovering dominant tumor immune archetypes in a pan-cancer census. *Cell* **185**, 184-203.e19 (2022).

11. Daniels, M. A., Luera, D. & Teixeiro, E. NFκB signaling in T cell memory. *Front. Immunol.* **14**, (2023).

12. Das, T., Chen, Z., Hendriks, R. W. & Kool, M. A20/Tumor Necrosis Factor α-Induced Protein 3 in Immune Cells Controls Development of Autoinflammation and Autoimmunity: Lessons from Mouse Models. *Front. Immunol.* **9**, (2018).

13. Tokunaga, F. *et al.* Specific recognition of linear polyubiquitin by A20 zinc finger 7 is involved in NF-κB regulation. *EMBO J* **31**, 3856–3870 (2012).

14. Jumper, J. *et al.* Highly accurate protein structure prediction with AlphaFold. *Nature* **596**, 583–589 (2021).

15. Gaudelli, N. M. *et al.* Programmable base editing of A•T to G•C in genomic DNA without DNA cleavage. *Nature* **551**, 464–471 (2017).

16. Schmidt, R. *et al.* Base-editing mutagenesis maps alleles to tune human T cell functions. *Nature* **625**, 805–812 (2024).

17. Eyquem, J. *et al.* Targeting a CAR to the TRAC locus with CRISPR/Cas9 enhances tumour rejection. *Nature* **543**, 113–117 (2017).

18. Ting, P. Y. *et al.* Guide Swap enables genome-scale pooled CRISPR–Cas9 screening in human primary cells. *Nat. Methods* **15**, 941–946 (2018).

19. Li, W. *et al.* MAGeCK enables robust identification of essential genes from genome-scale CRISPR/Cas9 knockout screens. *Genome Biol.* **15**, 554 (2014).

20. Baessler, A. & Vignali, D. A. A. T Cell Exhaustion. *Annu. Rev. Immunol.* **42**, 179–206 (2024).

21. Im, S. J. *et al.* Defining CD8+ T cells that provide the proliferative burst after PD-1 therapy. *Nature* **537**, 417–421 (2016).

22. Siddiqui, I. *et al.* Intratumoral Tcf1+PD-1+CD8+ T cells with stem-like properties promote tumor control in response to vaccination and checkpoint blockade immunotherapy. *Immunity* **50**, 195-211.e110 (2019).

23. Miller, B. C. *et al.* Subsets of exhausted CD8+ T cells differentially mediate tumor control and respond to checkpoint blockade. *Nat Immunol* **20**, 326–336 (2019).

24. Wang, D. *et al.* CRISPR Screening of CAR T Cells and Cancer Stem Cells Reveals Critical Dependencies for Cell-Based Therapies. *Cancer Discov* **11**, 1192–1211 (2021).

25. Freitas, K. A. *et al.* Enhanced T cell effector activity by targeting the Mediator kinase module. *Science (1979).* **378, eabn5647**, (2022).

26. Walsh, Z. H. *et al. Mapping Variant Effects on Anti-Tumor Hallmarks of Primary Human T Cells with Base-Editing Screens*. (Nat Biotechnol, 2024). doi:10.1038/s41587-024-02235-x.

27. Malynn, B. A. & Ma, A. A20: A multifunctional tool for regulating immunity and preventing disease. *Cell Immunol* **340**, 103914 (2019).

28. Lee, E. G. *et al.* Failure to regulate TNF-induced NF-kappaB and cell death responses in A20-deficient mice. *Science (1979).* **289**, 2350–2354 (2000).

29. Lu, T. T. *et al.* Dimerization and ubiquitin mediated recruitment of A20, a complex deubiquitinating enzyme. *Immunity* **38**, 896–905 (2013).

30. Razani, B. *et al.* Non-catalytic ubiquitin binding by A20 prevents psoriatic arthritis-like disease and inflammation. *Nat Immunol* **21**, 422–433 (2020).

31. Martens, A. *et al.* Two distinct ubiquitin-binding motifs in A20 mediate its anti-inflammatory and cell-protective activities. *Nat Immunol* **21**, 381–387 (2020).

32. Coornaert, B. *et al.* T cell antigen receptor stimulation induces MALT1 paracaspase-mediated cleavage of the NF-kappaB inhibitor A20. *Nat Immunol* **9**, 263–271 (2008).

33. Düwel, M. *et al.* A20 negatively regulates T cell receptor signaling to NF-kappaB by cleaving Malt1 ubiquitin chains. *J Immunol* **182**, 7718–7728 (2009).

34. Onizawa, M. *et al.* The ubiquitin-modifying enzyme A20 restricts ubiquitination of the kinase RIPK3 and protects cells from necroptosis. *Nat Immunol* **16**, 618–627 (2015).

35. Dabbah-Krancher, G. *et al.* A20 intrinsically influences human effector T-cell survival and function by regulating both NF-κB and JNK signaling. *Eur J Immunol* **54**, (2024).

36. Just, S. *et al.* A20 Curtails Primary but Augments Secondary CD8+ T Cell Responses in Intracellular Bacterial Infection. *Sci Rep* **6**, 39796 (2016).

37. LaFleur, M. W. *et al.* A STUB1-CHIC2 complex inhibits CD8+ T cells to restrain tumor immunity. *Nat Immunol* **26**, 1476–1487 (2025).

38. Giordano, M. *et al.* The tumor necrosis factor alpha-induced protein 3 (TNFAIP3, A20) imposes a brake on antitumor activity of CD8 T cells. *Proc Natl Acad Sci U S A* **111**, 11115–11120 (2014).

39. Mukohara, F. *et al.* Somatic mutations in tumor-infiltrating lymphocytes impact on antitumor immunity. *Proc Natl Acad Sci U S A* **121**, (2024).

40. Luo, C. *et al. Integrated Computational Analysis Identifies Therapeutic Targets with Dual Action in Cancer Cells and T Cells*. (Immunity, 2025). doi:10.1016/j.immuni.2025.02.007.

41. van den Broek, M. E. *et al.* Decreased tumor surveillance in perforin-deficient mice. *J Exp Med* **184**, 1781–1790 (1996).

42. Prévost-Blondel, A., Neuenhahn, M., Rawiel, M. & Pircher, H. Differential requirement of perforin and IFN-gamma in CD8 T cell-mediated immune responses against B16. F10 melanoma cells expressing a viral antigen. *Eur J Immunol* **30**, 2507–2515 (2000).

43. Street, S. E., Cretney, E. & Smyth, M. J. Perforin and interferon-gamma activities independently control tumor initiation, growth, and metastasis. *Blood* **97**, 192–197 (2001).

44. Poehlein, C. H. *et al.* TNF plays an essential role in tumor regression after adoptive transfer of perforin/IFN-gamma double knockout effector T cells. *J Immunol* **170**, 2004–2013 (2003).

45. Cao, X. *et al.* Granzyme B and perforin are important for regulatory T cell-mediated suppression of tumor clearance. *Immunity* **27**, 635–646 (2007).

46. Waldner, M. J. *et al.* Perforin deficiency attenuates inflammation and tumor growth in colitis-associated cancer. *Inflamm Bowel Dis* **16**, 559–567 (2010).

47. Juneja, V. R. *et al.* PD-L1 on tumor cells is sufficient for immune evasion in immunogenic tumors and inhibits CD8 T cell cytotoxicity. *J Exp Med* **214**, 895–904 (2017).

48. Kearney, C. J. *et al.* Tumor immune evasion arises through loss of TNF sensitivity. *Sci Immunol* **3**, (2018).

49. Blaeschke, F. *et al.* Modular pooled discovery of synthetic knockin sequences to program durable cell therapies. *Cell* **186, .e4233**, 4216–4234 (2023).

50. Doench, J. G. *et al.* Optimized sgRNA design to maximize activity and minimize off-target effects of CRISPR-Cas9. *Nat Biotechnol* **34**, 184–191 (2016).

51. Lv, J. *et al.* Disruption of CISH promotes the antitumor activity of human T cells and decreases PD-1 expression levels. *Mol Ther Oncolytics* **28**, 46–58 (2023).

52. Prinzing, B. *et al.* Deleting DNMT3A in CAR T cells prevents exhaustion and enhances antitumor activity. *Sci Transl Med* **13, eabh0272**, (2021).

53. Gurusamy, D. *et al.* Multi-phenotype CRISPR-Cas9 Screen Identifies p38 Kinase as a Target for Adoptive Immunotherapies. *Cancer Cell* **37**, 818-833.e819 (2020).

54. Liao, X. *et al.* The CUL5 E3 ligase complex negatively regulates central signaling pathways in CD8+ T cells. *Nat Commun* **15**, 603 (2024).

55. Belk, J. A. *et al.* Genome-wide CRISPR screens of T cell exhaustion identify chromatin remodeling factors that limit T cell persistence. *Cancer Cell* **40**, 768-786.e767 (2022).

56. Tavares, R. M. *et al.* The ubiquitin modifying enzyme A20 restricts B cell survival and prevents autoimmunity. *Immunity* **33**, 181–191 (2010).

57. Aki, A., Nagasaki, M., Malynn, B. A., Ma, A. & Kagari, T. Hypomorphic A20 expression confers susceptibility to psoriasis. *PLoS One* **12**, (2017).

58. Hammer, G. E. *et al.* Expression of A20 by dendritic cells preserves immune homeostasis and prevents colitis and spondyloarthritis. *Nat Immunol* **12**, 1184–1193 (2011).

59. Vande Walle, L. *et al.* Negative regulation of the NLRP3 inflammasome by A20 protects against arthritis. *Nature* **512**, 69–73 (2014).

60. Duong, B. H. *et al.* A20 restricts ubiquitination of pro-interleukin-1β protein complexes and suppresses NLRP3 inflammasome activity. *Immunity* **42**, 55–67 (2015).

61. Komander, D. & Barford, D. Structure of the A20 OTU domain and mechanistic insights into deubiquitination. *Biochem J* **409**, 77–85 (2008).

62. Boone, D. L. *et al.* The ubiquitin-modifying enzyme A20 is required for termination of Toll-like receptor responses. *Nat Immunol* **5**, 1052–1060 (2004).

63. Wertz, I. E. *et al.* De-ubiquitination and ubiquitin ligase domains of A20 downregulate NF-kappaB signalling. *Nature* **430**, 694–699 (2004).

64. Bosanac, I. *et al.* Ubiquitin binding to A20 ZnF4 is required for modulation of NF-κB signaling. *Mol Cell* **40**, 548–557 (2010).

65. Shembade, N., Ma, A. & Harhaj, E. W. Inhibition of NF-kappaB signaling by A20 through disruption of ubiquitin enzyme complexes. *Science (1979).* **327**, 1135–1139 (2010).

66. Skaug, B. *et al.* Direct, noncatalytic mechanism of IKK inhibition by A20. *Mol Cell* **44**, 559–571 (2011).

67. Wertz, I. E. *et al.* Phosphorylation and linear ubiquitin direct A20 inhibition of inflammation. *Nature* **528**, 370–375 (2015).

68. Rives, A. *et al.* Biological structure and function emerge from scaling unsupervised learning to 250 million protein sequences. *Proc Natl Acad Sci U S A* **118**, (2021).

69. Verhelst, K. *et al.* A20 inhibits LUBAC-mediated NF-κB activation by binding linear polyubiquitin chains via its zinc finger 7. *EMBO J* **31**, 3845–3855 (2012).

70. Hoft, D. F., Lynch, R. G. & Kirchhoff, L. V. Kinetic analysis of antigen-specific immune responses in resistant and susceptible mice during infection with Trypanosoma cruzi. *J Immunol* **151**, 7038–7047 (1993).

71. Labanieh, L. & Mackall, C. L. CAR immune cells: design principles, resistance and the next generation. *Nature* **614**, 635–648 (2023).

72. Jin, Y. *et al.* Different syngeneic tumors show distinctive intrinsic tumor-immunity and mechanisms of actions (MOA) of anti-PD-1 treatment. *Sci Rep* **12**, 3278 (2022).

73. Lewis, K. E. *et al.* Interleukin-21 combined with PD-1 or CTLA-4 blockade enhances antitumor immunity in mouse tumor models. *Oncoimmunology* **7**, (2017).

74. Vignali, P. D. A. *et al.* Hypoxia drives CD39-dependent suppressor function in exhausted T cells to limit antitumor immunity. *Nat Immunol* **24**, 267–279 (2023).

75. LaFleur, M. W. *et al.* PTPN2 regulates the generation of exhausted CD8 T cell subpopulations and restrains tumor immunity. *Nat Immunol* **20**, 1335–1347 (2019).

76. Tillé, L. *et al.* Activation of the transcription factor NFAT5 in the tumor microenvironment enforces CD8+ T cell exhaustion. *Nat Immunol* **24**, 1645–1653 (2023).

77. Khan, O. *et al.* TOX transcriptionally and epigenetically programs CD8+ T cell exhaustion. *Nature* **571**, 211–218 (2019).

78. Scott, A. C. *et al.* TOX is a critical regulator of tumour-specific T cell differentiation. *Nature* **571**, 270–274 (2019).

79. Alfei, F. *et al.* TOX reinforces the phenotype and longevity of exhausted T cells in chronic viral infection. *Nature* **571**, 265–269 (2019).

80. Chen, Z. *et al.* TCF-1-Centered Transcriptional Network Drives an Effector versus Exhausted CD8 T Cell-Fate Decision. *Immunity* **51**, 840-855.e845 (2019).

81. Li, H. *et al.* Dysfunctional CD8 T Cells Form a Proliferative, Dynamically Regulated Compartment within Human Melanoma. *Cell* **181**, 747 (2020).

82. Wu, J. E. *et al.* In vitro modeling of CD8+ T cell exhaustion enables CRISPR screening to reveal a role for BHLHE40. *Sci Immunol* **8, eade3369**, (2023).

83. Schietinger, A. *et al.* Tumor-Specific T Cell Dysfunction Is a Dynamic Antigen-Driven Differentiation Program Initiated Early during Tumorigenesis. *Immunity* **45**, 389–401 (2016).

84. Scharping, N. E. *et al.* Mitochondrial stress induced by continuous stimulation under hypoxia rapidly drives T cell exhaustion. *Nat Immunol* **22**, 205–215 (2021).

85. Voskoboinik, I., Whisstock, J. C. & Trapani, J. A. Perforin and granzymes: function, dysfunction and human pathology. *Nat Rev Immunol* **15**, 388–400 (2015).

86. Paley, M. A. *et al.* Progenitor and terminal subsets of CD8+ T cells cooperate to contain chronic viral infection. *Science (1979).* **338**, 1220–1225 (2012).

87. Sade-Feldman, M. *et al.* Defining T Cell States Associated with Response to Checkpoint Immunotherapy in Melanoma. *Cell* **175, .e1020**, 998–1013 (2018).

88. Kovacs, S. B., Oh, C., Aachoui, Y. & Miao, E. A. Evaluating cytokine production by flow cytometry using brefeldin A in mice. *STAR Protoc* **2**, 100244 (2021).

89. Nahmad, A. D. *et al.* Frequent aneuploidy in primary human T cells after CRISPR-Cas9 cleavage. *Nat Biotechnol* **40**, 1807–1813 (2022).

90. Glaser, V. *et al.* Combining different CRISPR nucleases for simultaneous knock-in and base editing prevents translocations in multiplex-edited CAR T cells. *Genome Biol* **24**, 89 (2023).

91. Tsuchida, C. A. *et al.* Mitigation of chromosome loss in clinical CRISPR-Cas9-engineered T cells. *Cell* **186, .e4520**, 4567–4582 (2023).

92. Chiesa, R. *et al.* Base-Edited CAR7 T Cells for Relapsed T-Cell Acute Lymphoblastic Leukemia. *N Engl J Med* **389**, 899–910 (2023).

93. Chen, Y. *et al.* Association of Clinical Phenotypes in Haploinsufficiency A20 (HA20) With Disrupted Domains of A20. *Front Immunol* **11**, 574992 (2020).

94. Kato, M. *et al.* Frequent inactivation of A20 in B-cell lymphomas. *Nature* **459**, 712–716 (2009).

95. Braun, F. C. *et al.* Tumor suppressor TNFAIP3 (A20) is frequently deleted in Sézary syndrome. *Leukemia* **25**, 1494–1501 (2011).

96. Giles, J. R. *et al.* Shared and distinct biological circuits in effector, memory and exhausted CD8+ T cells revealed by temporal single-cell transcriptomics and epigenetics. *Nat Immunol* **23**, 1600–1613 (2022).

97. Daniel, B. *et al.* Divergent clonal differentiation trajectories of T cell exhaustion. *Nat Immunol* **23**, 1614–1627 (2022).

98. Dou, Z. *et al.* 4-1BB-encoding CAR causes cell death via sequestration of the ubiquitin-modifying enzyme A20. *Cell Mol Immunol* **21**, 905–917 (2024).

99. Pores-Fernando, A. T. & Zweifach, A. Calcium influx and signaling in cytotoxic T-lymphocyte lytic granule exocytosis. *Immunol Rev* **231**, 160–173 (2009).

100. Dong, M. B. *et al.* Systematic Immunotherapy Target Discovery Using Genome-Scale In Vivo CRISPR Screens in CD8 T Cells. *Cell* **178, .e1123**, 1189–1204 (2019).

Publishing Agreement

It is the policy of the University to encourage open access and broad distribution of all theses, dissertations, and manuscripts. The Graduate Division will facilitate the distribution of UCSF theses, dissertations, and manuscripts to the UCSF Library for open access and distribution. UCSF will make such theses, dissertations, and manuscripts accessible to the public and will take reasonable steps to preserve these works in perpetuity.

I hereby grant the non-exclusive, perpetual right to The Regents of the University of California to reproduce, publicly display, distribute, preserve, and publish copies of my thesis, dissertation, or manuscript in any form or media, now existing or later derived, including access online for teaching, research, and public service purposes.

DocuSigned by:
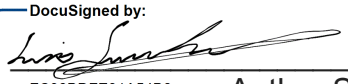
FC98BDFE91A54B8...

Author Signature

05/05/2026

Date